ALMA MATER STUDIORUM · UNIVERSITÀ DI BOLOGNA

Scuola di Scienze

Corso di Laurea Magistrale in Fisica

Characterization of X-ray Detectors based on Organic Semiconducting Single Crystals

Relatore:
Prof.ssa Beatrice Fraboni

Correlatore:
Dott.ssa Laura Basiricò

Presentata da:
Enrico Zanazzi

Sessione I
Anno Accademico 2014/2015

Abstract

Negli anni recenti, lo sviluppo dell'*elettronica organica* ha condotto all'impiego di materiali organici alla base di numerosi dispositivi elettronici, quali i diodi ad emissione di luce, i transistor ad effetto di campo, le celle solari e i rivelatori di radiazione. Riguardo quest'ultimi, gli studi riportati in letteratura si riferiscono per la maggiore a dispositivi basati su materiali organici a film sottile, che tuttavia presentano problemi relativi ad instabilità e degradazione. Come verrà illustrato, l'impiego di singoli cristalli organici come materiali alla base di questi dispositivi permette il superamento delle principali limitazioni che caratterizzano i rivelatori basati su film sottili. In questa attività sperimentale, dispositivi basati su cristalli organici semiconduttori verranno caratterizzati in base alle principali figure di merito dei rivelatori. Tra i campioni testati, alcuni dispositivi basati su singoli cristalli di 6,13-bis (triisopropylsilylethynyl)-pentacene (TIPS-Pentacene) e 5,6,11,12-tetraphenyltetracene (Rubrene) hanno mostrato interessanti proprietà e sono stati quindi maggiormente studiati.

Abstract

In recent years, the development of the *organic electronics* has led to the employment of organic materials as basic materials for the operation of many electronic devices, such as organic light emitting diodes, organic field effect transistors, organic solar cells and radiation sensors. As regards radiation sensors, the studies reported in literature mainly refer to devices based on thin film organic semiconductors, which however present problems due to instability and degradation. As it will be illustrated, organic single crystals overcame most of the major limitations inherent to thin film-based detectors. In this experimental work, OSSCs-based detectors will be characterized in terms of the principal detectors' figures of merit. Among the samples tested, devices based on 6,13-bis(triisopropylsilylethynyl)-pentacene (TIPS-Pentacene) and 5,6,11,12-tetraphenyltetracene (Rubrene) have shown interesting properties and therefore they have been more deeply investigated.

Contents

Introduction

With the invention of the transistor around the middle of the last century, inorganic semiconductors such as Si or Ge began to take over the role as the dominant material in electronics from the previously dominant metals. At the same time, the replacement of vacuum tube based electronics by solid state devices initiated a development which by the end of the 20th century has led to the omnipresence of semiconductor microelectronics in our everyday life. Now at the beginning of the 21st century we are facing a new electronics revolution that has become possible due to the development and understanding of a new class of materials, commonly known as *organic semiconductors*. Unlike the inorganic counterpart, the use of organic semiconductors opens the possibility for large-area fabrication using low-cost, wet processing techniques, such as spin-casting, spray casting and inkjet printing. Moreover, mechanical flexibility of these materials allows the fabrication of flexible devices, opening the field known as *flexible electronics*.

In recent years, numerous electronic devices, including field effect transistors, light-emitting diodes, photovoltaic cells and radiation sensors, have employed organic materials as the active component. As regards radiation detectors, organic materials could be viable candidates for the detection of higher energy photons (X- and gamma-rays), and they were first suggested for radiation detection in the early 1980s. However, the interest in these materials was mostly focused on their scintillating properties, possibly because the material requirements are particularly stringent in the case of direct detectors, as evidenced by the few reports present in the literature on radiation detection based on organic thin films, where stability, reproducibility and the attainment of good sensitivity are still open issues. In fact, it must be pointed out that the direct conversion of ionizing radiation into an electrical signal within the same device is a more effective process than indirect conversion, since it potentially improves the signal-to-noise ratio and it reduces the device response time. Thanks to their particular properties, Organic Semiconducting Single Crystals (OSSCs) are ideal candidates to directly detect X-ray radiation, since they overcome most of the major limitations inherent to thin film-based detectors, as will be discussed in detail. Moreover, being based on carbon, their low effective atomic number is similar to the average human tissue-equivalent Z value and makes them ideal candidates for radiotherapy and medical applications, which would benefit greatly from the improved accuracy of tissue-equivalent dosimeters. In fact, there are currently no low-cost, large-area detectors with tissue-equivalence response available.

Within the *i-flexis*[1] European project, this experimental work has been dedicated to the study and characterization of direct X-ray detectors based on OSSCs. Sixteen samples belonging to different organic molecules have been tested and characterized as direct X-ray detectors in terms of the most important detectors' figures of merit (sensitivity, dark current, signal-to-noise ratio). Samples based on single crystals of the following organic molecules will be the object of this study:

- 6,13-bis(triisopropylsilylethynyl)pentacene (TIPS-Pentacene);
- 5,6,11,12-tetraphenyltetracene (Rubrene);
- 1,2-dimethyl-1,1,2,2-tetraphenyldisilane (DMTPDS);
- 5,6,11,12-tetraphenyltetracene (Naphthalene);
- Methylphenylnaphtaleneimide (NTHI)

Among the previous molecules, detectors based on both TIPS-Pentacene and Rubrene have shown interesting properties and a significant response under X-rays, although lower than that of other OSSCs-based X-ray detectors reported in literature. Therefore, these samples have been more deeply investigated.

The first chapter of this thesis will illustrate the general properties of organic materials, discussing the charge transport mechanism of organic semiconductors and the principles related to the metal/semiconductor interfaces. In closing, after introducing the organic single crystals, the principal methods for their growing will be described.

In the second chapter, after an introduction on the radiation interaction with matter, an overview on radiation detectors will be illustrated. Among the radiation detectors, a focus on solid state detectors and on their most important figures of merit will be reported. Moreover, an overview on organic semiconductor X-ray detectors based on thin films and single crystals will be illustrated in the last two subsections.

The third chapter will describe the general procedure adopted throughout the experimental work, including the description of the sample preparation method and the measurement setup. Subsequently, the measurement procedure and the data analysis method will be illustrated. In closing, the last subsection will report the characterization results of the reference devices.

The fourth and fifth chapter will report the characterization results of the TIPS- and Rubrene-based detectors, respectively.

Although the other OSSCs-based samples (DMTPDS-, Naphthalene- and NTHI-based devices) have not shown a significant response under X-rays, the characterization results of the related samples will be shown in the sixth chapter.

The seventh chapter will be a discussion of the results obtained through the entire activity and in the eighth and last chapter we will report the conclusions.

[1] www.iflexis.eu

1 Organic electronics

In this chapter, an introduction on the fundamental properties of organic materials will be treated in subsection 1.1. Among the organic materials, organic semiconductors are the basis of the organic electronics and their most important properties will be discussed in subsection 1.2. Subsequently, in subsection 1.3, the charge transport mechanism of these materials will be illustrated. Since metal/semiconductors interfaces are very important in electronic devices, a summary on this topic will be reported in subsection 1.4. After introducing the organic single crystals, in subsection 1.5 the principal methods for their growing will be described.

1.1 Introduction to organic materials

The adjective *organic* used in the expression *organic electronics* refers to the fact that, in this branch of electronics, the active materials used for the fabrication of devices are organic compounds. Although the distinction between "organic" and "inorganic" compounds is not always straightforward, an organic molecule is usually defined as a chemical compound containing carbon. Consequently, in order to explain and understand the electrical properties of organic compounds it is necessary to describe the electronic configuration of the carbon atom and the way it forms chemical bonds with other atoms (of the same type or belonging to different chemical species).

Carbon is an element belonging to the group 14 of the periodic table. The members of this group are characterized by the fact that they have four electrons in the outer energy level. Since there are three naturally occurring isotopes of carbon (carbon-12, carbon-13 and carbon-14), but the carbon-12 is the most stable and the most abundant, we will refer to the carbon-12 whenever the name "carbon" will be used throughout this thesis. [**1**] [**2**]

In order to understand the electronic properties of organic compounds it is essential to describe the way carbon electrons are distributed in space and the way they are bonded to the nuclei. In other words, it is necessary to introduce the concepts of *atomic orbital* and *orbital hybridization.*

According to quantum mechanics, the wave-like behavior of an electron may be described by a complex wavefunction depending on both position and time $\Psi(r,t)$; the square modulus $|\Psi(r,t)|^2$ is equal to a probability density: the integral of the square modulus over a certain volume V gives the probability of finding, at a certain instant t, the electron in that volume. We can therefore define as *atomic orbital* the region of space in which the probability of finding an electron is at least 90%. Each orbital is defined by a different set of quantum numbers and, due to the Pauli's

exclusion principle, it contains a maximum of two electrons. The shape of each orbital depends on the mathematical definition of the wavefunction and therefore on the value assumed by the l quantum number. As shown in Figure 1.1, for $l = 0$ we obtain the orbitals 1s and 2s, which are shaped as spheres centered in correspondence with the atom nucleus. The three orbitals on the bottom are the 2p orbitals and are obtained for $l = 1$. In this case each orbital is shaped as a couple of ellipsoids with a point of tangency in correspondence with the atom nucleus. The three p orbitals are reciprocally orthogonal: if we consider a cartesian coordinate system centered in the nucleus, these orbitals appear aligned along the three axes and are therefore called $2p_x$, $2p_y$ and $2p_z$ orbitals. Since the carbon atom has $Z = 6$, the ground-state electron configuration of carbon may be expressed, according to the IUPAC standard rules, by the following notation: $1s^2 2s^2 2p^2$. [**2**]

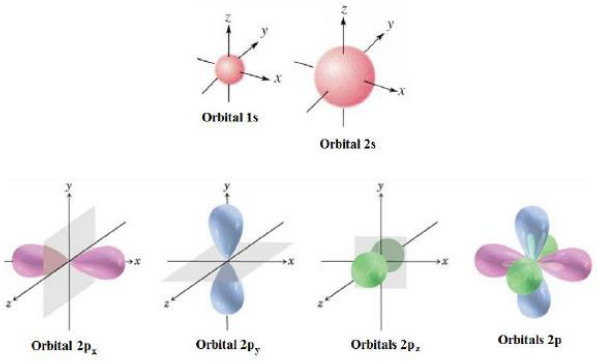

Figure 1.1: Shape of the orbitals 1s, 2s and 2p. [2**]**

In order to understand the charge transport mechanisms within the organic materials, it is necessary to describe the concept of *hybrid orbital*, introduced by Linus Pauling in 1931. Let us take *n* different orbitals, each one described by its own wavefunction $\Psi(r,t)$. When hybridization occurs, these orbitals are linearly combined in order to form *n* new hybridized orbitals, each one corresponding to its own wavefunction $\Phi_j(r,t)$. From a qualitative point of view, hybridization may be thought of as a "mix" of atomic orbitals which results in the formation of new, isoenergetic orbitals more suitable for the description of specific molecule structure, as that of the methane, shown in Figure 1.2. As can be seen, methane is characterized by a tetrahedral geometry, in which the carbon atom occupies the tetrahedron center while the four hydrogen atoms are placed in correspondence with the four tetrahedron corners. [**1**] [**3**]

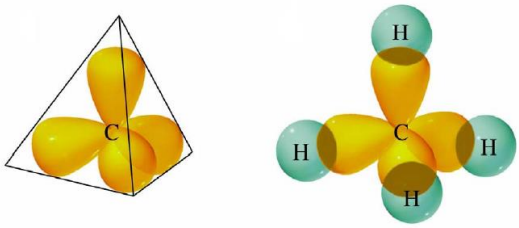

Figure 1.2: Methane molecule CH_4. [3**]**

The carbon atom can give rise to three different hybridization (sp^3, sp^2 and sp), depending on the bonds that it arranges with other atoms. [**4**]

In the case of methane, the structure may be explained by considering the hybridization of carbon outer orbitals (the 2s and the three 2p orbitals) which results in the formation of four sp^3 orbitals (Figure 1.3). The four sp^3 orbitals of carbon partially overlap with the 1s orbitals of hydrogen atoms, giving rise to four covalent bonds which are usually indicated as σ-bonds.

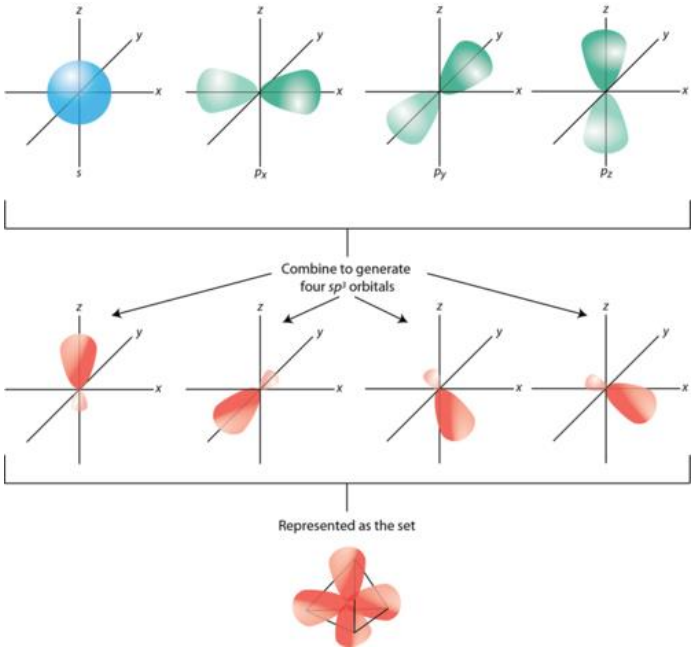

Figure 1.3: Sp^3 hybridization. [2]

The hybridization sp^2 takes place, for instance, in the ethylene molecule $CH_2=CH_2$ (Figure 1.4). In this case, the 2s orbital and two 2p orbitals (let us assume $2p_x$ and $2p_y$) hybridize and form a set of three sp^2 orbitals which lie on the XY plane and are located in correspondence with the corners of an equilateral triangle (Figure 1.5). The fourth, unhybridized $2p_z$ orbital lies along a direction which is perpendicular to the plane containing the hybridized sp^2 orbitals. [**1**]

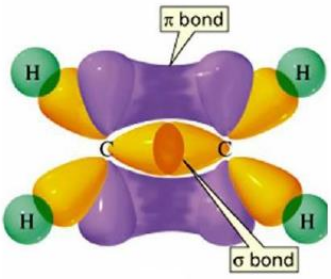

Figure 1.4: Ethylene molecule $CH_2=CH_2$. [2]

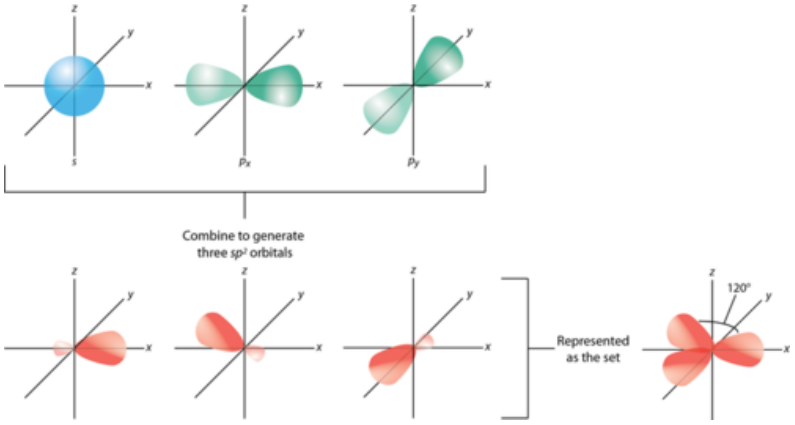

Figure 1.5: Sp^2 hybridization. [2]

When two sp^2-hybridised carbon atoms come into close contact in order to form a chemical bond, the orbitals overlap occurs at two different levels. On one hand, one can notice the formation of a covalent σ -bond resulting from the intersection between two sp^2 orbitals along the line joining the two carbon atoms' nuclei. The other two sp^2 orbitals overlap with the hydrogen atoms' 1s orbitals and form two other covalent σ -bonds. When the two carbon atoms come into contact, a partial overlap between the two unhybridized $2p_z$ orbitals occurs. This overlap is responsible for the formation of a second covalent bond between the carbon atoms, called π-bond. These two types of covalent bond are shown in Figure 1.6. [**1**] [**2**]

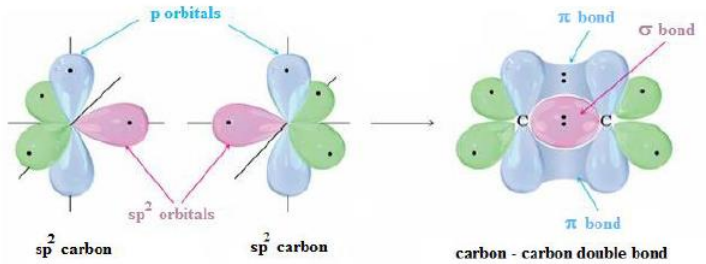

Figure 1.6: formation of π and σ bonds. [2]

Since the σ bond is characterized by a much larger overlap volume, the σ bonds are more energetic than the π bonds. This phenomenon has very important consequences for the electrical behavior of the molecule: while σ electrons are strictly confined into the small volume between the two carbon atoms' nuclei, π electrons are able to move into a larger volume and their interaction with the nuclei is relatively weak. [**1**] [**2**]

1.2 Organic semiconductors

In order to understand how organic devices work it is essential to have a clear picture of the conduction mechanisms in organic conductors and semiconductors.

Let us define a *polymer* as a molecule composed of repeating structural units called monomers, which are characterized by a low relative molecular mass and are interconnected typically by means

of covalent bonds. More specifically, conductive polymers are usually defined as organic polymers able to conduct electricity, exhibiting a conductive or a semiconductive behavior. Conductive polymers can be roughly grouped into three different categories:

- conjugated polymers;
- polymers containing aromatic cycles;
- conjugated polymers containing aromatic cycles.

All the molecules belonging to the previous categories have in common the alternation of single and multiple bonds (usually, double bond) in their structure. This is shown for example in Figure 1.7a for the simplest conjugated molecule, polyacetylene. [**2**]

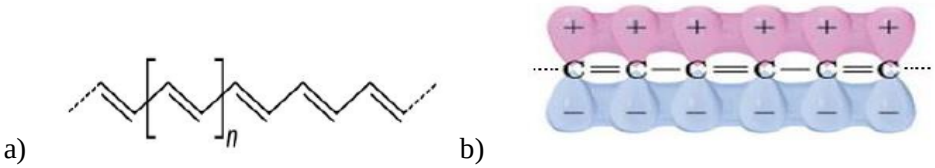

Figure 1.7: a) polyacetylene and b) overlap of p-orbitals in conjugated polymers. [2**]**

In these molecules, the p-orbitals of the π-electrons overlap (Figure 1.7b), thus, the arrangement of the electrons is reconfigured concerning the energy levels. We can separate the molecular energy levels into two categories: π and π*, bonding and anti-bonding respectively, forming a band-like structure (Figure 1.8). The occupied π-levels are the equivalent of the valence band in inorganic semiconductors. [**3**]

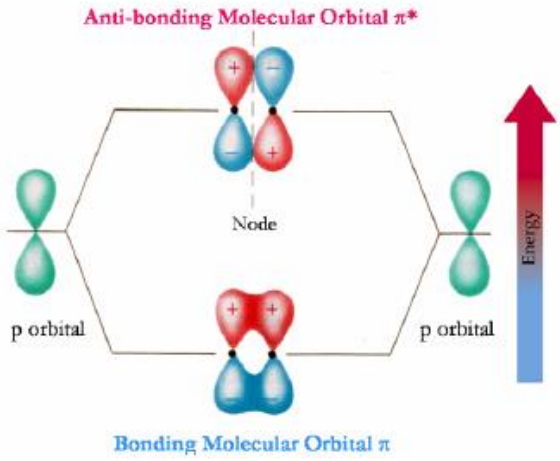

Figure 1.8: bonding and anti-bonding π molecular orbitals. [3**]**

The electrically active level is the highest one and it is called Highest Occupied Molecular Orbital (HOMO). The unoccupied π*-levels are equivalent to the conduction band. In this case, the electrically active level is the lowest one, called Lowest Unoccupied Molecular Orbital (LUMO). The resulting band gap is given by the difference of the energy between HOMO and LUMO. If we

consider a polymer chain with N atoms using the quantum mechanical model for a free electron in a one dimensional box, the wave functions for the electrons of the polymer chain is given by:

$$E_n = \frac{n^2 h^2}{8mL^2} \qquad \textbf{Equation 1.1}$$

with n positive integer and where h is the Plank constant, m the electron mass and L the conjugation length, which, if we consider N atoms separated by a distance d within the polymer chain, is equal to Nd. Therefore, if the π-electrons from the p-orbitals of the N atoms occupy these molecular orbits, with 2 electrons per orbit, then the HOMO should have an energy given by:

$$E\ (HOMO) = \frac{\left(\frac{N}{2}\right)^2 h^2}{8mL^2} \qquad \textbf{Equation 1.2}$$

whereas, the LUMO will have an energy of:

$$E\ (LUMO) = \frac{\left(\frac{N}{2}+1\right)^2 h^2}{8m(Nd)^2} \qquad \textbf{Equation 1.3}$$

All energies are supposed to be measured with respect to vacuum energy level as reference. Thus, the energy required to excite an electron from the HOMO to the LUMO is given by their energies difference:

$$E_g = E(LUMO) - E(HOMO) = \frac{(N+1)^2 h^2}{8m(Nd)^2} \cong \frac{h^2}{8md^2N} \quad for\ large\ N \qquad \textbf{Equation 1.4}$$

It is evident that the band gap is inversely proportional to the conjugation length L, and, as a consequence, to the number of atoms N in the polymer chain. If the band gap is high the material is an insulator, if it is low the material is a conductor. Usually the most of the organic semiconductors have a band gap between 1.5 to 3 eV. [**3**]

In organic electronics, semiconductors based both on single crystals and polycrystalline materials can be employed. Single crystals of conjugated organic molecules are the materials with the highest degree of order and purity among the variety of different forms of semiconductors. Electronic devices comprising these materials are by far the best performers in terms of the fundamental parameters such as charge-carrier mobility, exciton diffusivity, concentration of defects and operational stability. [**5**]

Figure 1.9 shows, for example, the optical microscopy image of two different types of organic single crystals reported in literature: 4-hydroxycyanobenzene (4HCB) and 1,5-dinitronaphthalene (DNN). [**6**]

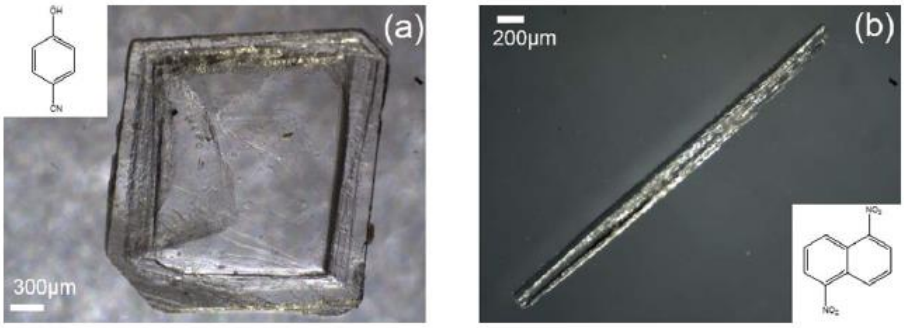

Figure 1.9: Optical microscopy images of (a) 4-hydroxycyanobenzene (4HCB) and (b) 1,5-dinitronaphthalene (DNN) organic single crystals. [6**]**

1.3 Charge carrier transport in organic semiconductors

In subsection 1.2 we have shown that if we hypothesize an ordered, periodic structure, then the electronic properties of a single polymer chain may be illustrated through a band diagram showing a band gap in which a conduction and valence bands may be clearly identified.
However, when polymer molecules aggregate, the resulting polymeric solids exhibit different crystallinity degree, varying from almost perfect crystals to amorphous solids. As a consequence, charge carrier transport in such solids varies in a range delimited by two extreme cases: band transport and hopping. [**1**] [**7**]

Band transport is normally observed only in pure, single organic crystals. In such materials, charge mobility depends on temperature according to the following power law:

$$\mu \propto T^{-n} \ \ with \ \ n = 1 \dots 3 \qquad \textbf{Equation 1.5}$$

In highly disordered polymeric solids, such as amorphous solids, transport usually proceeds via hopping and is thermally activated. In amorphous solids, molecules are arranged in a random, disordered way. Therefore, energy states are not organized in continuous bands separated by an energy gap but instead localized energy states (i.e. existing only for discrete values of the wave number k) occur. The density of these states is usually described using a couple of Gaussian distributions, being centered in correspondence with the energy level where the majority of levels appear. The functions peaks may be interpreted as analogous to conduction and valence bands in crystalline semiconductors (Figure 1.10). [**1**] [**2**]

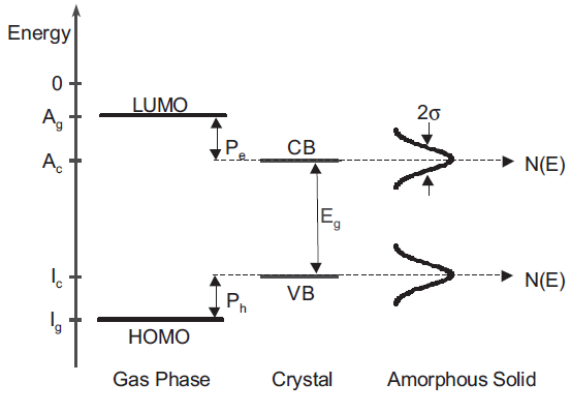

Figure 1.10: energy diagram in different type of organic semiconductors. [1]

In amorphous solids, charge flow takes place when electrons start moving (hopping) from lower energy levels to higher energy levels. This flow is due to an increment in electrons energy which may be caused both by temperature or the application of an external electric field. A simple model frequently used in order to express mathematically the mobility dependence on the factors cited above is the following:

$$\mu(F,T) \propto \exp\left(-\frac{\Delta I}{kT}\right) exp\left(\frac{\beta\sqrt{F}}{kT}\right) \qquad \textbf{Equation 1.6}$$

where E is a parameter called activation energy (i.e. the minimum amount of energy to be provided in order to start conduction) and F represents the applied electric field.

The case of semicrystalline polymeric solids is perhaps the most complicated, from an analytical point of view. These solids usually assume a polycrystalline structure, in other words they may be thought of as many crystalline grains immersed into an amorphous matrix. While within the grains charges move thanks to band transport, the problem arises in correspondence with the grain boundaries. Here, mobile charges are temporarily immobilized (trapping) thus creating a potential barrier which electrostatically repels same sign charges; as a consequence, charge mobility is greatly decreased. A simple expression utilized in order to express mobility in polycrystalline semiconductors is given by the following:

$$\mu \propto \mu_0 exp\left(-\frac{E_b}{kT}\right) \qquad \textbf{Equation 1.7}$$

In Equation 1.7, μ_0 is the mobility in crystalline grains and E_b is the height of potential barrier. [**1**]

1.4 Charge carrier injection into organic semiconductors

In electronic devices based on organic semiconductors, metal/organic semiconductor interfaces are very important and can strongly influence both the type and the amount of charge carrier injected into the channel. In principle, all organic semiconductors should be able to allow both

kinds of charge carriers transport. Therefore, achieving n-type or p-type conduction should only depend on the metal employed for the electrodes that should be able to efficiently inject one type of charge carriers into the semiconductor layer. Indeed, charge injection strongly depends on the energy level matching between the Fermi level of the metal electrodes and organic semiconductors energy levels, namely, lowest unoccupied molecular orbital (LUMO) and highest occupied molecular orbital (HOMO). One of the fundamental aspects of the metal/semiconductor interface is the Fermi level alignment, described by the Mott-Schottky model. When a neutral metal and a neutral semiconductor are brought in contact, the Mott-Schottky model predicts that their bulk Fermi levels will align, causing band bending in the semiconductor (Figure 1.11). [**3**]

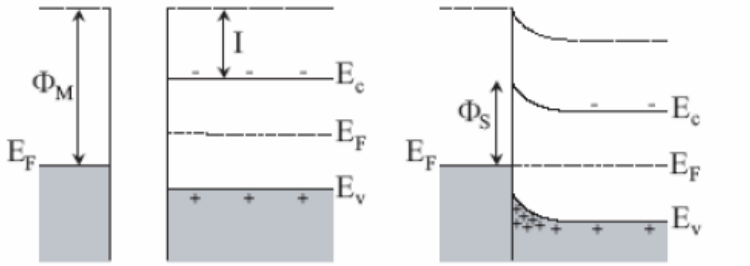

Figure 1.11: Energy-band diagrams under thermal equilibrium for a) a metal (left) and an intrinsic semiconductor (right) that are not in contact; b) a metal/semiconductor contact, with band bending region in the semiconductor, close to the interface with the metal. E_c and E_v indicate the edge of the conduction band and the edge of the valence band; E_F indicates the position of the Fermi level. [3**]**

Due to the band bending, a non-Ohmic Schottky barrier can be formed at the interfaces between metal and semiconductor. As a consequence, charge transport can be limited by injection through the Schottky barrier and is characterized by thermal excitation of charge carriers over the barrier, resulting in thermally excited temperature dependence. Mott-Schottky model is generally used as a guideline for choosing the contact metal. The height of the injection barrier will be given by the difference between the metal Fermi level and the HOMO or LUMO levels of the organic semiconductor for holes and electrons respectively.

There are several aspects that can modify the Mott-Schottky-type of band bending. One of these is the formation of surface dipoles at the interface between the metal and the organic semiconductor. Another aspect that can have a strong influence in charge injection is the presence of traps at the metal/organic interface that are mostly produced during contact fabrication. [**3**]

1.5 Single crystal growth of organic semiconductors

As already mentioned, organic semiconductors can be employed for the fabrication of electronic devices either as polycrystalline thin film or single crystals. Organic semiconducting thin films are used in numerous applications such as organic field-effect transistors (OFETs), organic light-emitting diodes (OLEDs), and organic solar cells because of their light weight, flexibility, solubility, low-temperature processability, large-scale yields, and low cost. Spin coating, drop

casting, or printing techniques can be applied in the production of prototype electronic devices. However, grain boundaries, defects, dislocations, and impurities make polycrystalline organic films not suitable for the investigation of the intrinsic properties of organic semiconductors. Instead, organic single crystals that can be prepared with high purity, low density of defects and high performances are ideal model compounds. Moreover, they provide an ideal platform for the studies of the intrinsic physical properties of organic semiconductors. [**8**]

As reported in literature, the study of organic single crystal has led to their employment in electronic devices as for example OFETs and X-ray detectors. [**9**] [**10**] [**11**]

A large number of organic crystal growth methods have been developed (solution, gas-phase and melt-growth method) and most have been based on modified inorganic crystal growth method.
The best-performing OSSCs are usually grown by Chemical Vapor Deposition (CVD), which involves the use of multi-zone heated tubes, in which a vapor of molecules is carried by a convenient inert gas onto a cold wall. However, due to the nature of this growth process, it is difficult to grow very large crystals. Crystal growth from the melt could represent an interesting alternative to CVD; nonetheless, although in some cases crystallization from the melt of OSSCs proved to be successful, stability problems (especially due to enhanced photo-oxidation rates at temperatures approaching the melting temperature) often limit the possibility of taking advantage of this crystallization technique for organic materials. These problems may be overcome using growth from solution. This approach has a high versatility, with the capability to deliver very large (up to several cm^3) and pure crystals, and with low energy requirements (i.e. no need for dramatic heating, cooling or vacuum) and ease of implementation. This latter point is worthy of particular attention, since it implies an extremely low cost, especially when large-area detectors are envisaged. [**6**] [**9**]

In this subsection we report three single crystal growth methods: the solvent evaporation method, the physical vapor transport (PVT) method and the Bridgman growth method. We remand to [**8**] and [**6**] for further information.

The solvent evaporation method is the simplest and most effective method to grow single crystals, and most organic crystals used for crystal structure analysis are grown by this method. Using an organic solvent, if a beaker containing a saturated solution is not covered too tightly, the solvent can slowly evaporate forming supersaturated solution. Then nuclei (seeds) spontaneously form, growing into larger crystals (Figure 1.12). [**8**]

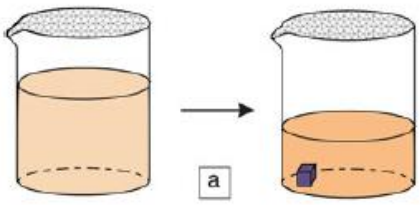

Figure 1.12: solvent evaporation method. [8**]**

The physical vapor transport (PVT) is a method that combines crystal growth with material purification. There are different PVT methods frequently employed: open systems, closed systems, and semi-closed system. In an open system, an inert gas controls the speed of sublimation, deposition, and crystal growth of organic molecules. Considering Figure 1.13, the material is heated

in zone 1 and sublimed in a flow of carrier gas under pressures ranging from a few Torr to atmospheric pressure. The molecular vapor crystallizes downstream at a lower temperature in zone 2, with pure crystals separated from impurities due to the temperature gradient and the flow of the carrier gas. [**8**]

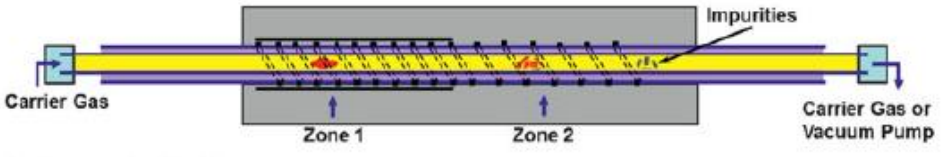

Figure 1.13: PVT in an open system. [8**]**

.

The Bridgman growth method is used for the growth of large single crystals inside sealed ampoules. In this method, a quartz ampoule is filled with powdered material. The ampoule is sealed under vacuum or with an inert gas, and then moves through a temperature gradient. At a certain temperature, crystal nucleation is induced at the tip of the ampoule, and the crystallization front propagates through the melted material. The ampoule moves slowly across the temperature gradient, and as the solubility of many impurities in the melt is different from the crystal solubility, the deposited impurities are separated from the crystals. However, if the solubility of the impurities in the melt is almost the same as that in the crystals, impurities cannot be removed by this method. Therefore, purification needs to be carried out in a separate process before crystal growth. [**8**]

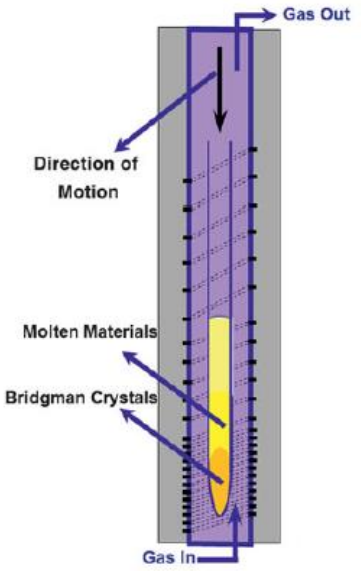

Figure 1.14: Bridgman growing method. [8**]**

2 Radiation detection

In order to understand the general properties of radiation detectors, an introduction on the radiation interaction with matter will be reported in subsection 2.1. Subsequently, in subsection 2.2 an overview on radiation detectors including the different operation modes will be illustrated. Solid state detectors based on inorganic semiconductor materials will be treated in subsection 2.3. Moreover, an overview on organic semiconductor detectors based on thin films and single crystals will be illustrated in subsections 2.4 and 2.5, respectively.

2.1 Radiation interactions with matter

To organize the discussion that follow, it is convenient to arrange the four major categories of radiation into the following matrix:

Charged Particulate Radiations		Uncharged Radiations
Heavy charged particles (characteristic distance $\cong 10^{-5}$ m)	⇐	Neutrons (characteristic length $\cong 10^{-1}$ m)
Fast electrons (characteristic distance $\cong 10^{-3}$ m)	⇐	X-rays and gamma rays (characteristic length $\cong 10^{-1}$ m)

Figure 2.1: the four major categories of radiation. [12**]**

The entries in the left column represent the charged particles that, because of the electric charge carried by the particle, continuously interact by means of the Coulomb force with the electrons present in any medium through which they pass. The radiations in the right column are uncharged and therefore are not subject to the Coulomb force. Instead, these radiations must first undergo an interaction that radically alters the properties of the incident radiation in a single encounter. In all cases of practical interest, the interaction results in the full or partial transfer of energy of the incident radiation to electrons or nuclei of the constituent atoms, or to charged particle products of nuclear reactions. If the interaction does not occur within the detector, these uncharged radiations (e.g., neutrons or gamma rays) can pass completely through the detector volume without revealing the slightest hint that they were ever there. The horizontal arrows shown in the diagram illustrate the results of such interactions. An X- or gamma ray, through the processes described below, can transfer all or part of its energy to electrons within the medium.

Although a large number of possible interaction mechanism are known for gamma rays in matter, only three major types play an important role in radiation measurements*: photoelectric absorption*, *Compton scattering*, and *pair production*. All of these processes lead to the partial or complete transfer of the gamma-ray photon energy to electron energy. [**12**]

Photoelectric absorption: in this process, a photon undergoes an interaction with an absorber atom in which the photon completely disappears. In its place, an energetic photoelectron is ejected by the atom from one of its bound shells. The interaction is with the atom as a whole and cannot take place with free electrons. The photoelectron appears with an energy given by

$$E_{e^-} = h\nu - E_b \qquad \textbf{Equation 2.1}$$

where hν is the energy of the original photon and E_b represents the binding energy of the photoelectron in its original shell. For gamma-ray energies of more than a few hundred keV, the photoelectron carries off the majority of the original photon energy. In addition to the photoelectron, the interaction also creates an ionized absorber atom with vacancy in one of its bound shell. This vacancy is quickly filled through capture of a free electron from the medium and/or rearrangement of electrons from other shells of the atom. Therefore, one or more characteristic X-ray photons may also be generated.

The photoelectric process is the predominant mode of interaction for X-rays of relatively low energy. The process is also enhanced for absorber materials of high atomic number Z. No single analytic expression is valid for the probability of photoelectric absorption per atom over all ranges of E_γ (photon's energy) and Z, but a rough approximation is

$$\tau \cong \text{constant} \times \frac{Z^n}{E_\gamma^{3.5}} \qquad \textbf{Equation 2.2}$$

where the exponent n varies between 4 and 5 over the gamma-ray energy region of interest. [**12**]

Compton scattering: this interaction takes place between the incident gamma-ray and an electron in the absorbing material. The photon transfers a portion of its energy to the electron (assumed to be initially at rest), which is then known as a recoil electron.

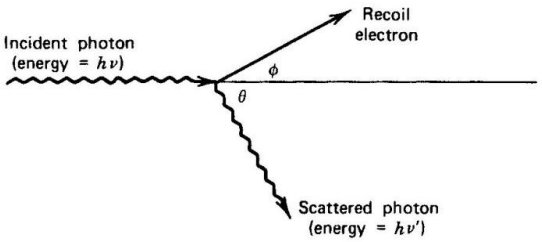

Figure 2.2: Compton scattering. [12**]**

The incoming gamma-ray is than deflected by an angle θ with respect to its original direction. Because all angles of scattering are possible, the energy transferred to the electron can vary from zero to a large fraction of the gamma-ray energy. The expression that relates the energy transfer and the scattering angle for any given interaction can simply be derived by writing simultaneous equations for the conservation of energy and momentum. Using the symbols defined in Figure 2.2 we can show that:

$$h\nu' = \frac{h\nu}{1 + \frac{h\nu}{m_0 c^2}(1 - \cos\theta)} \qquad \textbf{Equation 2.3}$$

where m_0c^2 is the rest-mass energy of the electron (0.511 MeV). The probability of Compton scattering per atom of the absorber depends on the number of electrons available as scattering targets and therefore increases linearly with Z. [**12**]

Pair production: if the gamma ray exceeds twice the rest-mass energy of an electron (1.02 MeV), the process of pair production is energetically possible. As a practical matter, the probability of this interaction remains very low until the gamma-ray energy approaches several MeV and therefore pair production is confined to high-energy gamma rays. In the interaction (which must take place in the coulomb field of a nucleus), the gamma-ray photon disappears and is replaced by an electron-positron pair. All the excess energy carried in by the photon above the 1.02 MeV required to create the pair goes into kinetic energy shared by the positron and the electron. No simple expression exists for the probability of pair production per nucleus, but its magnitude varies approximately as the square of the absorber atomic number. [**12**]

The relative importance of the three processes described above for different absorber materials and gamma-ray energies is conveniently illustrated in Figure 2.3.

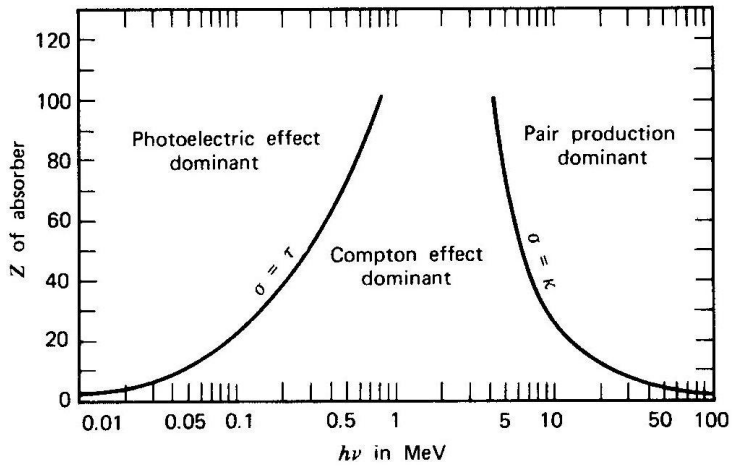

Figure 2.3: The relative importance of the three major types of gamma-ray interaction. The lines show the values of Z and hν for which the two neighboring effects have the same probability. [12**]**

The line at the left represents the absorber atomic number at which photoelectric absorption and Compton scattering are equally probable as a function of the photon's energy. The line at the right represents the absorber atomic number at which Compton scattering and pair production are equally probable. Three areas are thus defined on the Z, energy parameter space where photoelectric absorption, Compton scattering, and pair production each predominate. [**12**]

2.2 Radiation detectors

Before discussing specifically the features of the radiation detectors based on organic materials, we first outline some general properties of a radiation detector. We begin with a hypothetical detector that is subject to a quantum of radiation, which could be an individual X- or gamma-ray photon. In order for the detector to respond at all, radiation must undergo interaction through one of the mechanism discussed in subsection 2.1.

The net result of the radiation interaction in a wide category of detectors is the appearance of a given amount of electric charge within the detector active volume. Our simplified detector model thus assume that a charge Q appears within the detector at time t = 0 resulting from the interaction of a single quantum of radiation. Next, this charge must be collected to form the basic electrical signal. Typically, collection of the charge is accomplished through the imposition of an electric field within the detector, which causes the positive and negative charges created by the radiation to flow in opposite direction. The time required to fully collect the charge varies greatly from one detector to another: this time reflects both the mobility of the charge carriers within the detector active volume and the average distance that must be traveled before arrival at the collection electrodes. We therefore begin with a model of a prototypal detector whose response to a quantum of radiation will be a current that flows for a time equal to the charge collection time. The sketch in illustrate one example for the time dependence the detector current might assume, where t_c represents the charge collection time.

$$\int_0^{t_c} i(t)dt = Q \qquad \textbf{Equation 2.4}$$

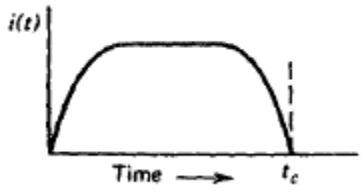

Figure 2.4: current vs time in a radiation detector. [12**]**

As described by Equation 2.4, the time integral over the duration of the current must simply be equal to Q, the total amount of charge generated in that specific interaction.

We can now introduce a fundamental distinction between three general modes of operation of radiation detectors. The three modes are called *pulse mode*, *current mode* and *mean square voltage mode*. [**12**]

In pulse mode operation, the measurement instrumentation is designed to record each individual quantum of radiation that interacts in the detector. In most common applications, the time integral of each burst of current, or the total charge Q, is recorded since the energy deposited in the detector is directly related to Q. At very high event rates, pulse mode operation becomes impractical or even impossible.
In current mode operation, we assume that the measuring device has a fixed response time T, then the recorded signal from a sequence of events will be a time-dependent current given by

$$I(t) = \frac{1}{T}\int_{t-T}^{t} i(t')dt' \qquad \textbf{Equation 2.5}$$

Because the response time T is typically long compared with the average time between individual current pulses from the detector, the effect is to average out many of the fluctuations in the intervals between individual radiation interactions and to record an average current that depends on the product of the interaction rate and the charge per interaction.
The mean square voltage mode of operation is most useful when making measurements in mixed radiation environments when the charge produced by one type of radiation is much different than that from the second type. [**12**]

2.3 Solid state detectors

With respect to gas radiation detectors, the use of solid state detectors is of great advantage in many radiation detection applications. For example, detectors dimension can be kept much smaller than the equivalent gas-filled detectors because solid densities are some 1000 times greater than that for a gas. [**12**]
Considering solid state detectors, high energy photons (X- and gamma-rays) can be detected with two different categories of functional materials: scintillators and semiconductors. In both cases, the interaction with a high energy photon first induces primary excitations and ionization processes (ions and electrons) which, at a second stage, interact within the volume of the detection material and produce a majority of secondary excitations (electron–hole pairs), within a picosecond timeframe. The by-products of both the primary and secondary excitations are electron–hole pairs (excitons) that can be transduced into an output signal following different pathways in semiconductor detectors and in scintillators, described in more detail in the following.
In a scintillator, the excitons transfer their energy to luminescent centers which are often intentionally introduced. These centers release the energy radiatively, and the resulting photons, typically in the visible wavelength range, escape the scintillator and are collected by a coupled photo-multiplier tube (PMT) or a photodiode to obtain an electrical signal associated to the incident radiation beam. [**6**]
In a semiconductor detector (e.g. CdTe, SiC), an electric field is applied to dissociate the electron–hole pairs and to sweep the electrons and holes to the positive and negative electrodes, respectively. The resulting photocurrent is directly recorded as the output electrical signal associated to the high energy radiation particles. The direct conversion of ionizing radiation into an electrical signal within the same material, and thus within one single device, is a more effective process than indirect

conversion, since it potentially improves the signal-to-noise ratio and it reduces the device response time. The material requirements for the two different detection mechanisms share some similarities: high stopping power to maximize the absorption efficiency of the incident radiation, high purity to minimize exciton trapping, and good uniformity to reduce scattering and good transparency, possibly coupled to the ability to grow the material into a large size to increase the interaction volume. For semiconductors, a high and balanced carrier mobility and a low intrinsic carrier density are essential to obtain a high sensitivity and a low background current. On the other hand, scintillators must have an efficient cascade energy transition series to achieve a high light emission yield. [**6**]

High purity silicon and germanium were the first materials to be used as solid state detectors, and are still widely employed thanks to their extremely good energy resolution which, however, can only be achieved at cryogenic temperatures. This prompted the development of novel compound semiconductors such as CdTe, SiC and CdZnTe which can offer excellent performance at room temperature, superior in a few aspects to Ge.

Nonetheless, the difficulty to grow large-size, high-quality crystals of these II–VI compound materials at a low cost is limiting their application in very high-tech and specific detectors, e.g. in satellites and as pioneering medical diagnostic tools. A non-negligible further drawback of these materials is their limited availability, and often their toxicity. These limitations have prompted the need to find alternative novel semiconducting materials.

The main requirements for a good solid state semiconductor detector are common to all semiconductors and are briefly detailed below:

- High sensitivity, which is defined as the detector's capability of producing a usable signal for a given type of radiation and energy. [**13**]
- High resistivity ($>10^9$ Ω cm) and low leakage current. Low leakage currents when an electric field is applied during operation are critical for low noise operation. The necessary high resistivity is achieved by using larger band gap materials (> 1.5 eV) with low intrinsic carrier concentrations.
- A small enough band gap so that the electron–hole ionization energy is small (< 5 eV). This ensures that the number of electron–hole pairs created is reasonably large and results in a higher signal to noise ratio.
- High atomic number (Z) and/or a large interaction volume for efficient radiation–atomic interactions. The cross-section for photoelectric absorption in a material of atomic number Z varies as Z^n, where $4 < n < 5$. For high-sensitivity and efficiency, large detector volumes are required to ensure that as many incident photons as possible have the opportunity to interact in the detector volume. A further related requirement is that the detector material must have a high density, although this is essentially guaranteed simply by the fact that a solid material is employed for the detector material in contrast to gas-based detectors.
- High intrinsic μτ product. The carrier drift length is given by μτE, where μ is the carrier mobility, τ is the carrier lifetime and E is the applied electric field. Charge collection is determined by which fraction of photo-generated electrons and holes effectively traverses the detector and reaches the electrodes.

- High-purity, homogeneous, defect-free materials, to ensure good charge transport properties, low leakage currents, and no conductive short circuits between the detector contacts.
- Electrodes which produce no defects, impurities or barriers to the charge collection process and which can be used effectively to apply a uniform electric field across the device. This requirement is also related to the need to avoid material polarization effects which may affect the time response of the detector.
- Surfaces should be highly resistive and stable over time to prevent increases in the surface leakage currents over the lifetime of the detector.

It is obvious that not all of the above requirements can be easily met by a single material, but the dramatic advancements in the organic semiconductor research field recently have stimulated studies on the potential application of organic semiconductors as solid-state detectors. [**6**]

2.4 Solid state detectors based on organic thin film materials

Let us now consider the organic materials and their applications in solid state detectors. The first studies performed featured the neutron irradiation of polyacetylene and polythiophene films, which induced an increase in the film conductivity, linear with the irradiation dose but irreversible. [**6**] To date, only a few examples of simple, direct detectors based on organic semiconductors have been reported, and they all refer to thin films based on organic semiconducting polymers and small molecules. When compared to silicon-based detectors, conjugated polymers, despite their lower carrier mobility and inferior radiation tolerance, exhibit the advantage that large areas can be covered and possibly nanostructured via wet-processing, thus increasing the detector's active surface at a much lower cost. Moreover, radiation detectors made from polymers exhibit greater mechanical flexibility in comparison to inorganic solids. However, the issue of the degradation of semiconducting polymers represents a practical problem for the fabrication of effective semiconducting polymer-based intrinsic, direct detectors. In fact, these detectors base their operability on the measurement of the resistivity (conductivity) of the polymeric semiconductor, which increases (decreases) upon device exposure to the ionizing radiation, due to material degradation. This means that the above described devices are not able to perform for prolonged periods, neither to be repeatedly used with reproducible performance, hence resulting in detectors with a very short operative lifetime and, in the best possible case, as disposable devices. [**6**]

A first step towards the solution of these problems was made recently, when semiconducting polymer-based drop-cast films with a thickness of approximately 10–20 mm showed linearity up to dose rates of 60 mGy/s. The sensitivity of these devices reached values of 100–400 nC $mGy^{-1}cm^3$, which are comparable to silicon devices. [**14**] The time response of the X-ray photocurrent measured for the thin film devices was less than 150 ms, and no sign of radiation damage was observed for doses in excess of 10 Gy, although no information on the reproducibility of the results was reported. Though the authors of these reports do not always mention it explicitly, it has to be noted that in these devices the polymeric semiconductor thin films are always coupled to metallic electrodes or substrates, which are exposed to the ionizing radiation together with the organic layer. The importance and the role of the metallic electrodes and/or the substrate in the performance of these devices has been stressed in several dedicated works, since they act as the primary X-ray

photo-conversion layers, producing secondary electrons which are injected into the organic thin film and thus produce the electrical signal output. [**6**] [**14**] [**15**]

A study that regards semiconducting thin film-based detectors and is worth mentioning, is reported in the article written by *Intaniwet et al.* [**16**]. In this article the authors performed a study on poly(triarylamine) (PTAA)-based X-ray detectors. In these devices a single layer of PTAA is deposited on indium tin oxide (ITO) substrates, with top electrodes selected from Al, Au and Ni. Results show that the choice of electrode contact material has a large effect on device performance. A high rectification Schottky diode can be achieved using a metal with a work function lower than the HOMO level of the polymer. The resulting higher barrier height metal-polymer contact produces a fast time-independent response with very stable photocurrent output and a high signal-to-noise ratio. When using PTAA, it was found that Al is very suitable for the metal contact. In contrast, diodes with lower barrier heights, fabricated with either Au or Ni contacts, show a long-lived, slow transient response to X-ray irradiation, because of X-ray-induced charge injection and the build-up of space charge close to the metal-polymer interface (Figure 2.5). Therefore, when selecting the material for the contacts on a polymeric sensor, the metal's work function should lie between the HOMO and LUMO levels of the chosen polymer. [**16**]

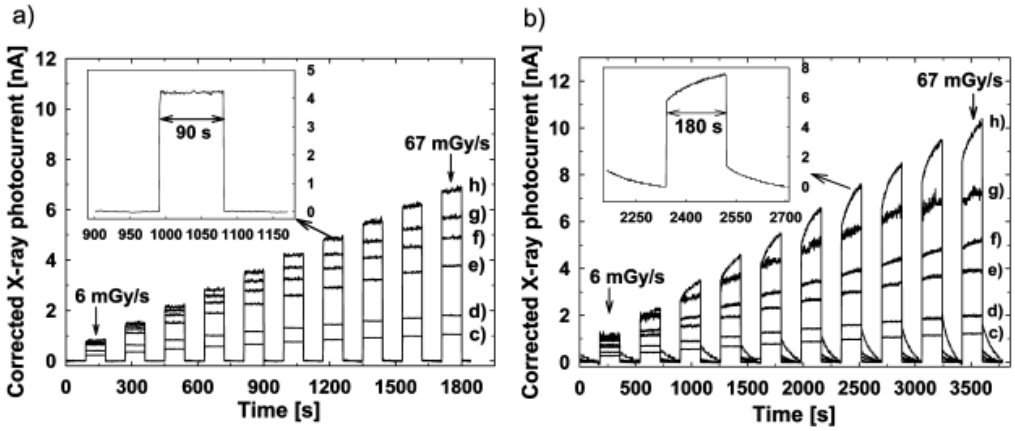

Figure 2.5: Response of the ITO/PTAA/metal sensors, with 30 µm thick PTAA layers, upon exposure to 17.5 keV X-rays through (a) Al and (b) Au top contacts with dose rates increasing over time (6, 13, 20, 27, 33, 40, 47, 54, 60, and 67 mGy/s). The devices are exposed to X-radiation for 90 s for the Al contact and for 180 s for the Au contact. Operational voltages: (c) 10, (d) 20, (e) 60, (f) 100, (g) 150, and (h) 300 V. Insets: magnified plot of a single response when exposed to an X-ray dose rate of 47 mGy/s and operated at 300 V. [16**]**

2.5 Solid state detectors based on organic single crystals

Although the studies reported in literature are still few, OSSCs are very promising materials to directly detect X-ray radiation, as their particular properties overcome most of the major limitations inherent to organic materials discussed previously. For example, their long range molecular packing order and lack of grain boundaries impart unique transport properties to all OSSCs such as high carrier mobilities (up to 40 $cm^2V^{-1}s^{-1}$), transport anisotropy and long exciton diffusion lengths (up to 8 mm, as opposed to the few nanometers in organic thin films and blends used in photovoltaic and photodetecting devices). These features, coupled with their high resistivity and low dark currents

due to the relatively large band gap, are enhanced, in the case of solution-grown OSSCs, by the possibility of tuning the crystal dimensions up to mm^3. Moreover, a notable unique property of OSSCs is that they can efficiently and intrinsically photo-convert X-ray photons into an electrical signal, without the need for the intervention of extra metal/substrate layers. [**6**]

Among the articles reported in literature, *Fraboni et al.* [**11**] reported devices based on solution-grown OSSCs (from two different molecules: 4-hydroxycyanobenzene (4HCB, Figure 2.6 a,b) and 1,8-naphthaleneimide (NTI ,Figure 2.6 c,d). These samples have been fabricated and operated in air, under ambient light and at room temperature, at voltages as low as few volts, delivering well reproducible performances and a stable linear response to the X-ray dose rate.

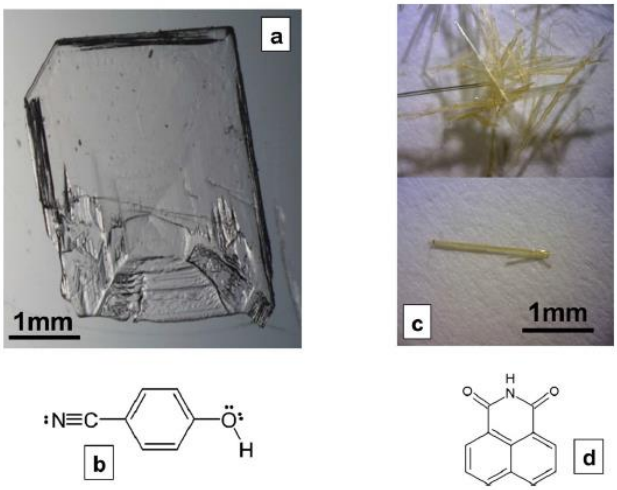

Figure 2.6: optical microscopy images (a,c) and molecular structure (d,b) of single crystals of 4HCB and NTI. [11**]**

Moreover, in the same article the authors show that the detectors' response may be influenced by the emission of secondary electrons from high- Z electrodes or substrates. Considering Figure 2.7, it is evident that the collected electrical signal is larger when the electrodes are exposed, possibly due to an extra contribution of secondary electrons released by the interaction of the X-rays with the metal electrodes. The same behavior has been observed for various combinations of substrates (quartz, SiO_2, Cu), metal electrodes (Ag, Au, Cu), and geometries, thus assessing that high- Z substrates and/or electrodes give a non-negligible contribution to the collected electrical signal. However, the fabrication of all-organic devices with the aim to remove the possible contribution from higher-atomic-number device components, demonstrated that the signal is comparable to that obtained from devices with shielded metallic electrodes. This confirms that organic single crystals exposed to X-rays can directly convert the incoming radiation into an electrical signal with no need for additional high-Z components in the device. [**11**]

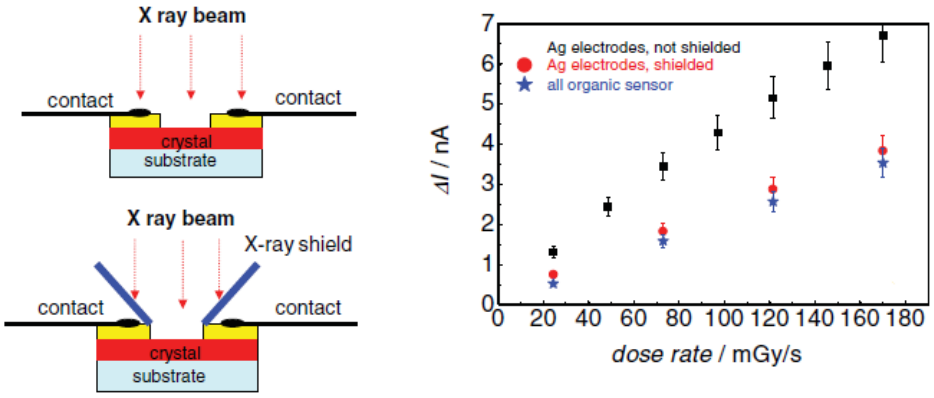

Figure 2.7: Left: sketched of the two different measurement configurations used to probe the detectors, that is, with unshielded (upper panel) and shielded (lower panel) metallic electrodes. Right: comparison of the $\Delta I=I_{on}-I_{off}$ response vs the dose rate for a device with shielded (solid red circles) and unshielded (solid black squares) Ag electrodes, compared with all-organic identical geometry device (solid blue stars). [11]

Another study that is reported in [**6**] and is worth mentioning, regards the investigation of the role and the effects of the molecular anisotropic packing in the X-ray photo-response of OSSCs. In this article the authors report two samples: one based on 4HCB and one based on 1,5-dinitronaphthalene (DNN) molecules, which have been chosen because they generate crystals with different geometries (platelets in the case of 4HCB and needles for DNN). Although the results show that the crystal shape and geometry does not affect the detector performance, the anisotropic packing of the molecule affects the electronic transport properties of the crystal, inducing a carrier mobility which can vary up to 4 orders of magnitude along the three crystal axes in the 4HCB. However, it is noteworthy that all axes can be used for the effective detection of ionizing radiation. Interestingly, in 4HCB crystals, the largest sensitivity is obtained in the vertical geometry, even if in this configuration the electrodes do not connect the crystal axis with the best molecular π-stacking and carrier mobility, as shown in Figure 2.8. In the same figure a sketch of the planar geometry, which is the electrodes geometry of most of the samples under test in this experimental work, is also reported. [**6**]

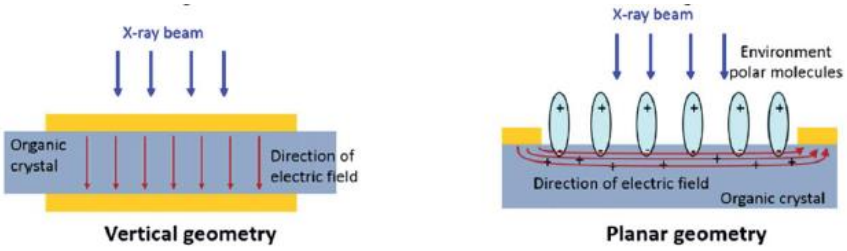

Bias (V)	Sensitivity (nC/Gy)		
	@10V	@50V	@100V
Planar	7	18	28
Vertical	24	49	70

Figure 2.8: Sketch of the electric field distribution in the vertical and planar geometry in 4HCB samples (upper panel). Sensitivity values in both configurations for three bias voltages. [6]

3 Materials and methods

In this chapter the general procedure adopted throughout the experimental work will be described. The samples preparation method, including description of materials and tools employed, will be treated in subsection 3.1. Subsequently, in subsection 3.2, the measurement setup will be described. The measurement and data analysis procedures will be illustrated respectively in subsections 3.3 and 3.4. In closing, the characterization results of the reference devices will be shown in subsection 3.5.

3.1 Sample preparation

Initially placed on a glass substrate, the organic single crystal is fixed by its edges using Ag paste. Subsequently, a 50 µm diameter Au wire is placed crosswise on the crystal as a shadow mask, in order to create a channel between the metal electrodes fabricated by means of vacuum evaporation. The metal deposition process is performed in a high vacuum chamber (10^{-5} torr), using either gold or silver as deposition material (150 mg). Initially, the metal is properly placed on a filament inside the chamber. At the pressure of 10^{-2} torr, achieved with a rotary pump, metal drops are created by heating the filament. Subsequently, the chamber is opened and the samples are placed on their support. At the pressure of 10^{-5} torr, achieved with a turbomolecular pump, the deposition is performed. Figure 3.1 shows an example of a crystal after the deposition process.

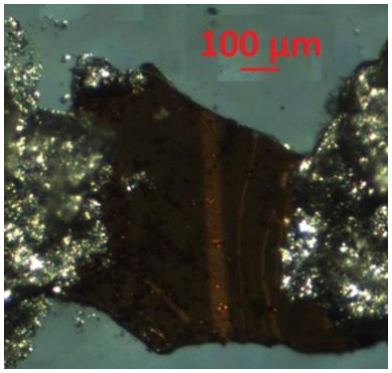

Figure 3.1: Image taken with the optical microscope showing a single crystal after the deposition process. As can be seen, it is possible to identify the channel.

After the deposition process, the organic crystal is electrically contacted using gold wires (Figure 3.2) and connected inside an aluminum case. The sample is therefore ready to be characterized under X-rays.

a) 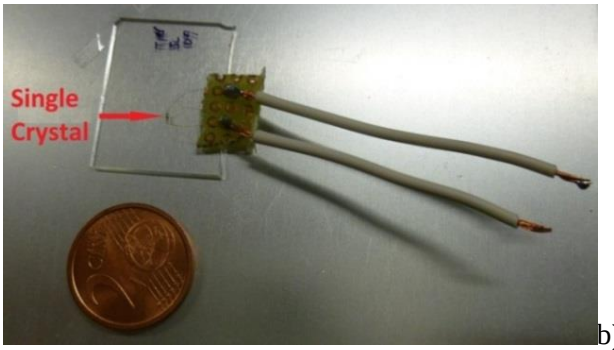

b) 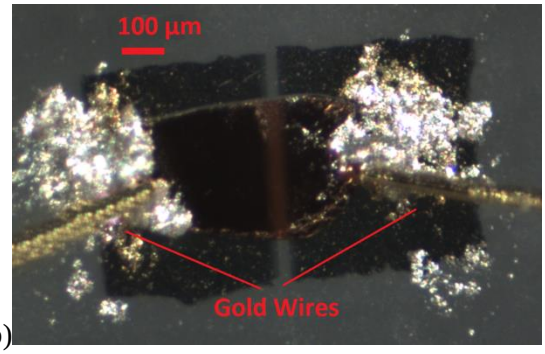

Figure 3.2: a) Image of a complete sample and b) enlargement of the crystal area, where it is possible to identify the gold wires.

3.2 Measurement setups

The most of the measurements will be performed with the samples exposed to X-rays. However, in the case of two samples (TIPSSC_07 and Rux), we will perform measurements using a LED of 375 nm wavelength. This will be done in order to compare both responses, with the aim to reach a better interpretation of the photoconversion process occurring in X-ray detectors. In fact, although controversial, the dynamic of photoconversion of visible photons in organic materials has been already treated in literature [**17**] [**18**]. On the other hand, the interaction mechanism between organic materials and X-rays is less known.
In this subsection the measurement setups employed in the case of both X-ray irradiation and LED illumination will be described.

3.2.1 Measurement setup (X-rays)

A schematic of the measurement setup is reported in Figure 3.3.

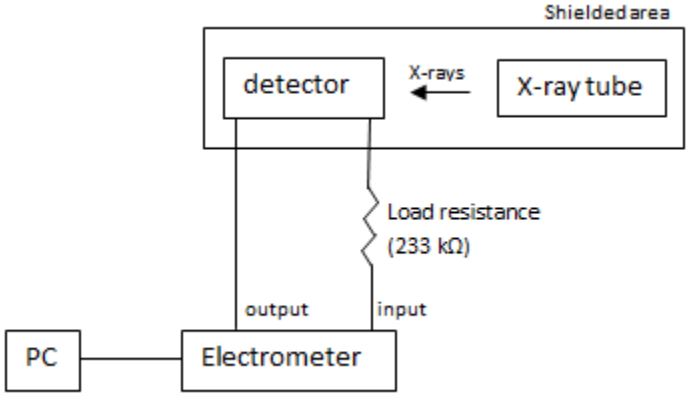

Figure 3.3: schematic of the measurement setup.

The detector is placed in a shielded area at the distance of 21 cm from a molybdenum X-ray tube (PANalytical[2], PW 2285/20), which operates at a voltage of 35 kV and at the current defined by the user (5 mA : 30 mA). The electrometer (Keithley[3], mod. 6517A) is connected to both the detector and a PC, allowing the user to interface with the system through the LabView software.
Figure 3.4 shows an image of the shielded area, where it is possible to identify the X-ray tube and the aluminum case containing the sample under test.

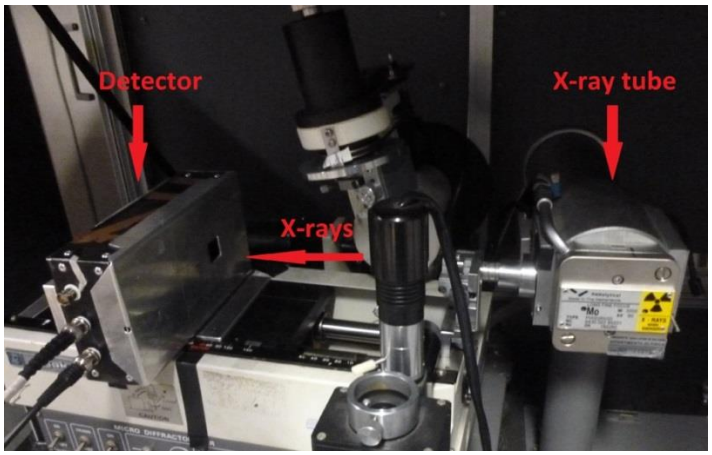

Figure 3.4: shielded area.

Samples are therefore subjected to a dose rate that depends on the X-ray tube's operation current. Figure 3.5 shows the dose rate-current calibration graph and Table 3.1 shows numerically the relation between the current and the dose rate at the distance of 21 cm from the beam source.

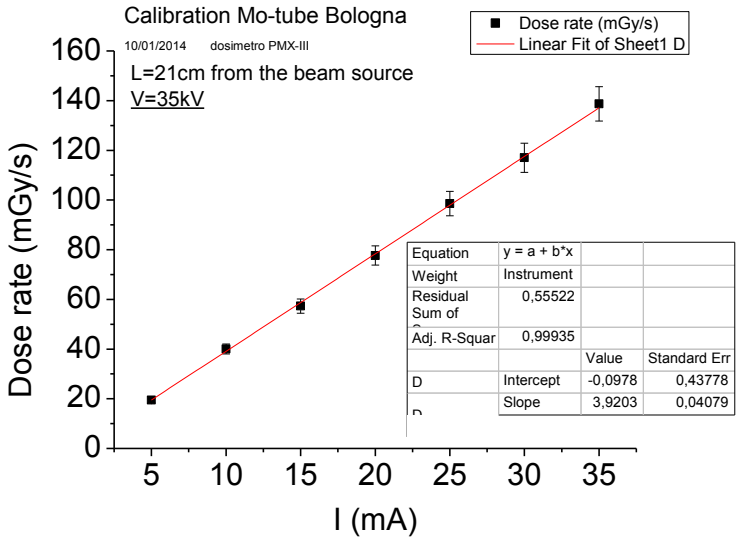

Figure 3.5: Calibration of the Mo-tube. Dose rate vs current.

[2] www.panalytical.com
[3] www.keithley.it

Current (mA)	Dose rate (mGy/s)
5	19.4
10	40.0
15	57.3
20	77.7
25	98.6
30	117.0
35	138.7

Table 3.1: Relation between current and dose rate at the distance of 21 cm from the beam source.

The sample under test will be subjected to a given incident photon flux, that can be calculated by means of a proper X-ray spectra simulator[4] developed by Siemens. By setting the anode material, the X-ray tube operation voltage and the dose rate it is possible to obtain the photon flux, as reported in Table 3.2.

Dose rate (mGy/s)	Photon Flux Φ ($cm^{-2}s^{-1}$)
19.4	$2.98 \cdot 10^{10}$
40.0	$6.16 \cdot 10^{10}$
57.3	$8.82 \cdot 10^{10}$
77.7	$1.20 \cdot 10^{11}$
98.6	$1.52 \cdot 10^{11}$
117.0	$1.79 \cdot 10^{11}$
138.7	$2.14 \cdot 10^{11}$

Table 3.2: Relation between dose rate and photon flux.

For a given incident photon flux Φ (expressed in $cm^{-2}s^{-1}$), the photocollection efficiency of the sample is given by:

$$f = \frac{\Delta I}{A \Phi \beta (2e)} \qquad \textbf{Equation 3.1}$$

where ΔI is the difference between the current under irradiation and the dark current, A is the channel area of the crystal, e is the electron charge and β is the ratio between the photon energy and the energy of pair creation (2.5 times the bandgap). [**11**] The previous quantities and the photocollection efficiencies of the TIPSSC_07 and the RUX samples exposed to X-rays at the dose rate of 98.6 mGy/s are reported in Table 3.3.

[4] https://w9.siemens.com/cms/oemproducts/Home/X-rayToolbox/spektrum/Pages/Default.aspx

Sample	Photon energy (ev)	Dose rate (eV gr^{-1} s^{-1})	Photon flux ($cm^{-2}s^{-1}$)	Channel area (cm^2)	ΔI (A)	Energy gap (ev)	β	**f (%)**
TIPSSC_07	$1.70 \cdot 10^4$	$6.16 \cdot 10^{14}$	$1.52 \cdot 10^{11}$	$5.0 \cdot 10^{-5}$	$4.10 \cdot 10^{-10}$	2	3400	**4.96**
Rux				$6.0 \cdot 10^{-4}$	$1.10 \cdot 10^{-9}$	2.2	3090	**1.22**

Table 3.3: Photocollection efficiencies for the TIPSSC_07 and Rux samples at the X-ray dose rate of 98.6 mGy/s.

3.2.2 Measurement setup (LED)

The LED employed for the measurements (HWA/WYS ultrafire[5] mod. wf-501B) is characterized by a wavelength of 375 nm. A picture of the measurement setup is reported in Figure 3.6.

a) 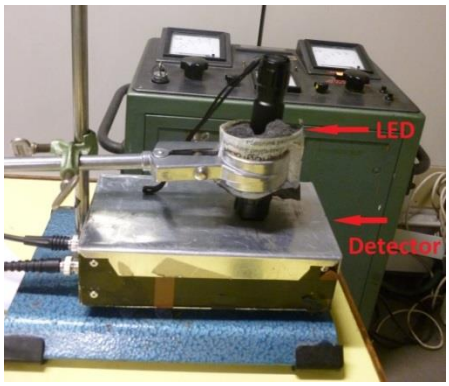

b) 

Figure 3.6: a) Measurement setup for the LED measurements; b) sample under illumination.

The photon flux is calculated by using a silicon-based UV photodiode of 2.5 mm diameter supplied by EOS[6] (Figure 3.7).

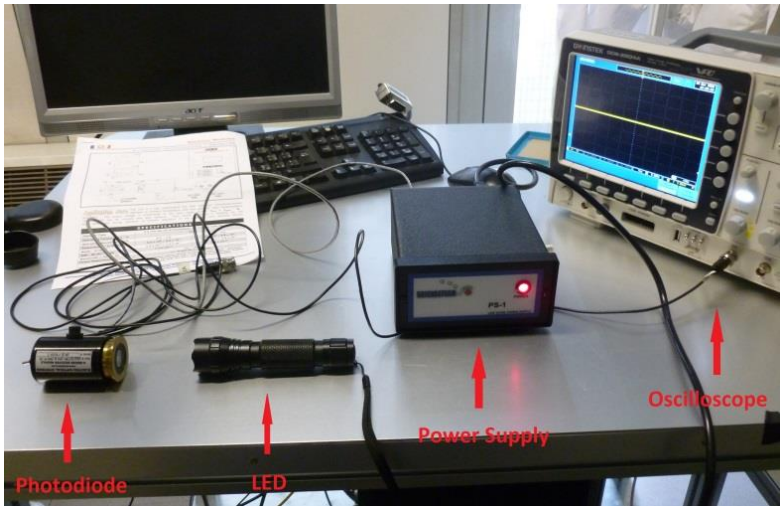

Figure 3.7: measurement set up for the LED photon flux calculation.

[5] www.ultrafire.net
[6] www.eosystems.com

When the LED is switched on, the ΔV induced by the LED to the photodiode can be appreciated by means of the oscilloscope (GW Instek[7] mod. GDS-2204A). At the distance of 5: 20 cm between the LED and the photodiode, the ΔV does not change significantly and is equal to 14V (Figure 3.8).

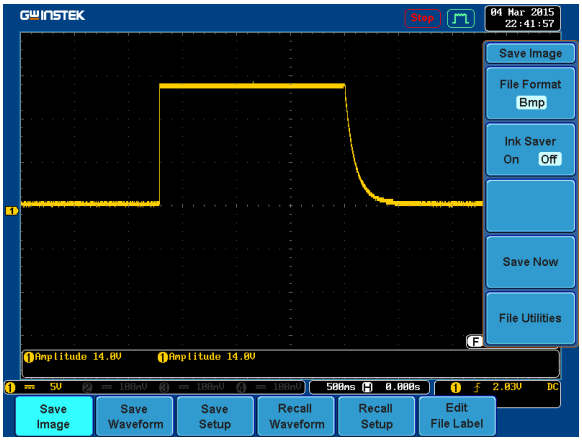

Figure 3.8: The ΔV induced by the LED to the photodiode can be appreciated on the oscilloscope's screen.

Since the responsivity of the photodiode at 375 nm is equal to $204 \cdot 10^5$ V/W, the incident power is given by:

$$Incident\ power = \frac{\Delta V}{Responsivity} = \frac{14\ V}{204 \cdot 10^5\ \mathrm{V/W}} = 6.86 \cdot 10^{-7}\ W \qquad \textbf{Equation 3.2}$$

Since the area of the photodiode is equal to 0.049 cm^2, the irradiance (incident power per unit area) is given by:

$$Irradiance\ = \frac{Incident\ power}{Incident\ Area} = \frac{6.86 \cdot 10^{-7} W}{0.049\ cm^2} = 1.4 \cdot 10^{-5}\ W/cm^2 \qquad \textbf{Equation 3.3}$$

The energy of the incident photon is equal to:

$$E_{photon} = \frac{hc}{\lambda} = \frac{1.989 \cdot 10^{-25}}{0{,}375 \cdot\ 10^{-6}} = 5{,}304 \cdot\ 10^{-19}\ J \qquad \textbf{Equation 3.4}$$

Therefore the photon flux is given by:

$$\Phi = \frac{Irradiance}{E_{photon}} = \frac{1.4 \cdot 10^{-5} W/cm^2}{5{,}304 \cdot\ 10^{-19}\ J} = \mathbf{2.64 \cdot 10^{13}\ photons\ \cdot s^{-1} \cdot cm^{-2}} \qquad \textbf{Equation 3.5}$$

[7] www.gwinstek.com

The photocollection efficiencies of the TIPSSC_07 and Rux samples under LED illumination can be calculated as reported in the previous subsection. However, in the case of visible photons β is considered equal to one (Table 3.4).

Sample	Photon flux ($cm^{-2}s^{-1}$)	Channel area (cm^2)	ΔI (A)	β	**f (%)**
TIPSSC_07	$2.64 \cdot 10^{13}$	$5.0 \cdot 10^{-5}$	$3.50 \cdot 10^{-9}$	1	**829**
Rux		$6.0 \cdot 10^{-4}$	$7.0 \cdot 10^{-8}$	1	**1381**

Table 3.4: photocollection efficiencies for the TIPSSC_07 and Rux samples under LED illumination.

It must be pointed out that in the case of organic photoconductors, photocollection efficiencies higher that 100% have been already obtained and discussed in literature. This high values can be obtained because one of the two generated carriers, typically electrons, remain trapped in the material, accumulating and giving rise to a space charge region. Therefore, in order to maintain the neutrality the electrodes inject a greater number of holes. [**19**]

3.3 Measurement procedure

In order to obtain a complete characterization of the device under test, different measurements have to be performed. The parameters needed for the data acquisition are defined by the user through LabView programs. Under irradiation, the sample is kept in the dark and at room temperature. The first measurements, which can be performed with the X-ray beam switched either on or off, allow to obtain current-voltage (I-V) characteristics of the device. In this measurements the user has to define, through the LabView program, the bias voltage range (for example -20 V : 20 V) and the current sampling interval (for example 0.5 V). Figure 3.9 shows an example of two I-V characteristics, taken with the X-ray beam off. As can be seen, this measurements allow to evaluate the dark current behavior and its entity. As discussed in subsection 2.3, a low dark current is critical for low noise operation.

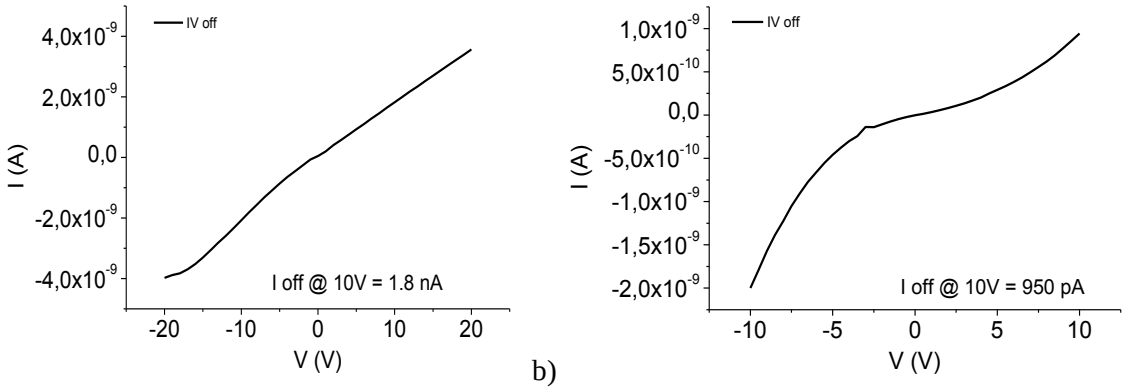

Figure 3.9: Examples of I-V characteristics showing a a) ohmic-like behavior and a b) Schottky-like behavior.

Subsequently, repeated I-V X-ray off measurements can be performed in order to evaluate the presence of the bias stress effect, i.e. the current-voltage characteristic change that can occur after

the application of prolonged voltages [**20**]. Figure 3.10 shows an example of repeated I-V curves with the X-ray beam off. As reported, at the bias voltage of 50 V the difference in the current entity between the first and the last measurement is equal to 0.13 nA.

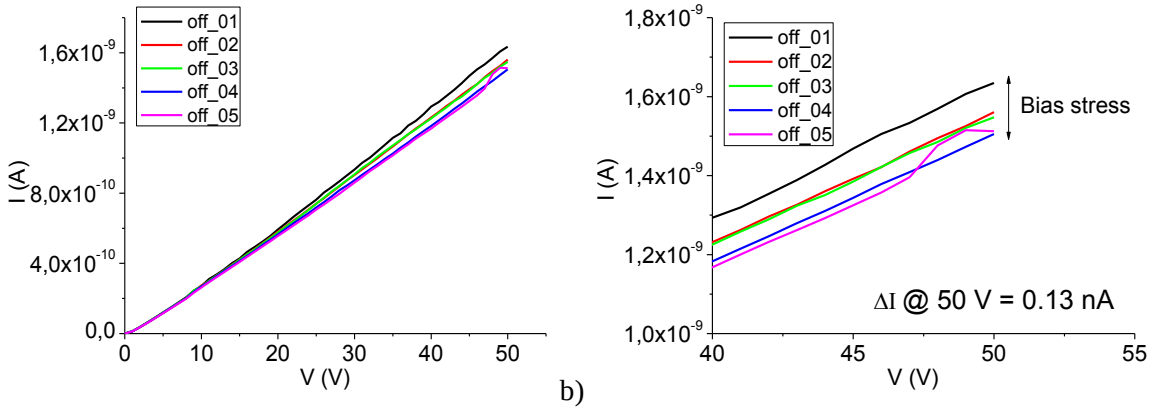

Figure 3.10: a) repeated I-V X-ray off curves showing bias stress. b) extension of the 40V : 50V range.

The second type of measurements is performed in order to obtain the current dynamical response (current versus time behavior). In this case, during the acquisition the X-ray beam is cyclically switched on and off . Since through the LabView program it is possible to set the bias voltage, this measurements allow to evaluate the dynamical response at different bias voltages (Figure 3.11). In Figure 3.11a it is possible to ascertain the presence of current drift, while in Figure 3.11b the current shows a slow behavior during the charge and discharge steps. As can be seen, both phenomena are more evident as the bias voltage increases.

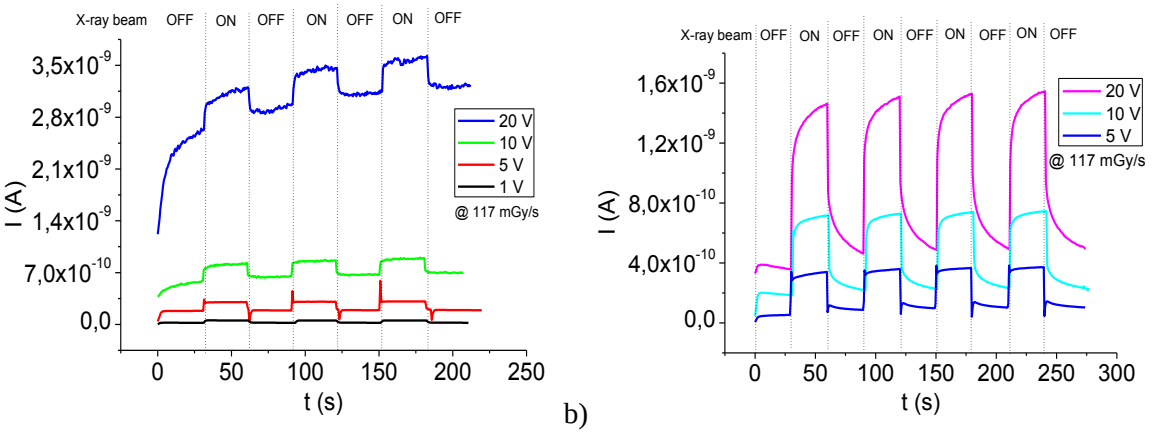

Figure 3.11: Examples of repeated X-ray beam on/off cycles (30 sec OFF – 30 sec ON). a) Presence of current drift. b) Slow charge and discharge behavior.

Through this measurements it is also possible to evaluate the response time of the device, i.e. the time constants related to both the rise and the decay part of the curve. This study is usually carried out when the current shows a slow charge and discharge behavior: as it will be shown, in order to obtain the time constants an exponential fit is performed in correspondence to the rise and decay

steps of the curves. Therefore, in this case the previous measurements are performed by acquiring only one X-ray off-on-off cycle with longer times, in order to obtain a more accurate and statistically reliable acquisition. Figure 3.12 shows an example of one X-ray off-on-off cycle where the current dynamical behavior is shown for different bias voltages.

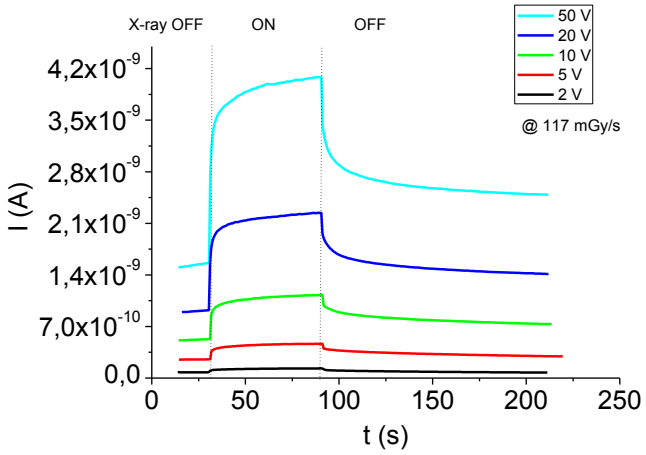

Figure 3.12: Example of one X-ray off/on/off cycle (1 sec OFF – 1 min ON – 2 min OFF).

The third type of measurement (Sweep Voltage measurement), similarly to the previous case, allows to obtain the current versus time behavior: during the acquisition, the bias voltage is periodically increased as defined by the user through the LabView program. Correspondingly to each voltage step, the X-ray beam is switched on and kept on for a given time. The measure is repeated for each dose rate, as reported in Figure 3.13. In the example shown, the bias voltage increases according to the following steps: 5 V, 10 V, 20 V, 50 V, 100 V, 150 V.

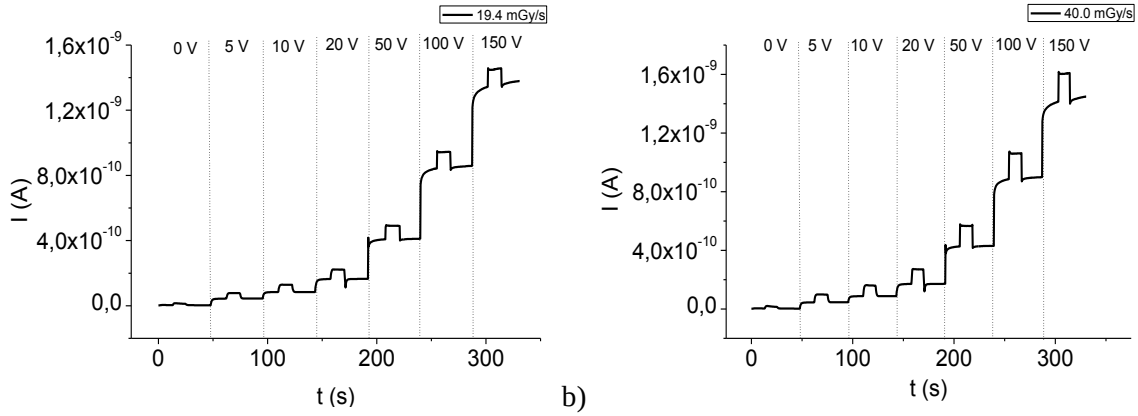

a) b)

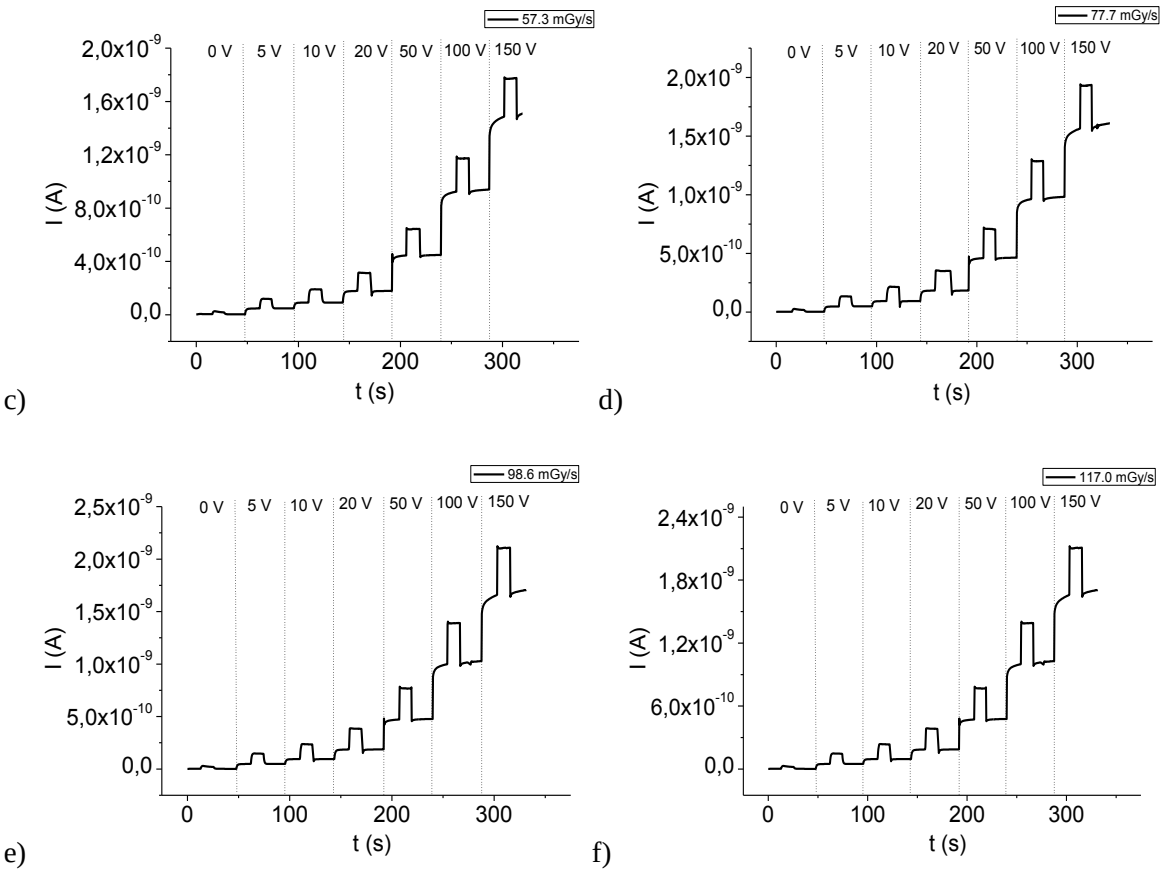

Figure 3.13: Examples of current versus time behavior increasing periodically the bias voltage (0 V, 5 V, 10 V, 20 V, 50 V, 100 V, 150 V). Correspondingly to each bias voltage step, the X-ray beam is switched on and kept on for a given time. The measure is repeated for different dose rate: a) 19.4 mGy/s ; b) 40.0 mGy/s; c) 57.3 mGy/s; d) 77.7 mGy/s; e) 98.6 mGy/s; f) 117.0 mGy/s.

3.4 Data analysis

After the acquisition process, the data are elaborated through the Origin software. The data analysis basically consists in calculating the sensitivity by means of the graphs reported in Figure 3.13. The sensitivity, which is defined as the detector's capability of producing a usable signal for a given type of radiation and energy [**13**], can be expressed by the following formula:

$$Sensitivity = \frac{\Delta I}{Dose\ rate} \qquad \textbf{Equation 3.6}$$

Correspondingly to each bias voltage step, the difference $\Delta I = I_{on} - I_{off}$ is calculated and plotted as a function of the dose rate. Subsequently, a linear fit is performed and the slope of the line gives the sensitivity, as shown for example in Figure 3.14 (in the table reported the slope is expressed in C/mGy). The error on the sensitivity is given by the software and corresponds to the error on the slope of the linear fit.

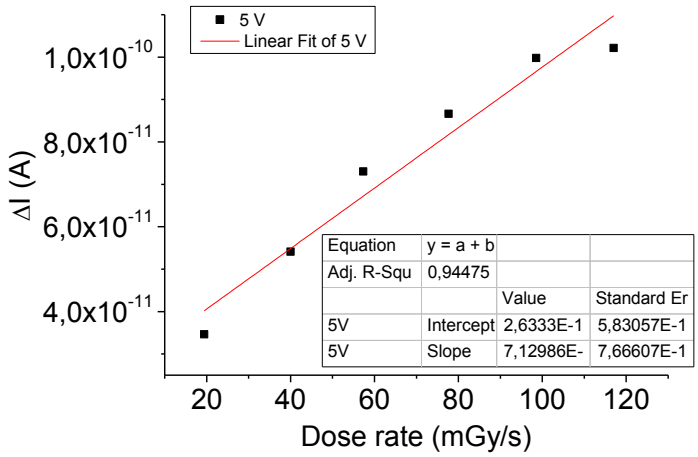

a)

Figure 3.14: ΔI vs dose rate: example of linear fitting in the case of 5 V.

In order to obtain the sensitivity related to each bias voltage, the latter procedure is then repeated for each bias voltage, as shown for example in Figure 3.15.

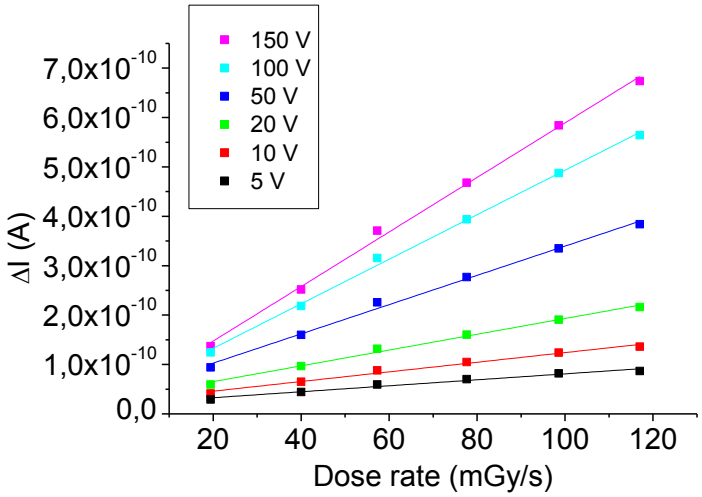

Figure 3.15: ΔI vs dose rate: example of linear fitting for each bias voltage.

Furthermore, the data analysis could consist in calculating the signal-to-noise ratio, that can be plotted for example as a function of either the dose rate or the bias voltage. It is defined as

$$SNR = \frac{\Delta I}{I_{off}} \qquad \textbf{Equation 3.7}$$

.

As mentioned in the last subsection, if the dynamical response of the current shows a slow charge and discharge behavior it is possible to study the response time of the device. In order to obtain the time constants an exponential fit is performed in correspondence to the rise and decay of the curve. In our case the best fit is usually obtained by fitting with a double exponential of the form:

$$y = y_0 + Ae^{-x/t1} + Be^{-x/t2}$$ **Equation 3.8**

An example of the exponential fit is reported in Figure 3.16 in the case of the rise step and in Figure 3.17 in the case of the decay step. In both examples, the two times (t_1 and t_2) are reported in milliseconds.

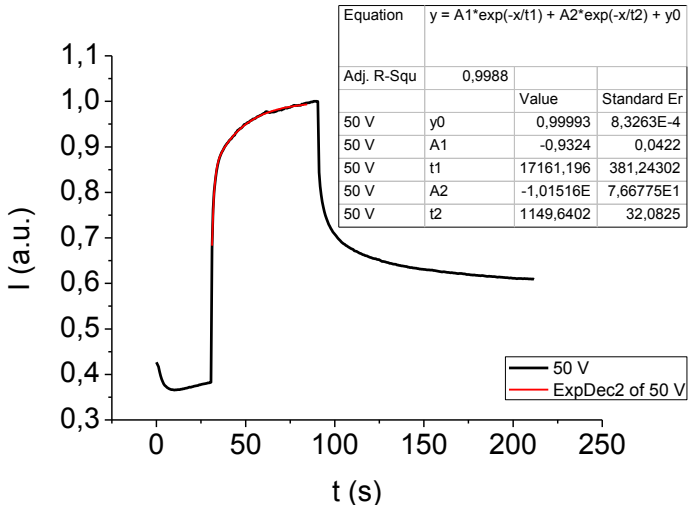

Figure 3.16: example of exponential fit in the case of the rise step.

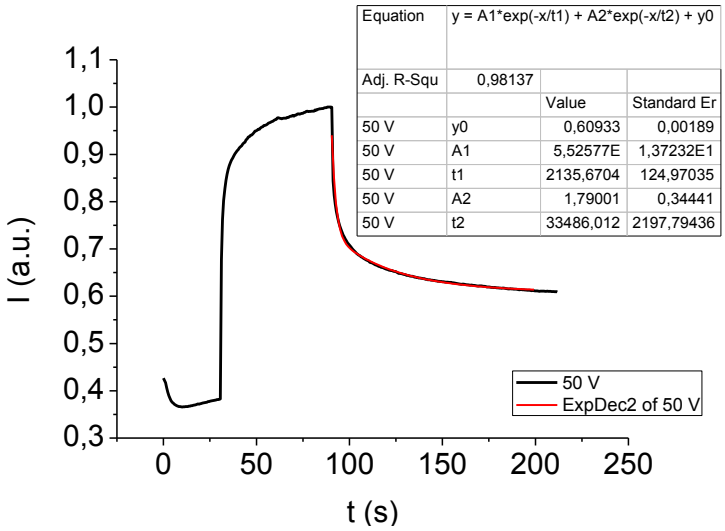

Figure 3.17: example of exponential fit in the case of the decay step.

3.5 Characterization of the reference devices

As we have seen in subsection 3.4, the detector's figures of merit allow to evaluate the detector's response. In order to define if this response is significant, it is necessary to determine some reference values of these figures of merit. The reference values can be obtained by characterizing "reference" devices, i.e. which do not involve any crystal, in order to quantify the device response

due to the interaction between radiation and the substrate/electrodes (subsection 2.5). This response will therefore be taken into account when we will evaluate the detectors' performances. Aiming at defining this reference values, four reference devices (Reference_01, Reference_02, Reference_03, Reference_04) have been characterized. All the samples have a planar geometry where the gold is deposited on the glass substrate and a channel, with the same length of that realized onto crystal surface, separates the two electrodes. We report, as an example, the characterization results related to the Reference_02 sample and we will summarize the results related to the other samples in a table. A picture of the Reference_02 sample, taken with the optical microscope, is reported in Figure 3.18.

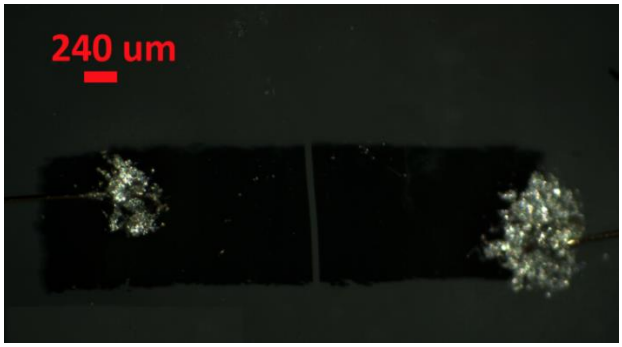

Figure 3.18: Picture of the Reference_02 sample taken with the optical microscope.

Figure 3.19a shows the dark current behavior between 0 V and 20 V. The dynamical behavior of the current, obtained with X-ray beam on/off cycles is reported in Figure 3.19b for different bias voltages.

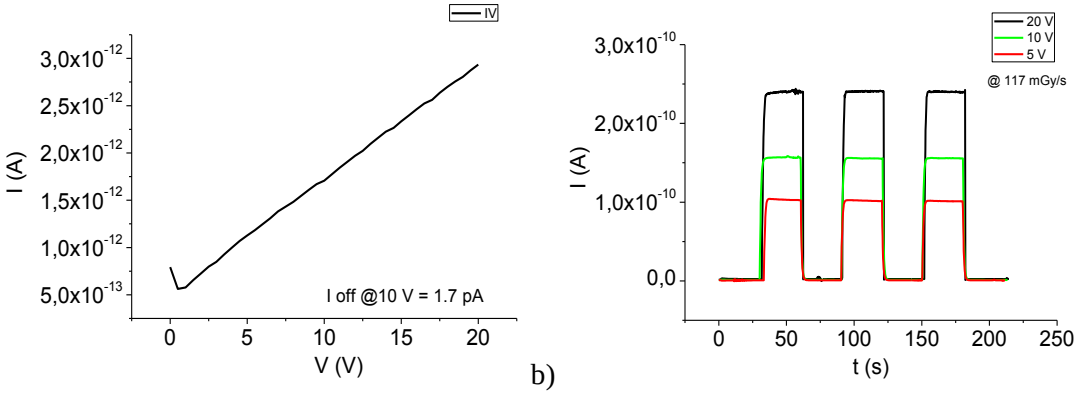

Figure 3.19: a) dark current behavior between 0 V and 20 V and b) dynamical response at different bias voltages.

The ΔI plotted as a function of the dose rate is shown in Figure 3.20a for different bias voltages. As reported, the maximum ΔI obtained at 10 V is equal to 155 pA. The sensitivity values plotted as a function of the bias voltage are shown in Figure 3.20b and reported in Table 3.5. At 10 V of applied voltage a sensitivity of (1.09 ± 0.04) nC/Gy has been calculated.

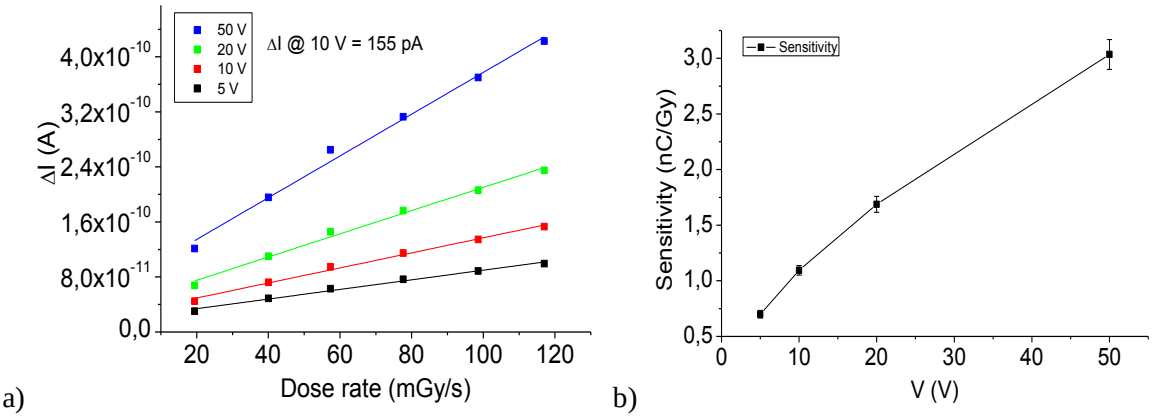

Figure 3.20: a) ΔI response for different bias voltages and b) Sensitivity vs bias voltage (White_02).

Bias voltage (V)	Sensitivity (nC/Gy)	Std error (nC/Gy)
5	0.70	0.03
10	**1.09**	**0.04**
20	1.69	0.07
50	3.03	0.13

Table 3.5: Sensitivity values (White_02).

Considering the 10 V bias voltage as the reference voltage, the most important results (I_{off}, ΔI, sensitivity) related to each reference device are reported in Table 3.6.

Sample	I_{off} @ 10V (pA)	Sensitivity @ 10 V (nC/Gy)	ΔI @ 10 V @ 117 mGy/s (pA)
reference_01	1.4	0.93 ± 0.04	127
reference _02	1.7	1.09 ± 0.04	155
reference _03	1.4	1.22 ± 0.07	184
reference _04	2.5	0.95 ± 0.03	133

Table 3.6: Characterization results of the white samples.

The results are then averaged and shown in Table 3.7. In this case the errors are calculated as

$$\sigma = \frac{X_{max} - X_{min}}{2}$$ **Equation 3.9**

Sample	Average I_{off} @ 10V (pA)	Average Sensitivity @ 10 V (nC/Gy)	Average ΔI @ 10 V @ 117 mGy/s (pA)
Reference_ 01/02/03/04	1.75 ± 0.55	1.04 ± 0.15	150 ± 28

Table 3.7: Average values related to the reference devices.

As we can deduce from Table 3.7, a sensitivity and a ΔI significantly greater than those reported will be needed in order to define the detector's response as meaningful. Moreover, as we will see in the case of few samples, if a device shows a dark current comparable with that reported there could be the absence of charge carrier injection through the metal-semiconductor interface.

4 Characterization of TIPS-based detectors

The TIPS-Pentacene (6,13-bis(triisopropylsilylethynyl)pentacene) is an apolar and high mobility crystal, which molecular structure is reported in Figure 4.1. In this chapter the characterization results of four TIPS Single Crystal-based (TIPSSC) devices will be illustrated. The first two samples (TIPSSC_01 and TIPSSC_02) have Au electrodes in planar geometry and have been grown using dichlorobenzene as solvent, at the concentration of 1%. The third sample (TIPSSC_07) has a planar Ag electrodes geometry and has been grown employing Tetralin as solvent at the concentration of 5.75 mg/mL. The last sample (TIPSSC_09) has Au electrodes in planar configuration and has been growth using Tetralin as solvent at the concentration of 4.9 mg/mL. All these information are summarized in Table 4.1.

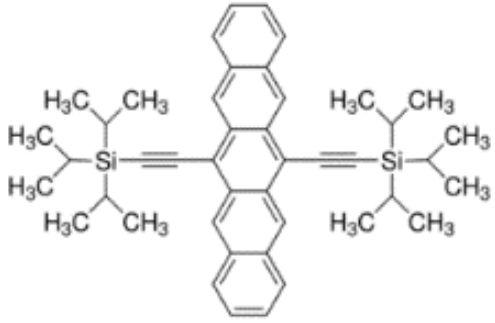

Figure 4.1: TIPSSC molecular structure.

Sample	Electrodes geometry	Solvent
TIPSSC_02	planar Au	DCB 1%
TIPSSC_01	planar Au	DCB 1%
TIPSSC_07	planar Ag	Tetralin 4.9 mg/mL
TIPSSC_09	planar Au	Tetralin 5.75 mg/mL

Table 4.1: Features of the samples under test.

4.1 TIPSSC_01 – Planar Au electrodes (Solvent DCB 1%)

The first TIPS-based sample under test is the TIPSSC_01, which has a planar configuration with gold electrodes and have been grown using dichlorobenzene as solvent at the concentration of 1%. An image of the TIPSSC_01 sample, taken with the optical microscope, is reported in Figure 4.2. Figure 4.2a shows the whole crystal with the gold electrodes and through Figure 4.2b it is possible to recognize the channel region, located between the red lines.

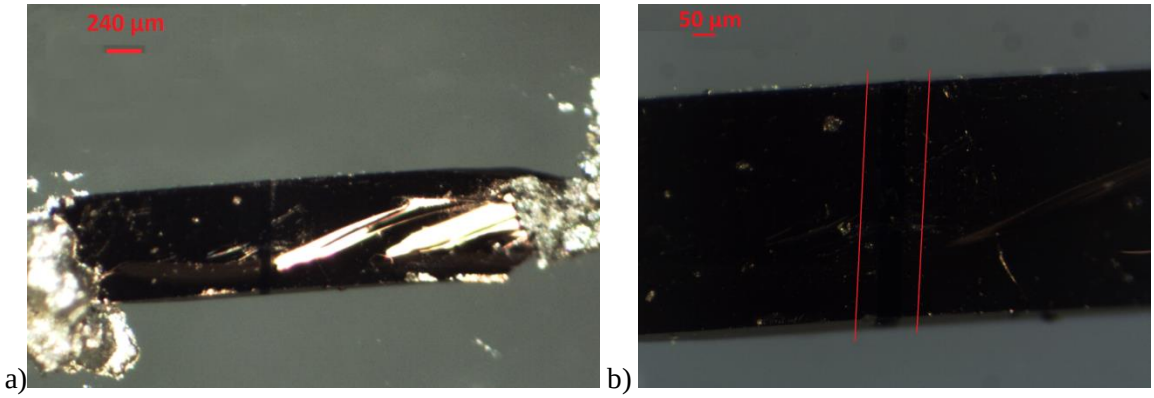

a) b)

Figure 4.2: image of the TIPSSC_01 sample with gold electrodes: a) whole crystal and b) channel region.

The dark current behavior between 0 V and 100 V is reported Figure 4.3a, where we can observe that the relation between the current and the applied voltage follows an ohmic behavior. Moreover, due to the low leakage current we can deduce that this sample is characterized by a low noise. The dynamical behavior of the current, obtained with X-ray beam on/off cycles is reported in Figure 4.3b. As shown, the sample response is fast for all the applied voltages involved.

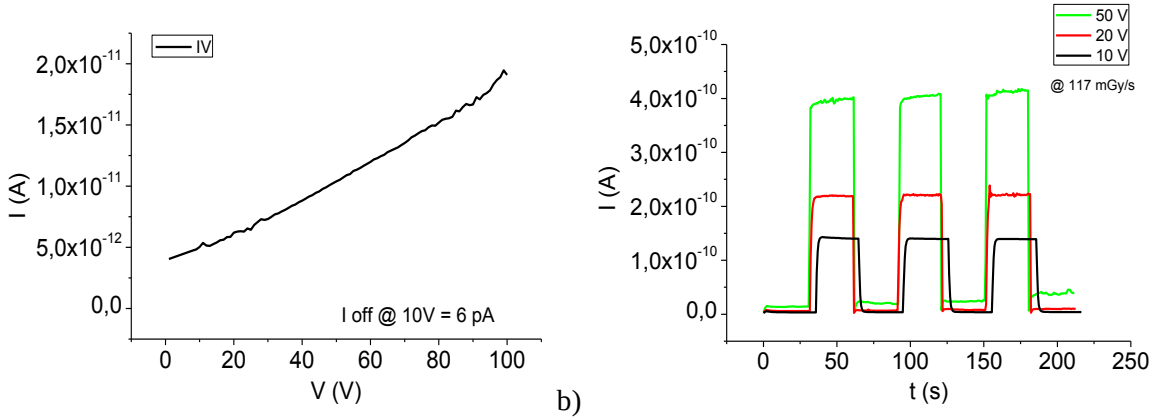

a) b)

Figure 4.3: a) Dark current behavior between 0 V and 100 V; b) dynamical response at different bias voltages for the TIPSSC_01 sample.

The ΔI response and the sensitivity values plotted as a function of the applied voltage are shown in Figure 4.4.

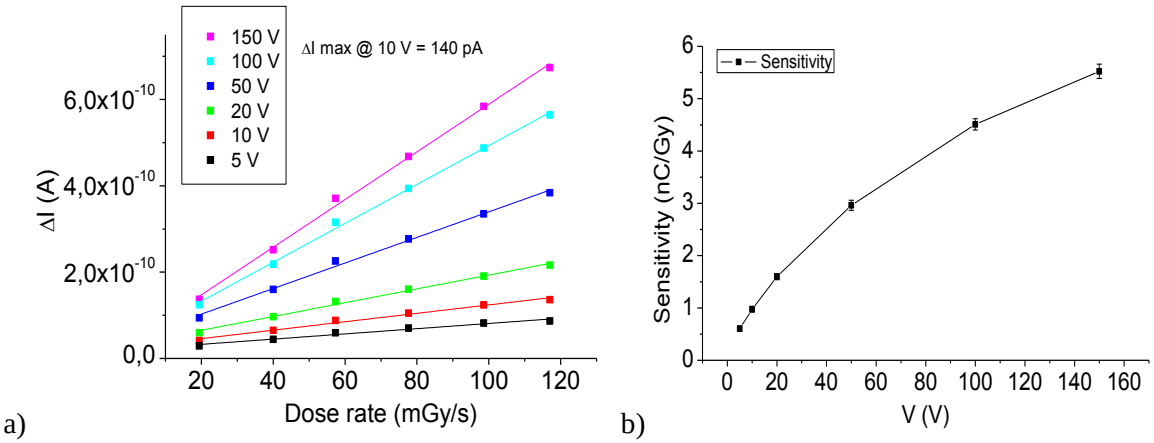

Figure 4.4: a) ΔI response for different bias voltages and b) sensitivity vs bias voltage (TIPSSC_01).

Bias voltage (V)	Sensitivity (nC/Gy)	Std error (nC/Gy)
5	0.60	0.05
10	**0.98**	**0.06**
20	1.60	0.06
50	2.96	0.10
100	4.51	0.11
150	5.52	0.14

Table 4.2: Sensitivity values (TIPSSC_01).

As can be observed, the ΔI and the sensitivity are comparable with those of the reference device (subsection 3.5). As previously mentioned, this sample is characterized by a low dark current and therefore presents high signal to noise ratios, as shown in Figure 4.5. However, considering all these aspects we can deduce that the TIPSSC_01 does not give a significant response under X-rays.

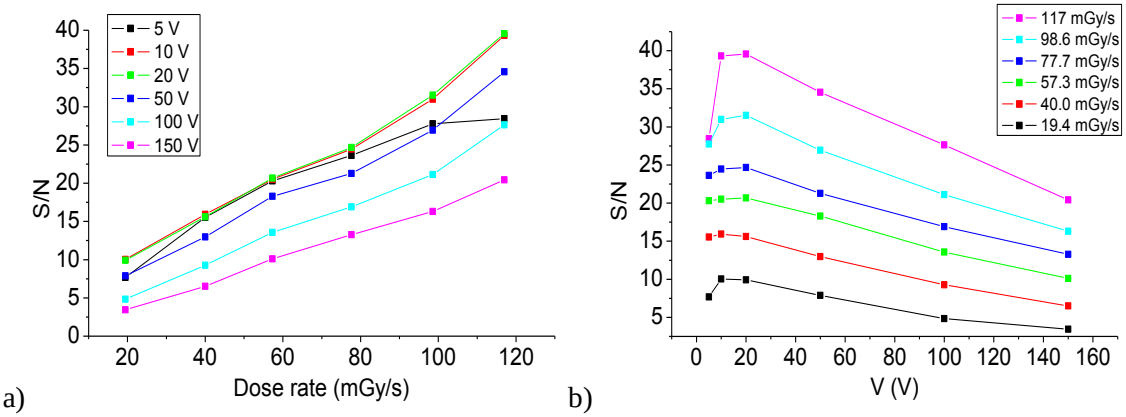

Figure 4.5: Signal-to-noise ratio plotted as a function of the a) dose rate and b) bias voltage (TIPSSC_01).

4.2 TIPSSC_02 – Planar Au electrodes (Solvent DCB 1%)

The second sample under test, the TIPSSC_02, presents the same features of the previous one, namely the electrodes geometry (planar with gold deposition) and the solvent employed for the crystal growth (DCB at the concentration of 1%). The TIPSSC_02 sample is shown in Figure 4.6.

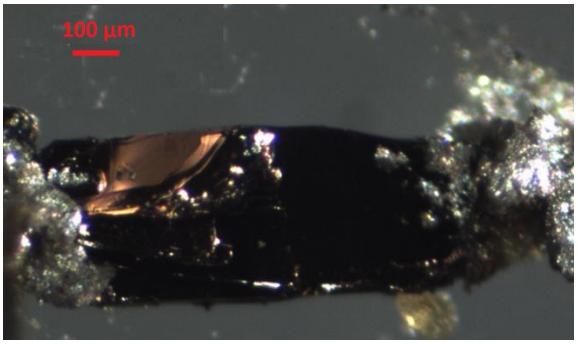

Figure 4.6: image of the TIPSSC_02 sample.

The dark current behavior is reported Figure 4.7a and the dynamical response of the sample is shown in Figure 4.7b for different bias voltages. As observed for the TIPSSC_01, we can appreciate an ohmic relation between the current and the applied voltage. On the other hand, with respect to the previous sample we can in this case observe a higher dark current and a noisier response. In particular, in Figure 4.7b it is possible to notice a current drift that becomes more evident at higher bias voltages.

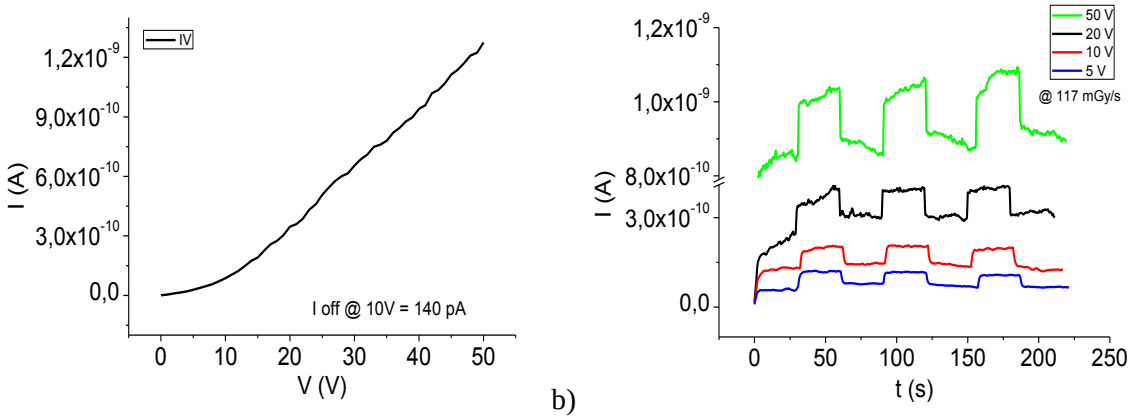

Figure 4.7: a) Dark current behavior between 0 V and 50 V; b) dynamical response at different bias voltages for the TIPSSC_02 sample.

Figure 4.8a shows the ΔI plotted as a function of the dose rate, for different applied voltages. In the graph of Figure 4.8b we report the sensitivity plotted as a function of the bias voltage. These results reveal that the TIPSSC_02 is characterized by a poor response in terms of both ΔI and sensitivity.

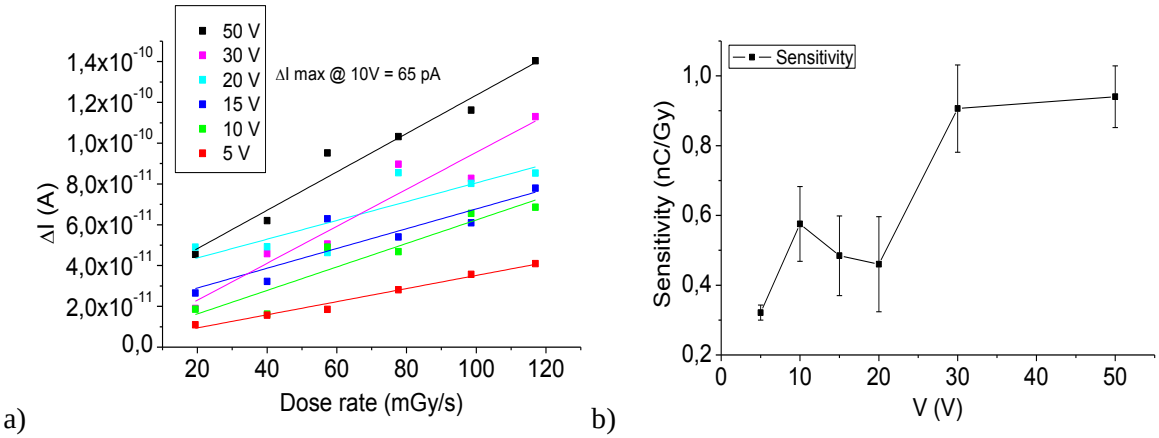

Figure 4.8: a) ΔI response for different bias voltages and b) sensitivity vs bias voltage (TIPSSC_02).

4.3 TIPSSC_07 – Planar Ag electrodes (Solvent Tetralin 5.75 mg/mL)

With respect to the previous two samples, the TIPSSC_07 has been grown using Tetralin as solvent (concentration 5.75 mg/mL) and has silver electrodes in planar geometry. Figure 4.9 shows an image of the TIPSSC_07 sample, where it is possible to identify the whole crystal and the channel region.

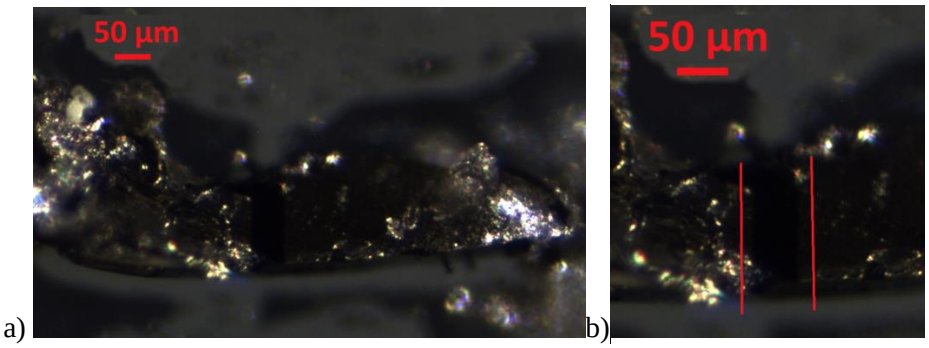

Figure 4.9: image of the TIPSSC_07 sample with silver electrodes: a) whole crystal and b) channel region.

The first measurement allows to obtain the dark current behavior, as reported in Figure 4.10. In this case, with respect to the previous samples (TIPSSC_01 and TIPSSC_02) we can observe a non-ohmic behavior.

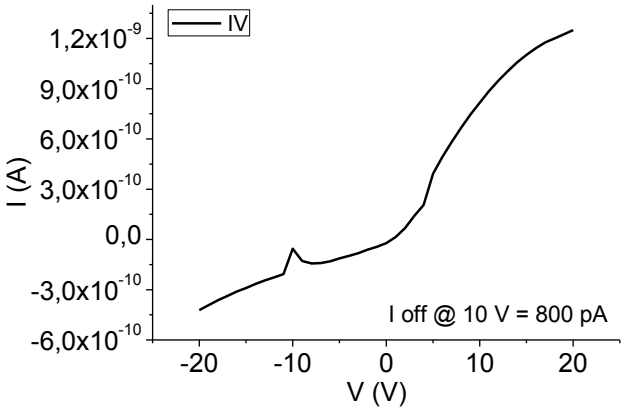

Figure 4.10: Dark current behavior between 0 V and 20V for the TIPSSC_07 sample.

The current versus time behavior for different bias voltages is reported in Figure 4.11. In order to study more in depth the device's response only one X-ray on/off cycle has been acquired (subsection 3.2). As shown, in this case the sample has been characterized for both positive and negative voltages.

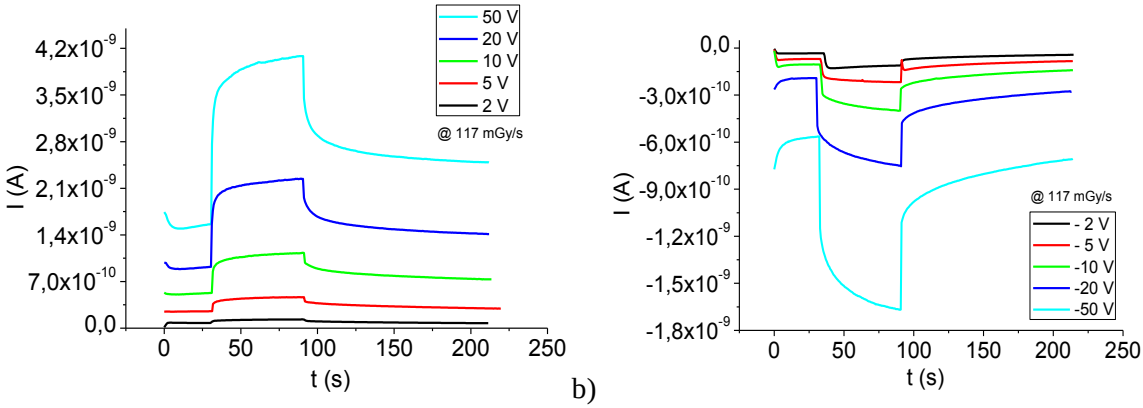

Figure 4.11: Dynamical behavior of the current at different bias voltages in the case of a) positive voltages and b) negative voltages (TIPSSC_07).

Subsequently, the same measurements have been repeated varying the dose rate in the case of both 10 V and -10 V of applied voltage (Figure 4.12). Through this measurement it is possible to obtain the ΔI response plotted as a function of the dose rate (Figure 4.13). Principal results are summarized in Table 4.3.

1st measurement		
Bias voltage (V)	ΔI @ 117 mGy/s (pA)	Sensitivity (nC/Gy)
10	240	3.63 ± 0.15
-10	420	1.29 ± 0.07

Table 4.3: Sensitivities and ΔI values (1st measurement, TIPPSC_07)

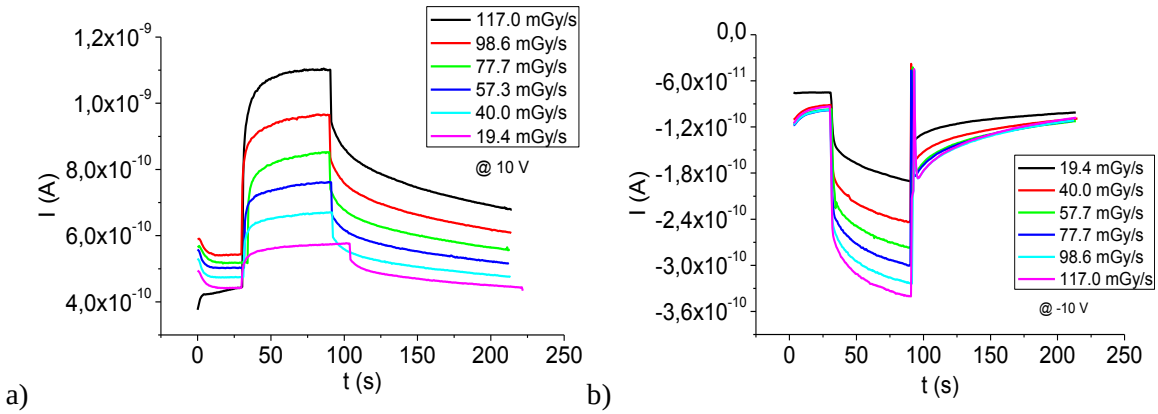

Figure 4.12: Dynamical behavior of the current at different at different dose rates in the case of a) 10 V and b) -10 V (TIPSSC_07).

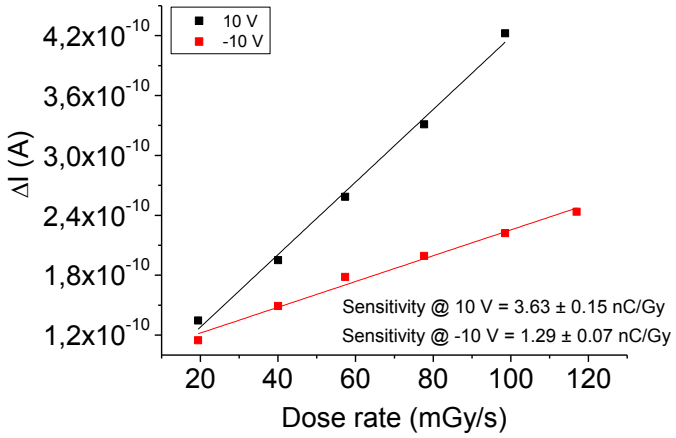

Figure 4.13: ΔI response at 10 V and -10 V of applied voltage (TIPSSC_07).

In order to evaluate the reliability of the results, the measurements performed varying the dose rate have been repeated and the results are shown in Figure 4.14 and Figure 4.15. By comparing the results of the first measurement (Table 4.3) with those of the second measurement (Table 4.4) we can ascertain a good agreement between data. Since the ΔI and the sensitivity are greater than those of the reference, we can deduce that the TIPSSC_07 gives a significant response under X-rays.

2nd measurement		
Bias voltage (V)	ΔI @ 117 mGy/s (pA)	Sensitivity (nC/Gy)
10	290	2.75 ± 0.14
-10	380	1.73 ± 0.11

Table 4.4: Sensitivities and ΔI values (2nd measurement, TIPPSC_07)

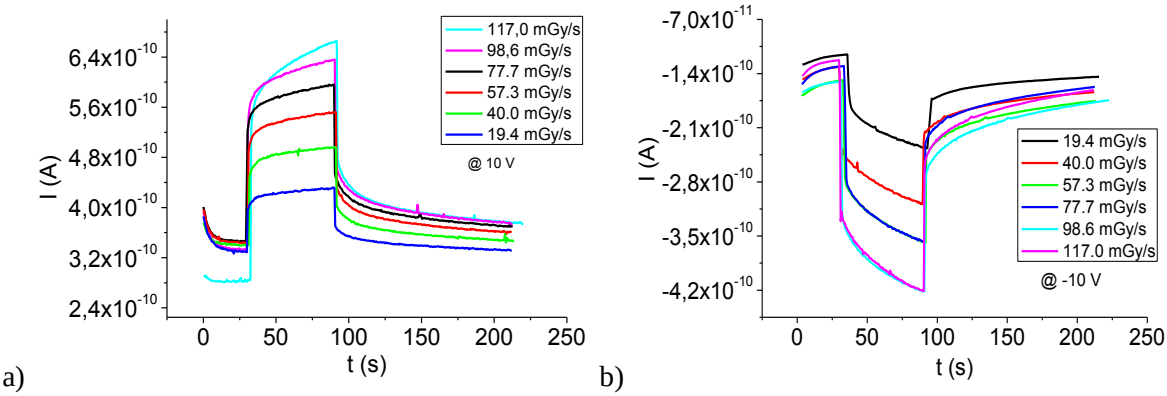

Figure 4.14: Dynamical behavior of the current at different at different dose rates in the case of a) 10 V and b) -10 V (TIPSSC_07, second measurement).

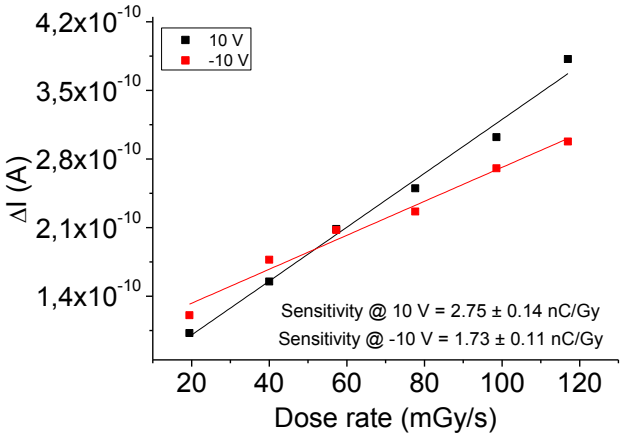

Figure 4.15: ΔI response at 10 V and -10 V of applied voltage (TIPSSC_07, second measurement).

In order to evaluate the presence of a trend in relation to the dose rate and the bias voltage, the dynamical curves of the first measurement have been normalized by the maximum and minimum values of the current. Results are reported in Figure 4.16.

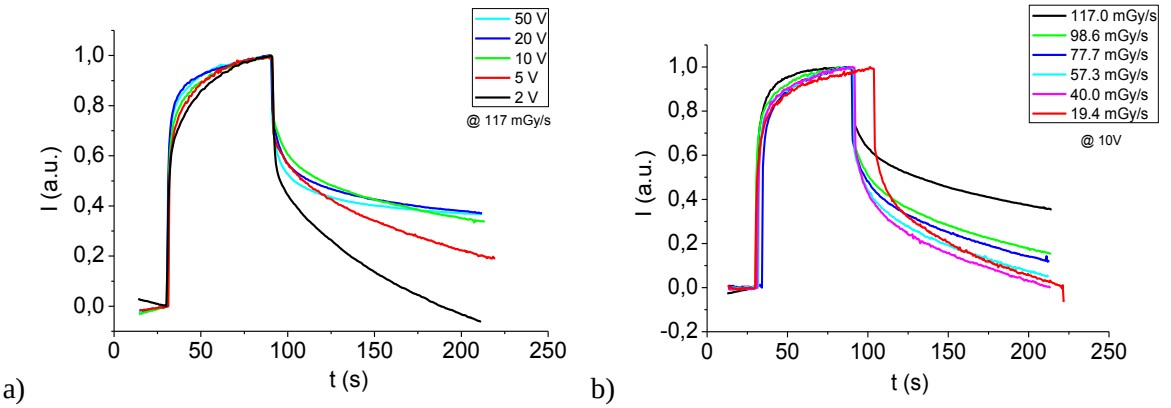

Figure 4.16: Dynamical behavior of the current normalized by the maximum and minimum values in the case of a) different bias voltages and b) different dose rates (TIPSSC_07).

As reported in subsection 1.5, the slow transient response shown above has been already observed in detectors based on thin film organic semiconductors exposed to X-rays [**16**]. The authors observed this phenomenon in poly(triarylamine) (PTAA) diodes where the electrodes' work function was higher than the HOMO level of the polymer and therefore with a low metal/semiconductor barrier. In contrast, samples with the electrodes' work function lower than the HOMO level of the polymer and therefore higher metal/semiconductor barrier, showed a fast time-independent response (Figure 4.17). The barrier height for hole injection (Φ_b) at the metal/semiconductor interface can be evaluated using the following equation:

$$\Phi_b = E_g - \Phi_m - \chi_s \qquad \textbf{Equation 4.1}$$

where E_g is the semiconductor energy gap, Φ_m is the metal work function and χ_s the electron affinity of the conjugated polymer.

a)

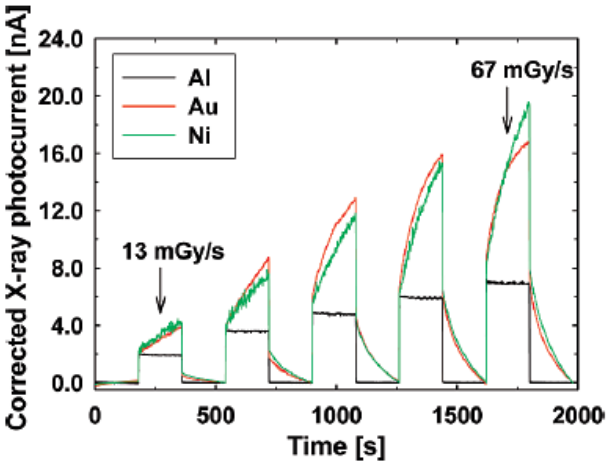

b)

interface	barrier height, ϕ_b (eV)
PTAA/Al	0.97
PTAA/Au	0.15
PTAA/Ni	0.1

Figure 4.17: a) Time-dependent X-ray response for the ITO/PTAA/metal sensors, with 20 µm thick PTAA layers, at an operational voltage of 200 V, upon exposure of 17.5 keV X-rays for 180 s durations through Al (black line), Au (red line), and Ni (green line) top contacts with X-ray dose rates increasing over time (13, 27, 40, 54, and 67 mGy/s). b) Barrier heights related to different metal/semiconductor interfaces. [16**]**

The slow transient response in the dynamical current behavior has been also observed in organic insulating materials, as for example polystyrene, exposed to X-rays (Figure 4.18a) [**21**] [**22**]. In this case this phenomenon is believed to be caused by the presence of electric traps or defect in the material: conduction electron may, it is assumed, become trapped in localized electron traps (Figure 4.18b) of unspecified nature, from which they will later be thermally released into conduction levels.

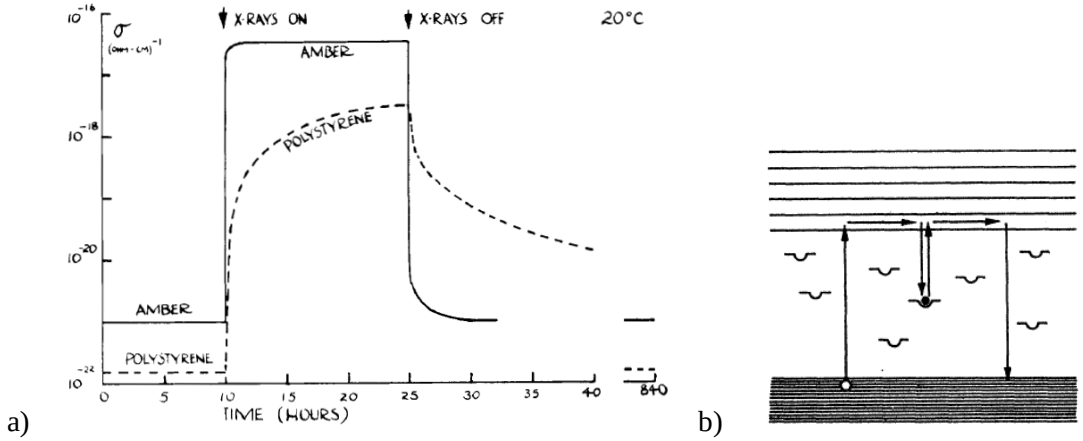

Figure 4.18:a) Conductivity induced by X-rays in polystyrene and amber, plotted against time. b) Energy level diagram for crystals or single groups of atoms in insulating materials. [21**]**

Let us now consider Figure 4.16a. Although there is not a clear trend, we can see that the rise appears faster in the case of higher bias voltages and slower for lower bias voltages. This feature is in contrast with the study reported in [**16**] (subsection 1.5). In order to investigate more deeply the detector's response, the raise steps of the dynamical curves reported in Figure 4.16a have been fitted with a double exponential as described in subsection 3.4. Both the rise and decay steps are characterized by a fast and a slow process and therefore we will refer to t_1 and t_2 as the slow and the fast time constant, respectively. The response times t_1 e t_2 related to the rise steps of the curves are plotted as a function of the bias voltage in Figure 4.19. Although there is not a clear trend, the time constants tend in general to decrease as the bias voltage increases, according to our previous considerations.

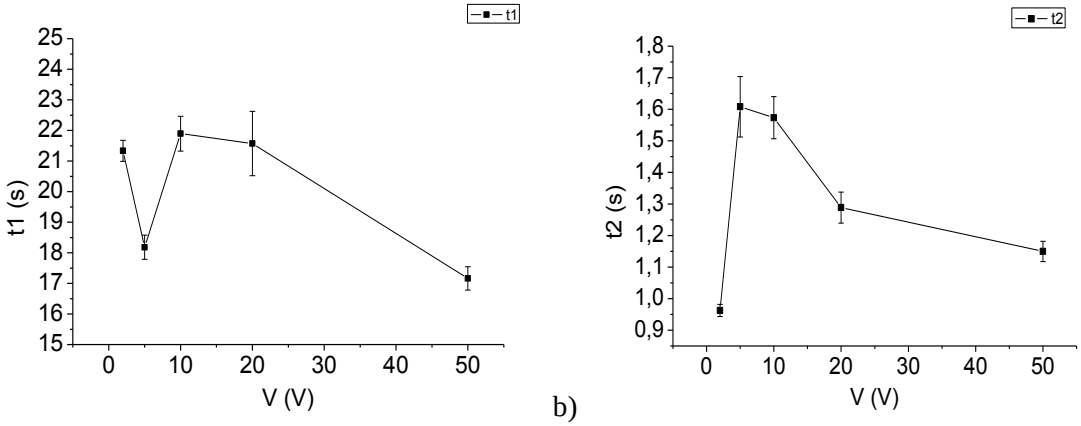

Figure 4.19: Rise times vs bias voltage in the case of a) t_1 and b) t_2 (TIPSSC_07).

Considering the decay steps of the dynamical curves reported in Figure 4.16a , we can ascertain that the process is slower in the case of 2 V and 5 V, while it is faster for higher bias voltages. The response times t_1 and t_2 related to the decay steps of the curves are plotted as a function of the bias voltage in Figure 4.20. Figure 4.20a shows clearly that the slow time constant t_1 decreases with the bias voltage.

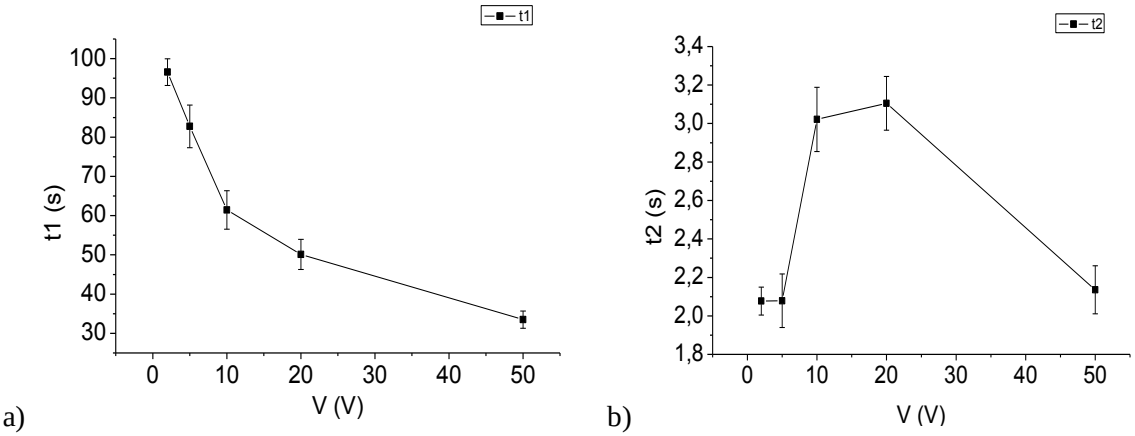

a) b)

Figure 4.20: Decay times vs bias voltage in the case of a) t_1 and b) t_2 (TIPSSC_07).

Moreover, analyzing the decay step of the normalized dynamical curves reported in Figure 4.16a we can see that in the case of 2 V and 5 V bias voltages the curves tend to zero, while for the other bias voltages the curves tend to a constant positive value. This feature can be better understood analyzing Figure 4.21, where the difference between the discharge current (the current value at the end of the acquisition) and the initial off current is plotted as a function of the bias voltage. As shown this difference tends to a constant value, according to our previous observation.

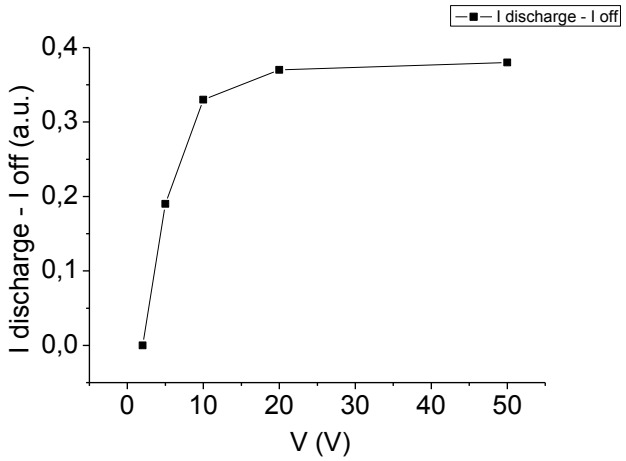

Figure 4.21: Difference between the discharge current (the current value at the end of the acquisition) and the initial off current plotted as a function of the bias voltage (TIPSSC_07).

Considering Figure 4.16b, we can observe the absence of a clear trend in relation to the dose rate, too. However, the rise step appears to be faster as the dose rate increases. This is confirmed by the results reported in Figure 4.22, where the rise time constants are plotted as a function of the dose rate and we can see that both t_1 and t_2 overall decrease as the dose rate increases.

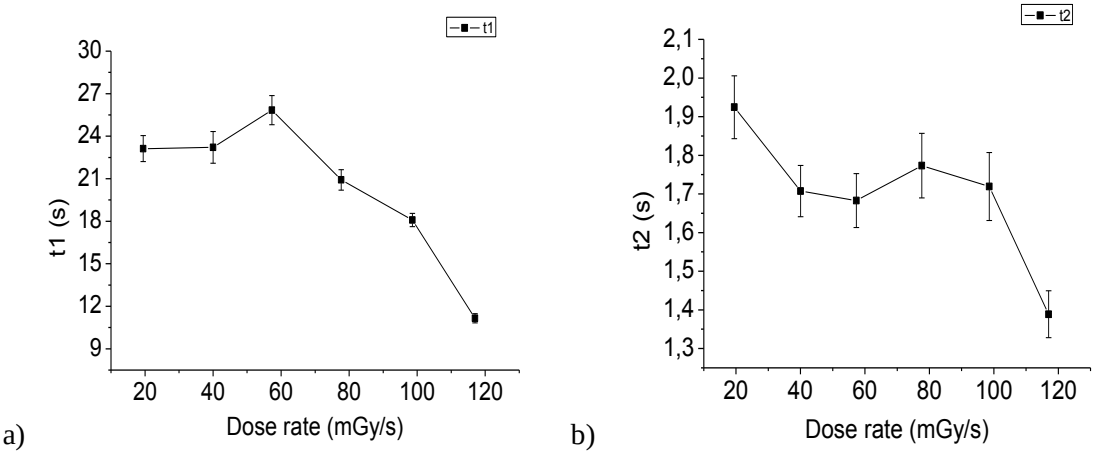

a) b)

Figure 4.22: Rise times vs dose rate in the case of a) t_1 and b) t_2 (TIPSSC_07).

As regards the decay step of the normalized dynamical curves reported in Figure 4.16b, we can observe that all the curves tend to zero. From Figure 4.23 we can ascertain that both t_1 and t_2 related to the decay step do not vary with the dose rate and the values are comparable taking into account the errors.

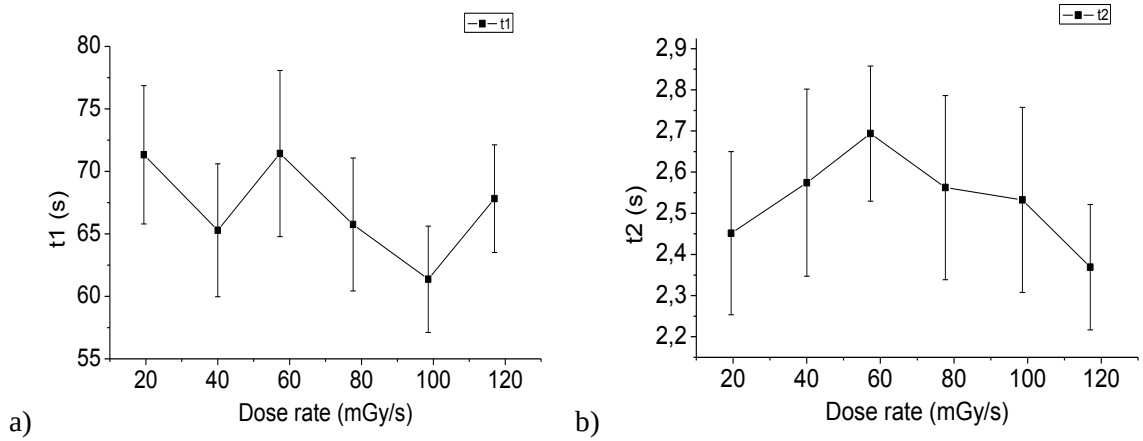

a) b)

Figure 4.23: Decay times vs dose rate in the case of a) t_1 and b) t_2 (TIPSSC_07).

Figure 4.24 shows the current dynamical response of the sample under LED (λ = 375 nm) illumination (black line). In order to perform a comparison we also report in the same graph the current dynamical response of the sample under X-rays (red line) at the dose rate of 98.6 mGy/s.

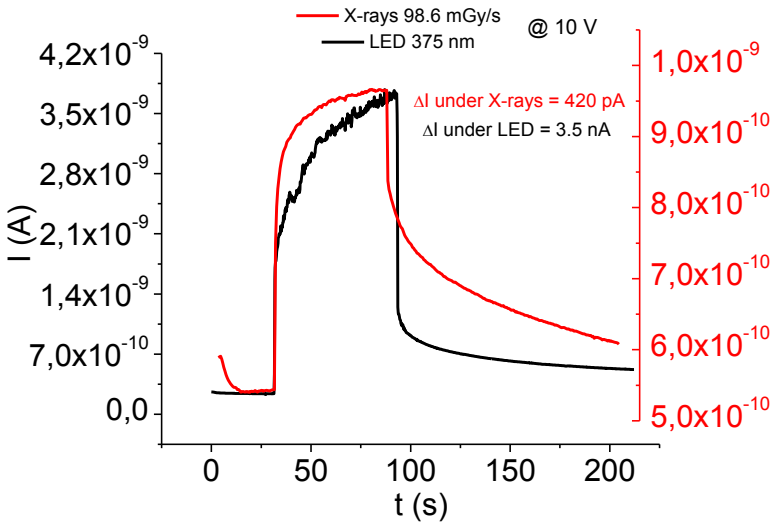

Figure 4.24: Current dynamical response under LED (λ = 375 nm) illumination (black line) and under X-rays at the dose rate of 98.6 mGy/s (red line) (TIPSC_07).

As can be noticed, a slow transient response has been obtained also under LED illumination. This phenomena has been already observed in TIPS-pentacene single crystals under LED (λ = 660 nm) illumination (Figure 4.25) [**18**]. In the cited article, the authors state that the origin of persistent photoconductivity involves the presence of traps, which may either pre-exist, or which may be created or modified by the optical illumination.

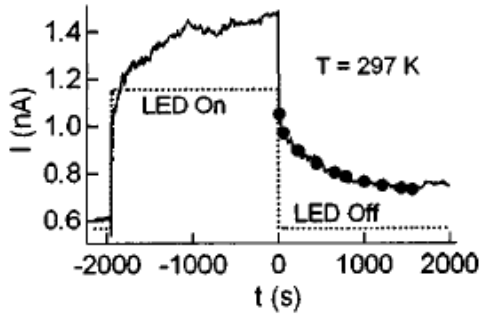

Figure 4.25: Persistent photocurrent in the TIPS-pentacene for the 660 nm illumination vs time. [18**]**

A similar transient phenomena has been also observed in modulated photocurrent measurement of organic photocells based on Titanyl phthalocyanine (TiOPc), under LASER irradiation (λ = 633 nm) [**23**]. The authors describe the observed slow time constants in terms of a modified space-charge distribution at the Schottky barrier. The optical injection of excess photocarriers causes the build-up of space charge limited currents, which influence the effective Schottky barrier height because of band bending at the metal/polymer interface.

The response time analysis has been also performed for the dynamical curve obtained under LED illumination and the time constants are reported in Table 4.5. In order to compare the responses, in the same table we report the response time constants related to the X-rays irradiation at 98.6 mGy/s

dose rate. As can be observed, the response time constants obtained under X-rays are comparable with those obtained under LED illumination.

	X-rays (98.6 mGy/s)		LED (λ = 375 nm)	
	t_1 (s)	t_2 (s)	t_1 (s)	t_2 (s)
Charge	18.1 ± 0.5	1.7 ± 0.1	22.9 ± 0.6	0.5 ± 0.1
Discharge	61.4 ± 4.3	2.5 ± 0.2	50.5 ± 6.9	1.7 ± 0.2

Table 4.5: time constants related to the dynamical curves reported in Figure 4.24.

4.4 TIPSSC_09 – Planar Au electrodes (Solvent Tetralin 4.9 mg/mL)

Let us now consider the fourth TIPS-based sample, the TIPSSC_09. Although the solvent concentration is slightly lower, the solvent type employed for the crystal growth is the same as that of the TIPSSC_07 (Tetralin). However, the deposition process has been performed using gold as deposition metal and therefore the TIPSSC_09, as the first two samples (TIPSSC_01 and TIPSSC02), has planar Au electrodes. Figure 4.26a and Figure 4.26b show a picture of the sample under test (whole crystal) and of the channel region, respectively.

a) 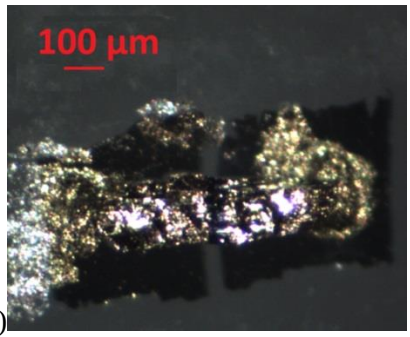

b) 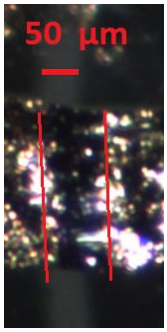

Figure 4.26: image of the TIPSSC_09 sample with gold electrodes: a) whole crystal and b) channel region located between the red lines.

As can be noticed from Figure 4.27, the dark current of the TIPSSC_09 shows an ohmic behavior: among the TIPS-based samples, this feature has been observed in samples having gold electrodes.

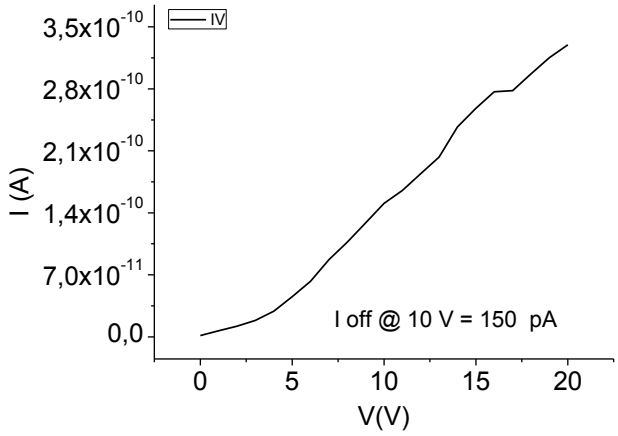

Figure 4.27: Dark current behavior between 0 V and 20 V for the TIPSSC_09 sample.

Figure 4.28a and Figure 4.28b show the dynamical behavior of the current for different applied voltages and for different dose rates, respectively (only one X-ray on/off cycle is reported). As can be observed, the response is noisier and faster with respect to the TIPSSC_07.

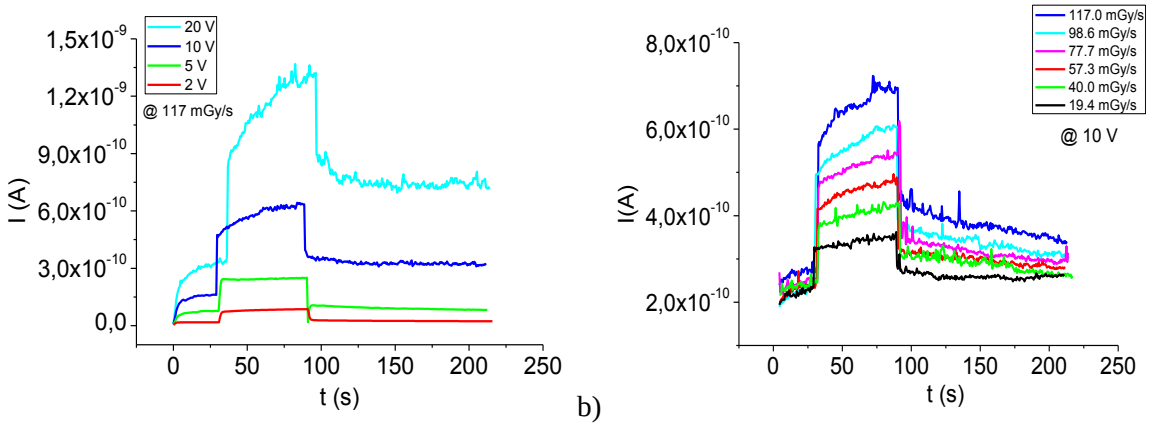

Figure 4.28: Dynamical behavior of the current a) at different bias voltages and b) at different dose rates.

Despite the noisy response, the ΔI and the sensitivity are greater than those of the reference device: the ΔI at the maximum dose rate is 420 pA and the sensitivity is (2.99 ± 0.13) nC/Gy (Figure 4.29). Moreover, high signal-to-noise ratios have been obtained, as shown in Figure 4.29b. Considering all the previous figures of merit, we can say that the TIPSSC_09 provides a significant response under X-rays.

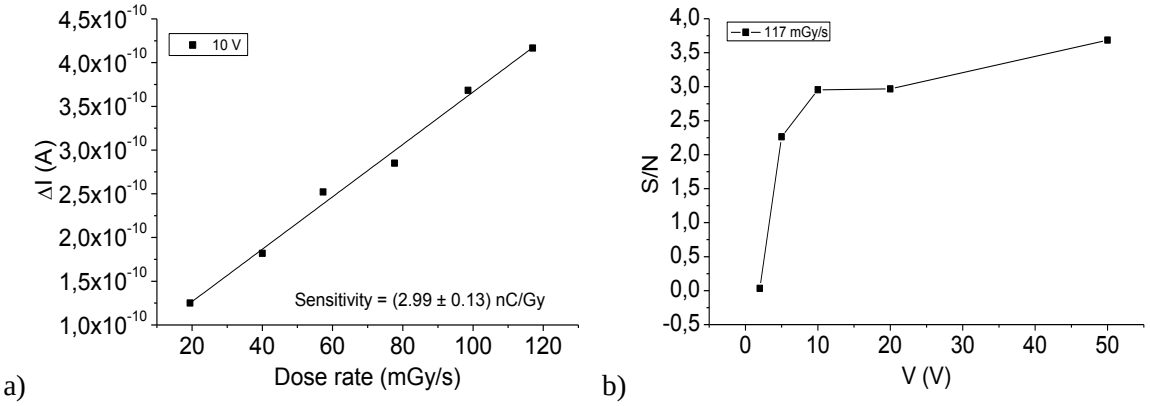

Figure 4.29: a) ΔI response at the bias voltage of 10 V and b) signal-to-noise ratio plotted as a function of the bias voltage (TIPSC_09).

4.5 Summary

The first two samples (TIPSSC_01 and TIPSC_02), which have been grown employing DCB solvent and have Au electrodes, did not show a significant response under X-rays. On the other hand, the TIPSSC_07 sample has been grown using Tetralin solvent and has Ag electrodes. As discussed in subsection 4.3, the TIPSSC_07 showed a significant response under X-rays, with sensitivities up to (3.63 ± 0.15) nC/Gy at 10 V bias voltage. The last sample, TIPSSC_09, has been grown with Tetralin solvent and has Au electrodes: it exhibited a significant response under X-rays achieving sensitivities up to (2.99 ± 0.13) nC/Gy at 10 V bias voltage. Considering these results, we correlated the differences in the X-ray detection performances to the solvent employed. Moreover, this hypothesis is supported by the characterization results (not reported here) of another sample, the TIPSSC_04. The latter has been grown mainly with DCB (70% DCB and 30% Benzonitrile 5mg/mL) and has Au electrodes: as the other samples grown with DCB, it has not shown a significant response under X-rays.

As regard the in-depth-analysis of the TIPSSC_07 response under X-rays, we observed a slow transient in the current dynamical curves both varying the bias voltage and the dose rate. We performed exponential fits of the rise and decay steps of the dynamical curves and we analyzed the variation of the slow and fast time constant (t_1 and t_2, respectively) with both the bias voltage and the dose rate. The results showed that both the time constants related to the rise and decay steps of the curves tend to decrease as the bias voltage increases. Moreover, the time constants related to the rise step of the curves tend to decrease as the dose rate increases, while those related to the decay step do not vary with the dose rate. Subsequently, a measurement under LED (λ = 375 nm) illumination has been performed and the dynamical curve showed, as those under the X-rays, a slow charge and discharge response. We compared this measurement with that obtained under X-rays at 98.6 mGy/s and we observed that the time constants of both the responses were comparable, possibly indicating that the two mechanisms of photogeneration and charge collection have the same nature.

In order to have an overview on the principal results related to all the samples treated in this chapter, we report a summary in Table 4.6. Since in the case of the TIPSSC_07 we performed two measurement sessions, we specify that the values reported in the table are the highest obtained.

Sample	Electrodes geometry	Solvent	I_{off} @ 10V (pA)	Sensitivity @ 10 V (nC/Gy)	S/N max @10V	ΔI @ 10 V @ 117mGy/s (pA)	Response
TIPSSC_01	planar Au	DCB 1%	6	0.98 ± 0.06	39.32 @ 117 mGy/s	135	!
TIPSSC_02	planar Au	DCB 1%	140	0.58 ± 0.11	0.53 @ 117 mGy/s	62	!
TIPSSC_07	planar Ag	Tet. 4.9 mg/mL	800	3.63 ± 0.15	1.53 @117 mGy/s	670	√
TIPSSC_09	planar Au	Tet. 5.7 mg/mL	150	2.99 ± 0.13	1.55 @ 98.6 mGy/s	420	√

Table 4.6: Summarized results (TIPS-based samples).

5 Characterization of Rubrene-based detectors

Rubrene (5,6,11,12-tetraphenyltetracene) belongs to the group of polycyclic aromatic hydrocarbons and consist of a tetracene backbone (it is built with four benzene rings placed side by side each other), with a phenyl ring bonded on each side of the two centralbenzene rings, as shown in the molecular structure reported in Figure 5.1. This molecule is one of the most investigated and promising organic semiconductor, due to its low density of charge traps and high charge carrier mobility (in the range of 20-40 cm^2/Vs [**24**]). At the same time it is still presenting some open problems which limits its performances, as its chemical instability in presence of oxygen and the difficulty to obtain a good crystalline quality samples [**24**] [**25**].

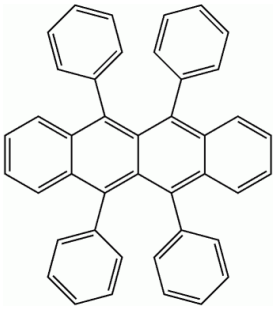

Figure 5.1: Rubrene molecular structure.

In this chapter we will show the characterization results of five Rubrene-based detectors (Rux_03, Rux_04, Rux_05, Rux_08, Rux) which have planar Au electrodes. Crystals have been grown by Physical Vapor Transport (PVT, subsection 1.5).

5.1 Rux_03 – Rux_04 – Rux_05

In this subsection we report the characterization results of three Rubrene-based samples (Rux_03, Rux_04, Rux_05), which are shown in Figure 5.2 and have gold electrodes in planar configuration.

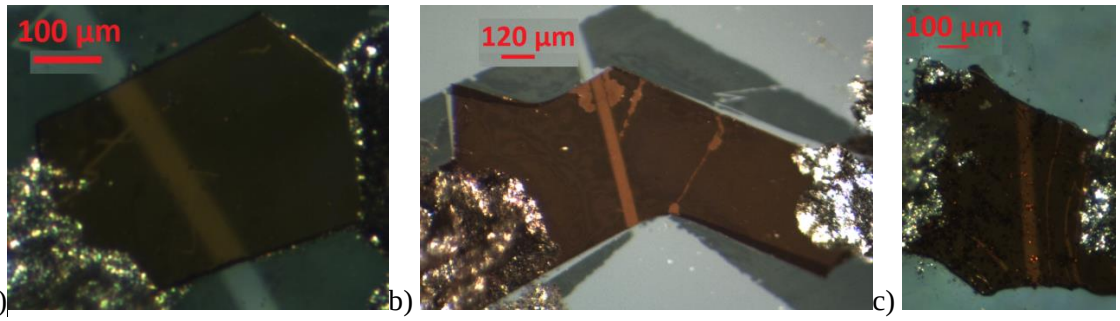

a) b) c)

Figure 5.2: image of the a) Rux_03, b) Rux_04 and c) Rux_05.

The principal characterization results are reported in Table 5.1, where we can notice that all the samples have in common an high dark current. In general, these samples present a poor response with ΔI values and sensitivities comparable with those of the reference device.

Sample	Electrodes geometry	I_{off} @ 10V (pA)	Sensitivity @ 10 V (nC/Gy)	S/N max @10V	ΔI @ 10 V @ 117mGy/s (pA)	Response
Rux_04	planar Au	**1800**	0.67 ± 0.32	0.02 @ 77.7 mGy/s	86	!
Rux_03		**600**	1.05 ± 0.09	0.15 @ 117 mGy/s	160	!
Rux_05		**500**	0.85 ± 0.24	0.35 @ 117 mGy/s	170	!

Table 5.1: principal characterization results of the Rux_03, Rux_04 and Rux_05 samples.

An interesting feature of these samples can be appreciated by analyzing the current dynamical responses, reported in Figure 5.3 and Figure 5.4.

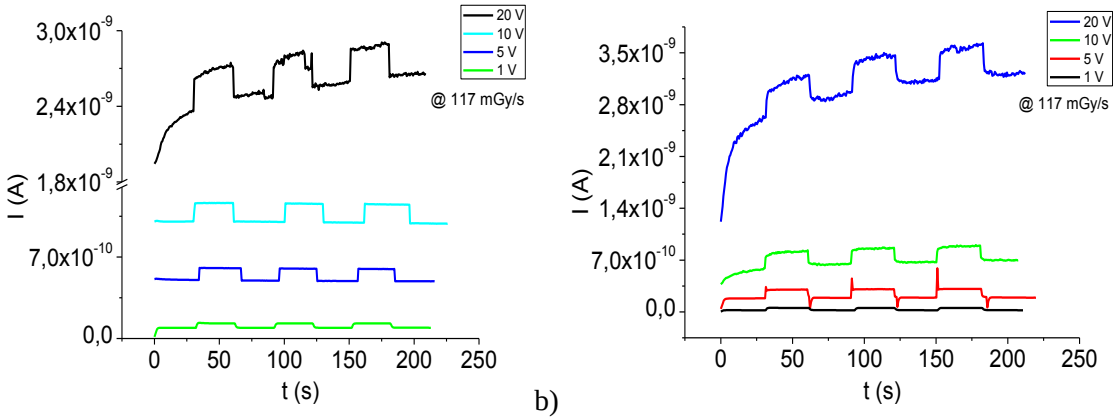

a) b)

Figure 5.3: dynamical response at different bias voltages for the a) Rux_03 and b) Rux_05 samples.

In fact, regarding the Rux_03 and Rux_05 (Figure 5.3) we can notice a drift of the dark current more evident at higher applied voltages (20 V). On the other hand, concerning the Rux_04 sample (Figure 5.4), this behavior is more evident at lower bias voltages (1 V and 5 V).

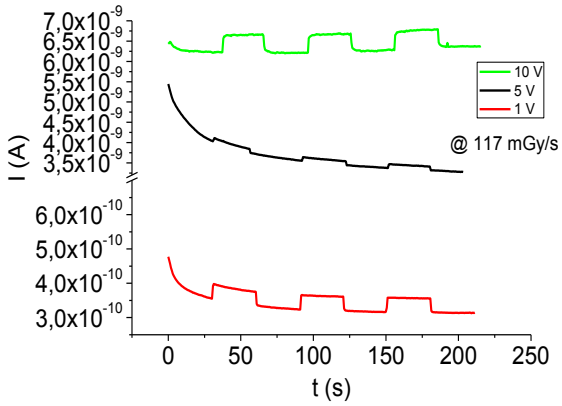

Figure 5.4: dynamical response at different bias voltages for the Rux_04 sample.

5.2 Rux_08

In this subsection we report the characterization results of the Rux_08 sample, shown in Figure 5.5.

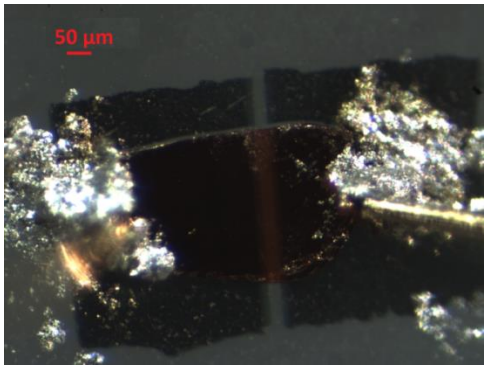

Figure 5.5: image of the Rux_08 sample.

The dark current behavior between 0 V and 20 V is reported Figure 5.6a, where we can observe a dark current of 80 pA at 10 V of applied voltage, much lower than in the previous three samples. The dynamical behavior of the current is reported in Figure 5.6b and shows a fast response for all the applied voltages involved.

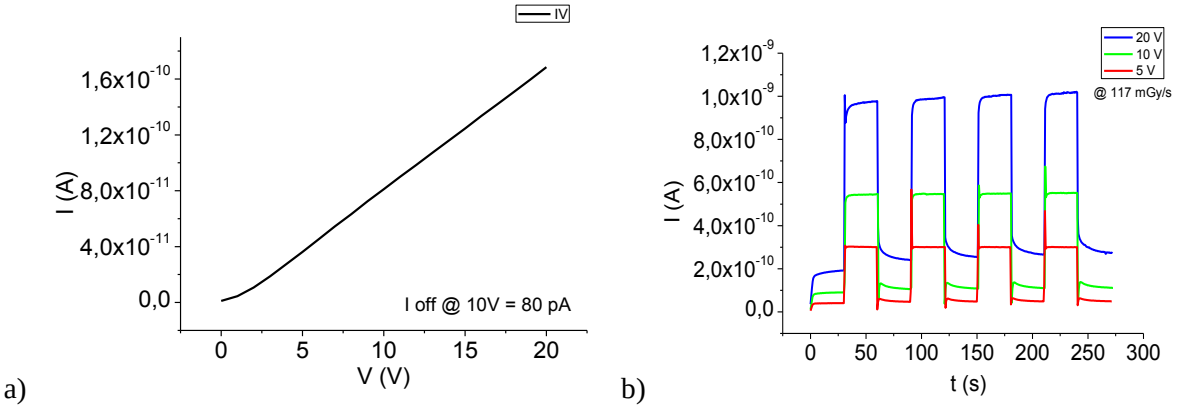

Figure 5.6: a) Dark current behavior between 0 V and 20 V and b) dynamical response at different bias voltages for the Rux_08 sample.

The ΔI response is shown in Figure 5.7a for different bias voltages, where we can appreciate that the maximum ΔI obtained at 10 V is 460 pA. Concerning the sensitivity, the values are plotted versus the bias voltage in Figure 5.7b and reported numerically in Table 5.2.

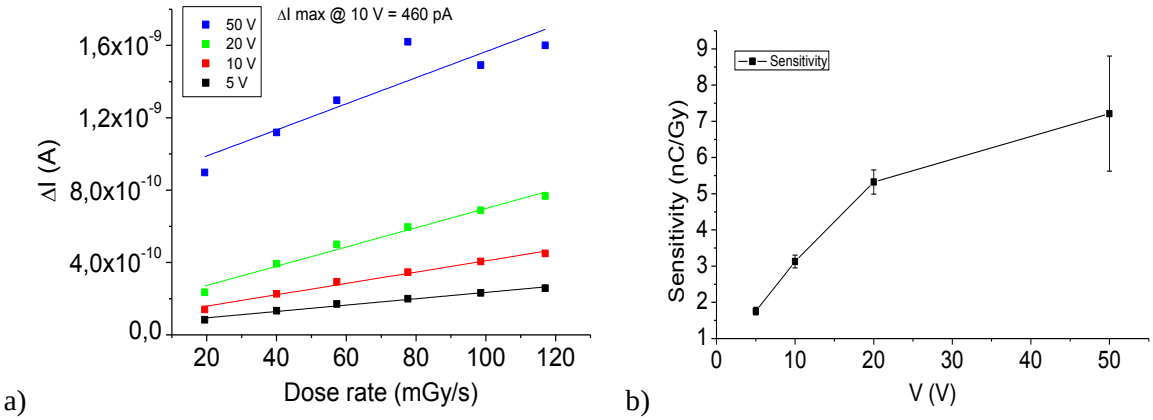

Figure 5.7: a) ΔI response for different bias voltages and b) sensitivity vs bias voltage (Rux_08).

Bias voltage (V)	Sensitivity (nC/Gy)	Std error (nC/Gy)
5	1.76	0.11
10	**3.13**	**0.18**
20	5.32	0.33
50	7.21	1.59

Table 5.2: Sensitivity values (Rux_08).

In this case the ΔI and the sensitivity are greater than those of the reference device. In addition, due to the low dark current we obtained high signal-to-noise ratios, as can be seen from Figure 5.8. As an example, considering the reference voltage of 10 V, we calculated a signal-to-noise ratio of 4.3 at the maximum dose rate. Moreover, we can observe that the signal-to-noise ratio increases as the

dose rate increases and as the applied voltage decreases. Considering all the previous considerations, we can say that the Rux_08 gives a significant response under X-rays.

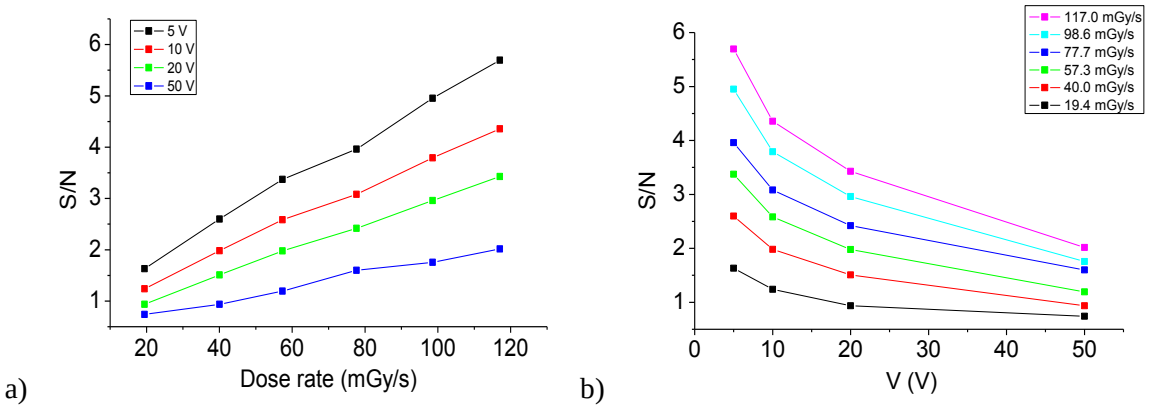

Figure 5.8: Signal-to-noise ratio plotted as a function of the a) dose rate and b) bias voltage (Rux_08).

5.3 Rux

An image of the Rux sample, taken with the optical microscope, is reported in Figure 5.9.

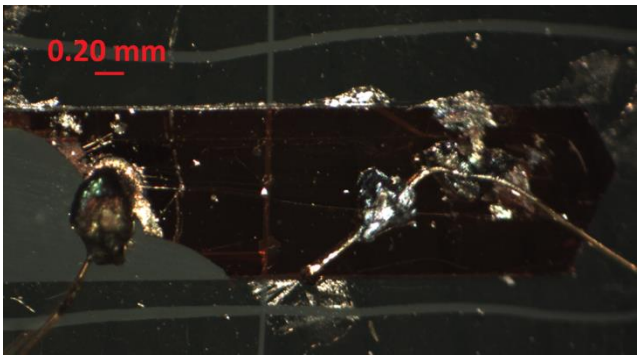

Figure 5.9: image of the Rux sample.

The dark current behavior (Figure 5.10a) shows, similarly to the previous sample, a dark current of 130 pA at 10 V of applied voltage, much lower than those of the first three samples (Rux_03, Rux_04, Rux_05). The dynamical behavior of the current (Figure 5.10b) reveals, as the TIPSSC_07, a slow charge and discharge response more evident as the applied voltage increases.

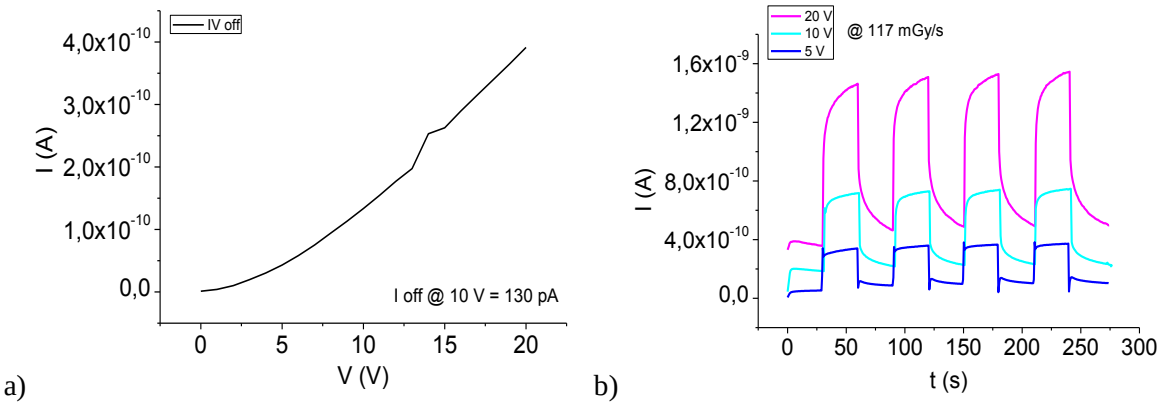

Figure 5.10: a) Dark current behavior between 0 V and 20 V and b) dynamical response at different bias voltages for the Rux sample.

An example of a sweep voltage measurement, in the case of 117 mGy/s dose rate, is reported in Figure 5.11. In this case for the subsequent data analysis we consider two values of the current at the voltage step of 50 V: correspondingly to the X-ray beam switched on we consider the current values at the beginning of the transient ($I_{on\ min}$) and at the end of the transient ($I_{on\ max}$), in order to evaluate the difference in sensitivity between the two cases.

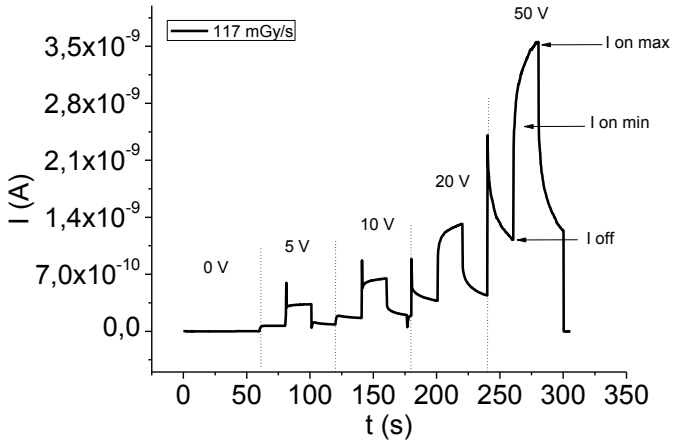

Figure 5.11: Sweep Voltage measurement. Current versus time behavior increasing periodically the bias voltage (0 V, 5 V, 10 V, 20 V, 50 V). Correspondingly to each bias voltage step, the X-ray beam is switched on and kept on for a given time. Example considering 117 mGy/s dose rate (30 mA X-ray tube operation current).

Figure 5.12a and Figure 5.12b show the ΔI versus the dose rate and the sensitivity values plotted as a function of the bias voltage, respectively. Sensitivities are reported numerically in Table 5.3.

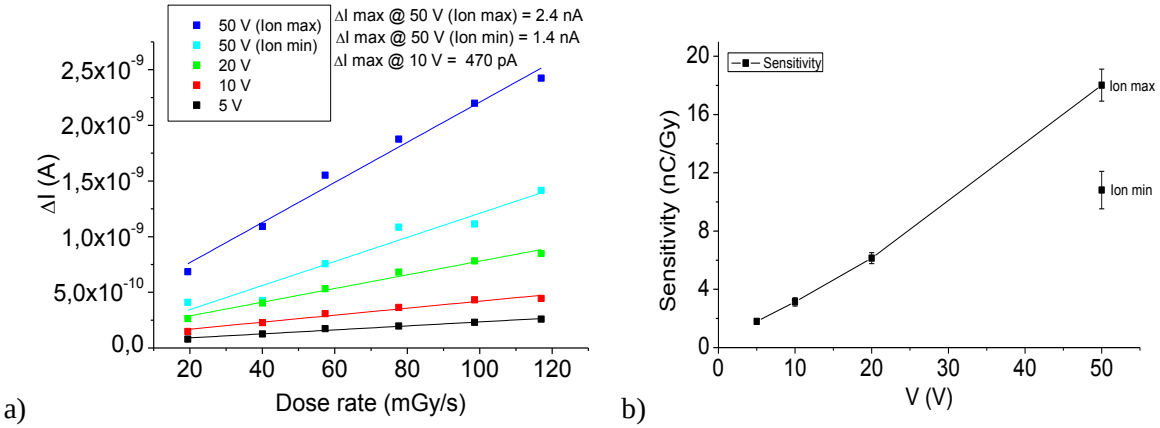

Figure 5.12: a) ΔI response for different bias voltages and b) sensitivity vs bias voltage (Rux).

Bias voltage (V)	Sensitivity (nC/Gy)	Std error (nC/Gy)
5	1.79	0.12
10	**3.14**	**0.28**
20	6.14	0.37
50 (Ion max)	18.02	1.10
50 (Ion min)	10.82	1.29

Table 5.3: Sensitivity values (Rux).

As illustrated, the ΔI and the sensitivity are significantly greater than those of the reference device. Moreover, due to the low dark current we obtained high signal-to-noise ratios, as can be seen from Figure 5.13.

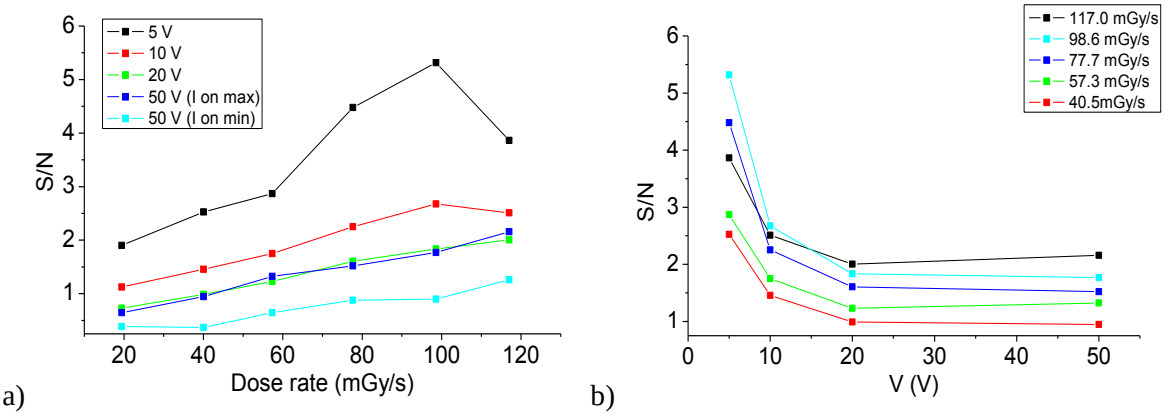

Figure 5.13: Signal-to-noise ratio plotted as a function of a) the dose rate and b) the bias voltage (Rux).

In order to study the response time of the current device, measurements with only one X-ray beam on/off cycle have been performed, as illustrated for the TIPSSC_07 sample. The current versus time behavior obtained varying the applied voltage and the dose rate are reported in Figure 5.14 and Figure 5.15, respectively.

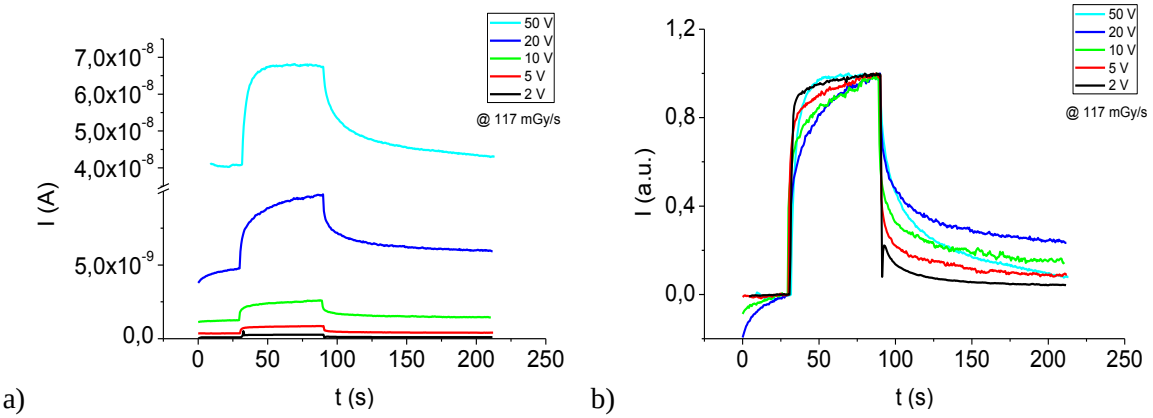

Figure 5.14: Dynamical behavior of the current at different bias voltages. a) Not normalized b) normalized by the I_{on} and I_{off} values of the current (Rux).

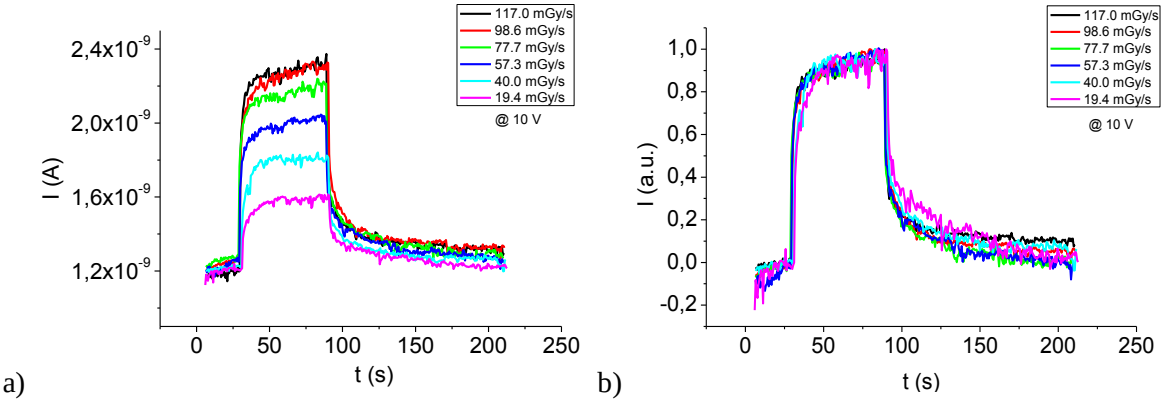

Figure 5.15: Dynamical behavior of the current at different dose rates. a) Not normalized b) normalized by the I_{on} and I_{off} values of the current (Rux).

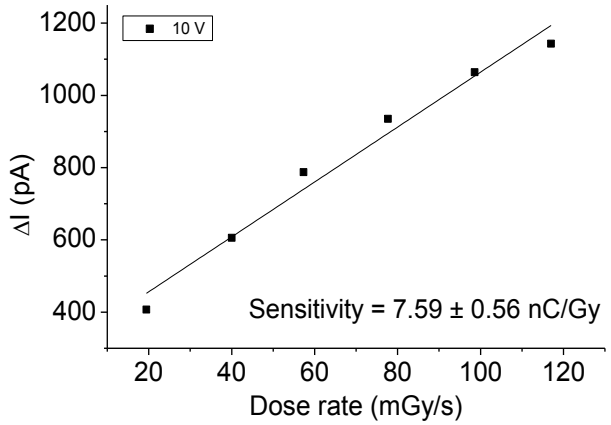

Figure 5.16: ΔI response calculated from data of Figure 5.15 (Rux).

The ΔI plotted as a function of the dose rate, calculated from the data of Figure 5.15, is reported in Figure 5.16. As shown, a sensitivity of (7.59 ± 0.56) nC/Gy has been calculated considering 10 V of applied voltage.

In order to investigate more deeply the detector's response, the rese steps of the dynamical curves reported in Figure 5.14a have been fitted with a double exponential as illustrated in subsection 3.4. The slow and fast time constants (t_1 and t_2 respectively) related to the rise and decay steps of the curves are plotted as a function of the bias voltage in Figure 5.17 and Figure 5.18. Analyzing these results, it is not possible to identify a clear trend in both cases.

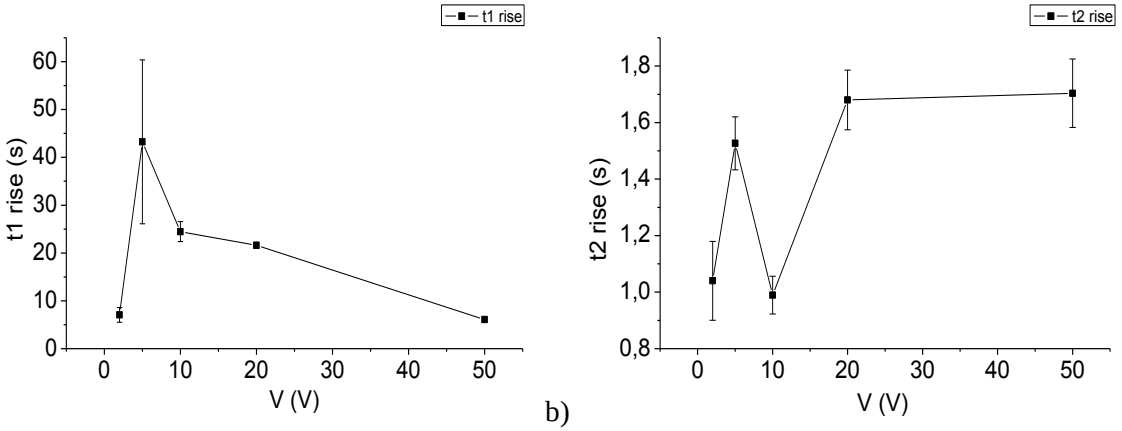

a) b)

Figure 5.17: Rise times vs bias voltage in the case of a) t_1 and b) t_2 (Rux).

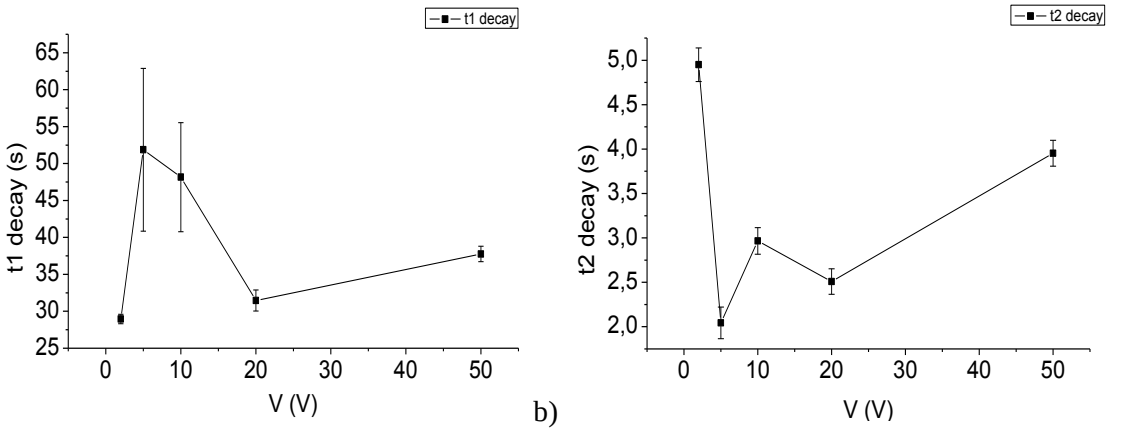

a) b)

Figure 5.18: Decay times vs bias voltage in the case of a) t_1 and b) t_2 (Rux).

By considering Figure 5.15, the response times t_1 e t_2 related to the rise and decay steps of the curves are plotted as a function of the dose rate in Figure 5.19 and Figure 5.20, respectively. As in the previous results, also in this case it is not possible to identify a clear trend.

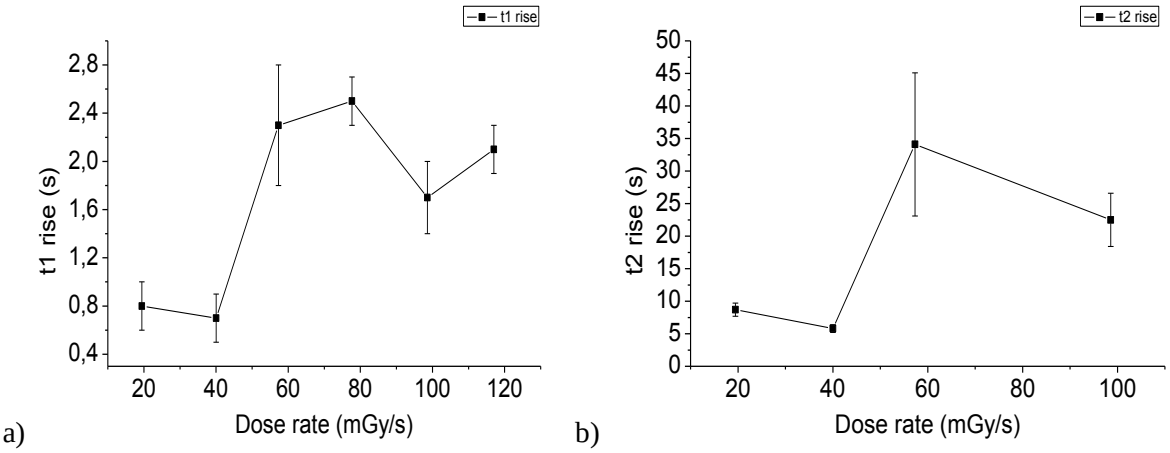

a) b)

Figure 5.19: Rise times vs dose rate in the case of a) t_1 and b) t_2 (Rux).

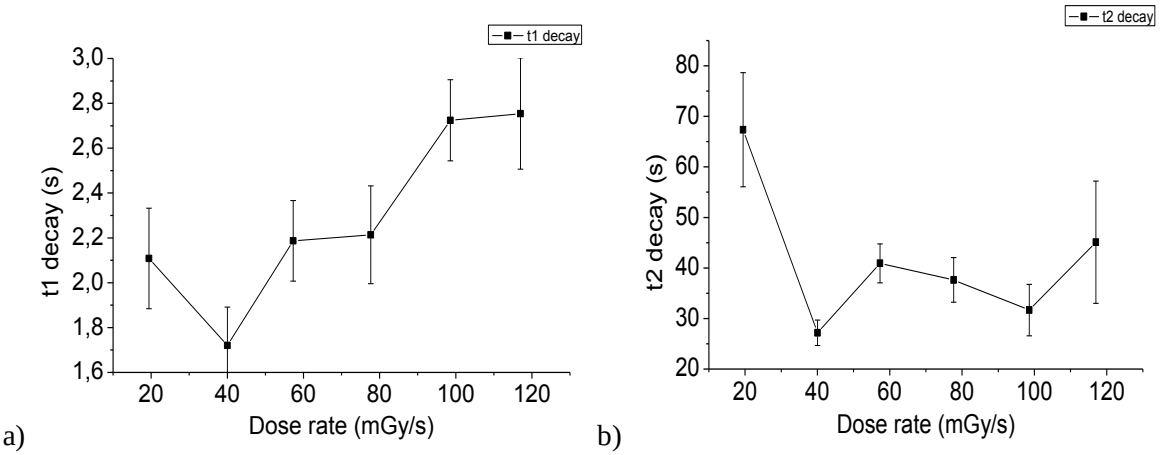

a) b)

Figure 5.20: Decay times vs dose rate in the case of a) t_1 and b) t_2 (Rux).

Figure 5.21 shows the current dynamical response of the sample under LED (λ = 375 nm) illumination (black line). In order to perform a comparison we also report in the same graph the current dynamical response of the sample under X-rays (red line) at the dose rate of 98.6 mGy/s.

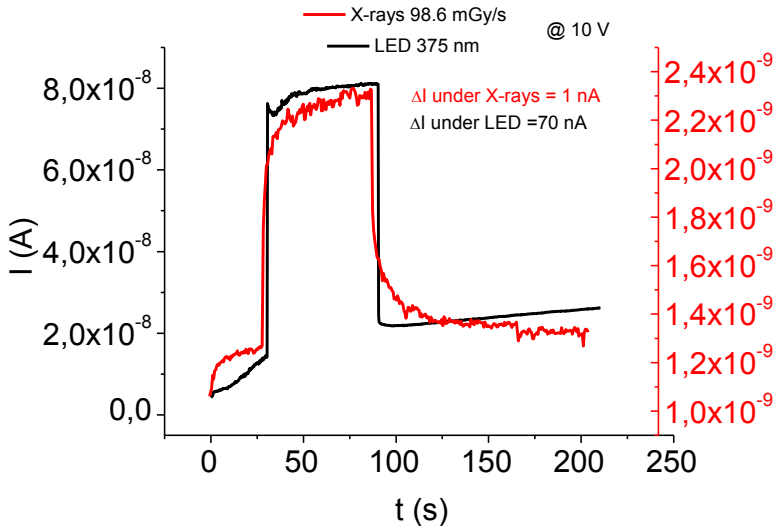

Figure 5.21: Current dynamical response under LED (λ = 375 nm) illumination (black line) and under X-rays at the dose rate of 98.6 mGy/s (red line) (Rux).

As can be noted, unlike the TIPSSC_07 the Rux response under LED illumination is faster without a significant transient. A similar study that is worth mentioning is reported in [**17**], where the photocurrent response of a field effect transistor based on Rubrene single crystals has been investigated, under LASER irradiation (λ = 405 nm). The authors observed a small persistent photoconductivity under continuous illumination, effect explained by delayed recombination aided by spatial separation of the photocarriers (Figure 5.22a). Photocurrent transients measured by applying short pulses on the other hand show a complete recovery in the microsecond regime implying immediate recombination (Figure 5.22b).

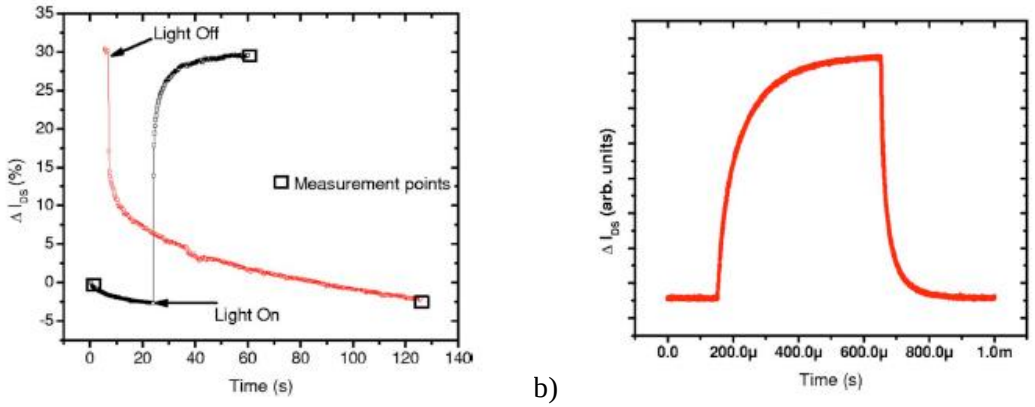

a) b)

Figure 5.22: a) Rise (black) and decay (red) of I_{DS} measured under continuous illumination. b) Photocurrent transients in the microsecond time range measured by applying short light pulses in the drain area showing immediate recombination of the charge carriers.

In contrast to the persistent photoconductivity clearly seen under continuous illumination, in Figure 5.22b the photocurrent decays in about 100 μs to its previous value. The authors believe that this difference arises from various spatial distributions of the electrons in the crystal. The short pulse

does not allow enough time for the photogenerated electrons to move into the bulk, thus resulting in immediate recombination with the holes when the laser pulse is stopped.

5.4 Summary

The first three samples (Rux_03, Rux_04, Rux_05) did not give a significant response under X-rays, showing high dark currents and therefore low signal-to-noise ratios. The Rux and Rux_08 samples, instead, have shown a lower dark current and their response in terms of ΔI and sensitivity was greater than that of the reference device. In particularly, the Rux sample has shown sensitivities up to (7.59 ± 0.56) nC/Gy at 10 V of applied voltage.
As regard the in-depth analysis of the Rux response under X-rays, we observed a slow transient in the current dynamical curves both varying the bias voltage and the dose rate. We performed exponential fits of the rise and decays steps of the dynamical curves and, unlike the TIPSSC_07, we did not observe a trend of the slow and fast time constants (t_1 and t_2, respectively) with both the bias voltage and the dose rate. Subsequently, a measurement under LED (λ = 375 nm) illumination has been performed and the dynamical curve has shown, unlike those with the X-rays, a faster response with a response time below 200 ms. This feature is therefore in contrast with that observed for the TIPSSC_07, possibly indicating that in Rubrene crystals the two mechanisms of photogeneration have different nature.
In general, among these samples we observed a high variability in terms of both X-ray detection and dark current. The principal results related to the Rubrene-based samples reported in this chapter are summarized in Table 5.4.

Sample	Electrodes geometry	I_{off} @ 10V (pA)	Sensitivity @ 10 V (nC/Gy)	S/N max @10V	ΔI @ 10 V @ 117 mGy/S (pA)	Response
Rux_04	planar Au	1800	0.67 ± 0.32	0.02 @ 77.7 mGy/s	86	!
Rux_03		600	1.05 ± 0.09	0.15 @ 117 mGy/s	160	!
Rux_05		500	0.85 ± 0.24	0.35 @ 117 mGy/s	170	!
Rux		130	7.59 ± 0.56	2.70 @ 98.6 mGy/s	480	√
Rux_08		80	3.13 ± 0.18	4.36 @ 117 mGy/s	460	√

Table 5.4: Summarized results (Rubrene-based samples).

6 Characterization of other OSSCs-based detectors

In these chapter we report the characterization results of other seven OSSCs-based devices. Four devices are based on 1,2-dimethyl-1,1,2,2-tetraphenyldisilane (DMTPDS); one sample on 5,6,11,12-tetraphenyltetracene (Naphthalene) and two devices on Methylphenylnaphtaleneimide (NTHI). The principal features of the samples under test are reported in Table 6.1.

Molecule	Sample	Electrodes geometry
DMTPDS	DMTPDS_01	planar Au
	DMTPDS SC3 MS	vertical with Ag paste
	DMTPDS 4 MS	planar Ag
	DMTPDS Poly 4 MS	planar Ag
Naphthalene	Naphthalene	planar Au
NTHI	NTHI_01	planar Au
	NTHI_02	planar Au

Table 6.1: Features of samples under test.

6.1 DMTPDS

The molecular structure of the DMTPDS is reported in Figure 6.1. As can be seen, the molecule presents silicon atoms, which were introduced with the aim to increase the X-ray cross section. The introduction of high Z elements in order to increase the X-ray attenuation has been already treated in literature, for example by *A. Intaniwet et al.* [**26**]. Although the sample reported in this article was based on thin film polymer, the authors show that adding high-Z nanoparticles into the active layer of the device leads to an improvement of the device performance.

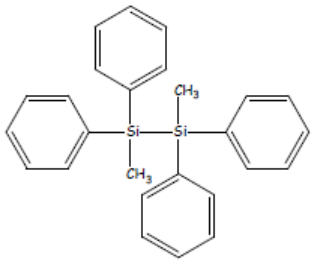

Figure 6.1: molecular structure of DMTPDS.

In the next subsections we will shows the characterization results of four DMTPDS-based detectors, which presents different features.

6.1.1 DMTPDS_01

The DMTPDS_01 crystal is shown in Figure 6.2, where we report two images taken with the optical microscope in reflection and in transmission, respectively. The DMTPDS_01 has gold electrodes in planar configuration.

a) 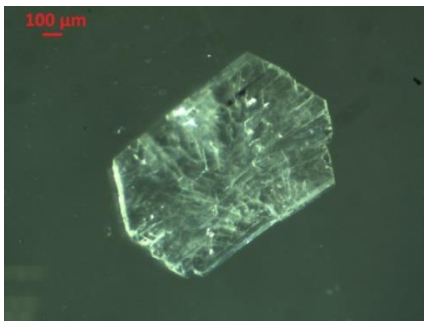

b) 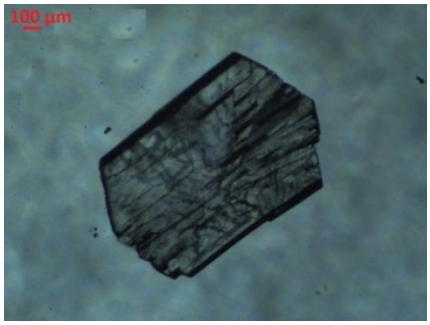

Figure 6.2: Images of the DMTPDS_01 crystal taken with the optical microscope a) in reflection and b) in transmission.

Figure 6.3a shows repeated IV off characteristics between 0 V and 50 V. As can be seen, the results show a bias stress effect that becomes greater as the bias voltage increases: at 50 V the graph shows a ΔI of about 140 pA between the first and the last curve acquired. The dynamical behavior of the

current, obtained with X-ray beam on/off cycles is reported in Figure 6.3b for different bias voltages. This results show a fast response and a drift of the dark current, more evident at 50 V.

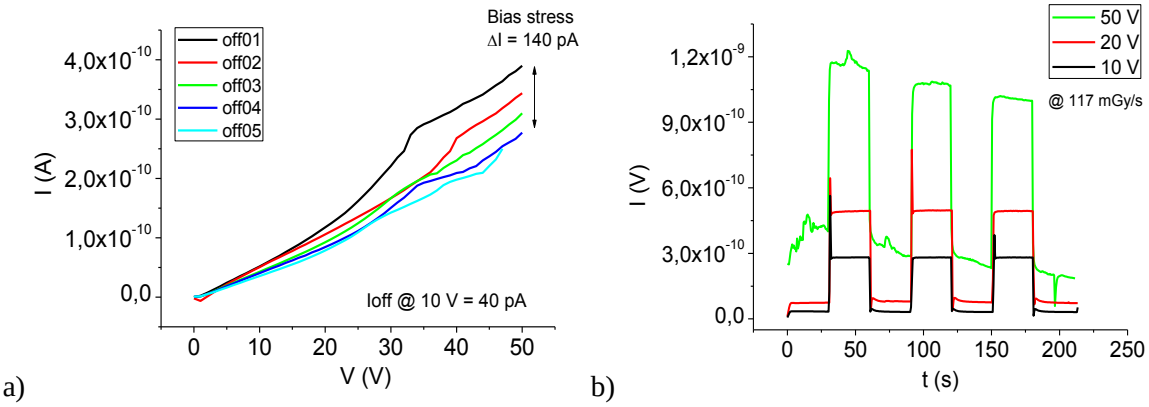

Figure 6.3: a) Repeated IV off curves between 0 V and 50 V and b) dynamical response at different bias voltages for the DMTPDS_01 sample.

The ΔI plotted as a function of the dose rate is shown in Figure 6.4a for different bias voltages. Regarding the sensitivity, the values are plotted versus the applied voltage in Figure 6.4b and reported numerically in Table 6.2.

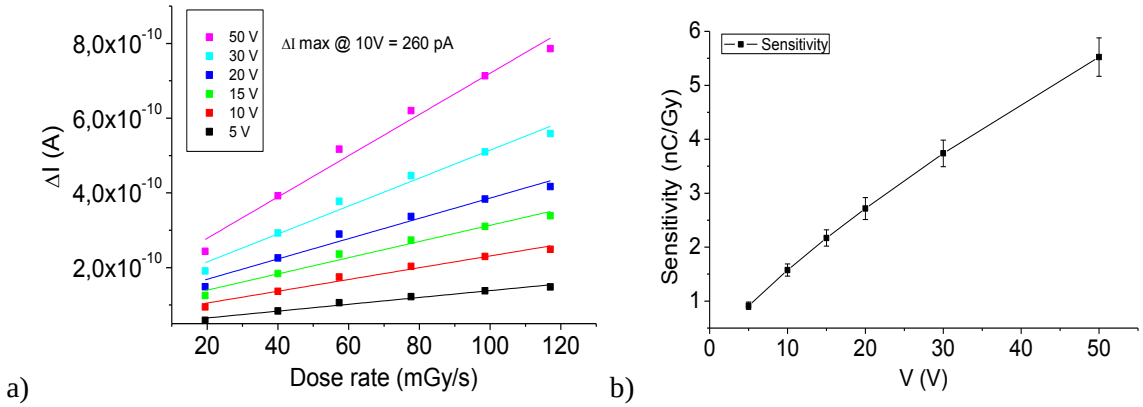

Figure 6.4: a) ΔI response for different bias voltages and b) sensitivity vs bias voltage (DMTPDS_01).

Bias voltage (V)	Sensitivity (nC/Gy)	Std error (nC/Gy)
5	0,91	0,07
10	**1,57**	**0,11**
15	2,17	0,15
20	2,72	0,20
30	3,74	0,25
50	5,52	0,36

Table 6.2: Sensitivity values (DMTPDS_01).

This sample is characterized by ΔI values and sensitivities slightly higher than those of the reference. Although the signal-to-noise ratios (Figure 6.5) are high (S/N = 13.5 at the maximum dose rate and 10V of applied voltage), considering the previous figures of merit we do not define the sample response as meaningful.

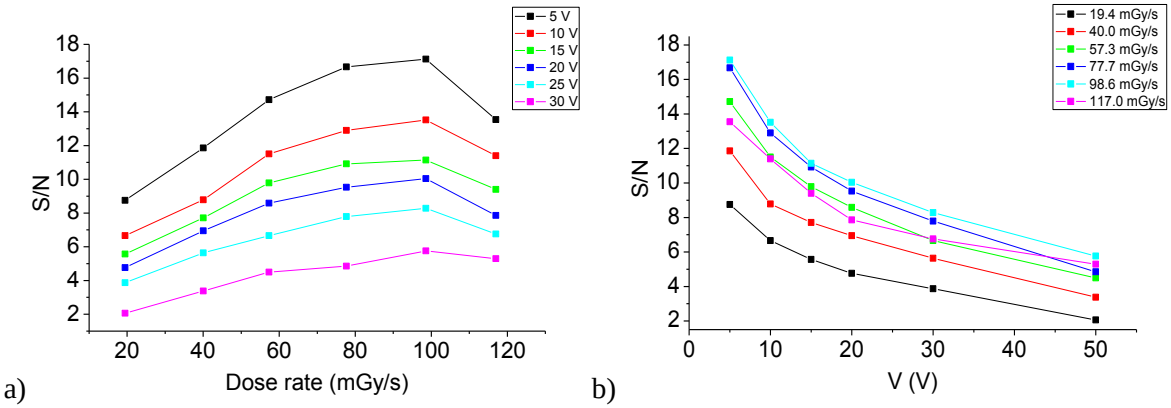

a) b)

Figure 6.5: Signal-to-noise ratio plotted as a function of the a) dose rate and b) bias voltage (DMTPDS_01).

6.1.2 DMTPDS SC3 MS - DMTPDS 4 MS - DMTPDS poly 4 MS

Figure 6.6 shows the images, taken with the optical microscope, of the other three DMTPDS-based samples.

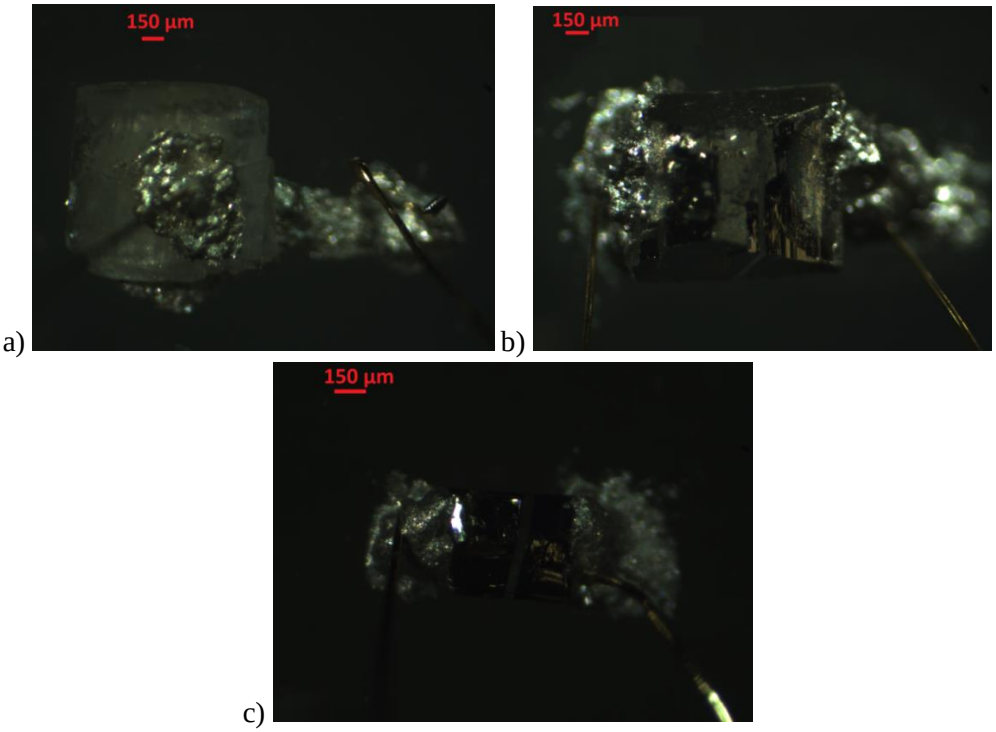

a) b) c)

Figure 6.6: image of the a) DMTPDS SC3 MS (vertical geometry with Ag paste); b) DMTPDS SC3 MS (planar Ag electrodes); c) DMTPDS 4 MS (planar Ag electrodes).

In order to test a different crystallographic direction, the DMTPDS SC3 MS (Figure 6.6a), was not prepared as described in subsection 3.1: in this case a vertical configuration (subsection 2.5) has been realized using Ag paste both on the top and on the bottom of the crystal. On the other hand, both the DMTPDS SC3 MS (Figure 6.6b) and the DMTPDS 4 MS (Figure 6.6c) have silver electrodes in planar geometry. Results showed that all these samples have in common a very low dark current (Table 6.3), comparable with that of the reference. In this case we can assert the absence of charge carrier injection through the metal-semiconductor barrier. Therefore, for all these samples the characterization was not further carried out.

Sample	Electrodes geometry	I_{off} @ 10 V (pA)	Response
DMTPDS SC3 MS	vertical with Ag paste	1,5	X
DMTPDS 4 MS	planar Ag	1,3	X
DMTPDS Poly 4 MS	planar Ag	1,8	X

Table 6.3: summarized information regarding the other three DMTPDS-based samples.

6.2 Naphthalene

The naphthalene is an apolar and low mobility crystal, which molecular structure is reported in Figure 6.7. This sample is characterized by a planar geometry with gold electrodes.

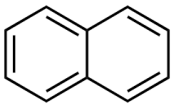

Figure 6.7: molecular structure of the naphthalene.

Figure 6.8a reports repeated IV off characteristics, showing the absence of a significant bias stress effect. The dynamical behavior of the current is reported in Figure 6.8b for different bias voltages.

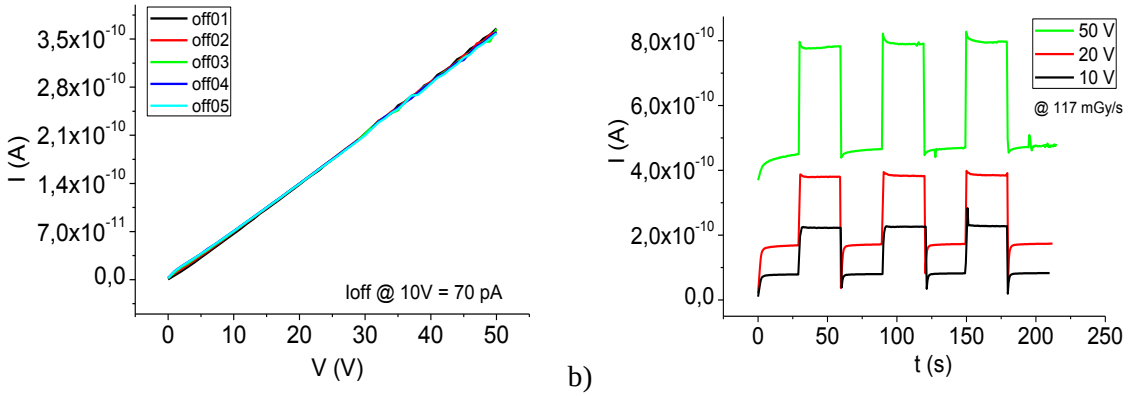

Figure 6.8: a) repeated IV off curves between 0 V and 50 V and b) dynamical response at different bias voltages for the Naphthalene sample.

Figure 6.9a and Figure 6.9b show the ΔI response of the sample and the graph reporting the sensitivity values plotted as a function of the bias voltage, respectively. Considering the applied voltage of 10 V, this sample is characterized by a maximum ΔI of 140 pA and by a sensitivity of (1.24 ± 0.06) nC/Gy. These results do not allow to define the detector response as meaningful. In addition, this crystal presents problems due to its tendency to sublimate at room temperature.

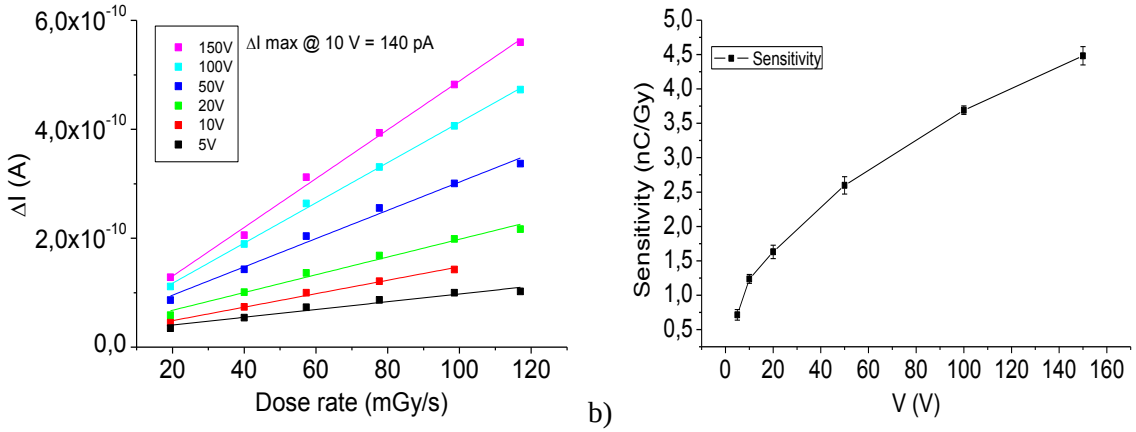

Figure 6.9: a) ΔI response for different bias voltages and b) sensitivity vs bias voltage (Naphthalene).

Bias voltage (V)	Sensitivity (nC/Gy)	Std error (nC/Gy)
5	0,71	0,08
10	**1,24**	**0,06**
20	1,63	0,10
50	2,60	0,13
100	3,69	0,06
150	4,48	0,13

Table 6.4: Sensitivity values (Naphthalene).

6.3 NTHI_01 – NTHI_02

In this subsection we report the characterization results of two samples based on Methylphenylnaphtaleneimide (NTHI), which have gold electrodes in planar geometry. The NTHI molecular structure is reported in Figure 6.10.

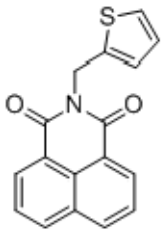

Figure 6.10: molecular structure of the NTHI.

The principal characterization results are summarized in Table 6.5 for both samples. The figures of merit related to the NTHI_01 samples indicates a poor response, in fact at 10 V of applied voltage it shows a ΔI of 170 pA and a sensitivity of (1.18 ± 0.07) nC/Gy. In addition, due to the dark current of 260 pA at 10 V, a signal-to-noise ratio smaller than one has been obtained.
Concerning the NTHI_01, we can observe a high dark current: although the ΔI and the sensitivity are greater than those of the reference, the noisy response does not allow to define the detector's response as significant.

Molecule	Sample	Electrodes geometry	I_{off} @ 10V (pA)	Sensitivity @ 10 V (nC/Gy)	S/N max @10V	ΔI @ 10 V @ 117 mGy/s (pA)	Response
NTHI	NTHI_01	planar Au	260	1.18 ± 0.07	0.81 @ 117 mGy/s	170	!
	NTHI_02		5700	2.78 ± 0.58	0.07 @ 98.6 mGy/s	390	!

Table 6.5: principal characterization results (NTHI-based samples)

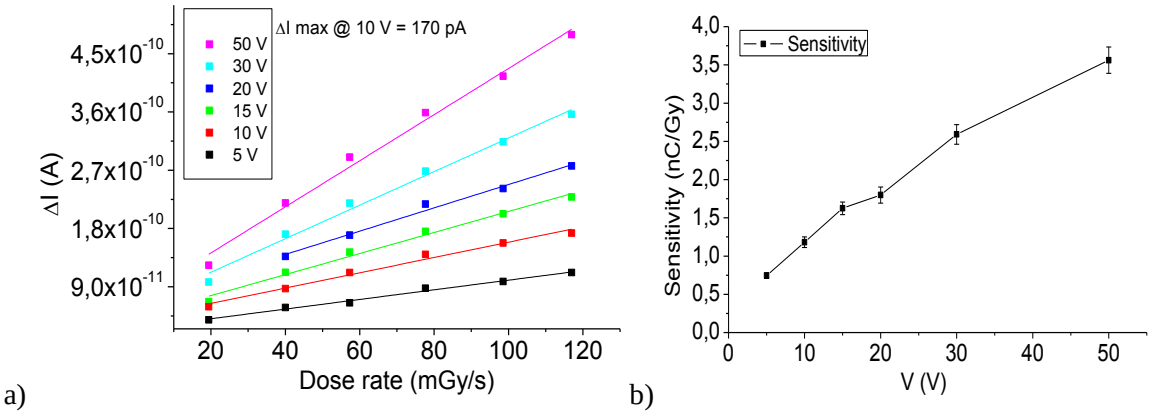

Figure 6.11: a) ΔI response for different bias voltages and b) sensitivity vs bias voltage (NTHI_01).

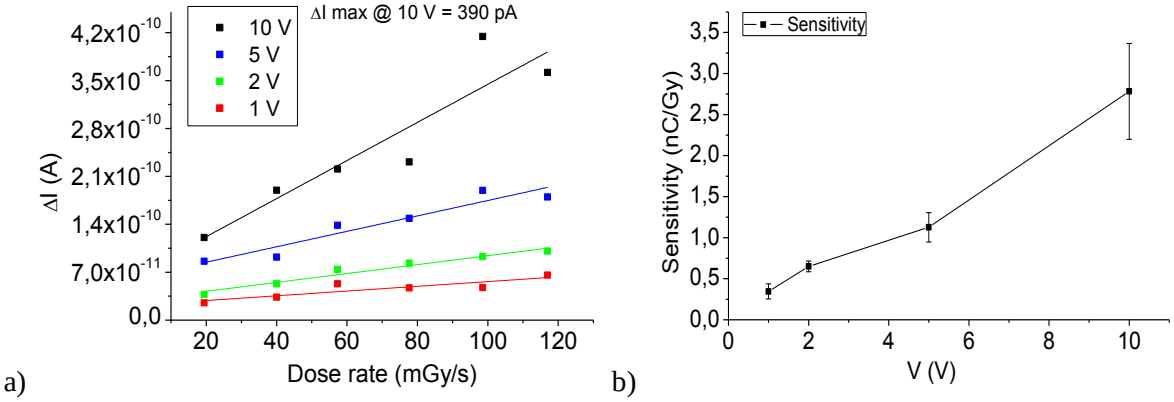

Figure 6.12: a) ΔI response for different bias voltages and b) sensitivity vs bias voltage (NTHI_02).

6.4 Summary

The samples reported in the current chapter did not show a significant response under X-rays. The DMTPDS_01 showed a maximum ΔI at 10 V of 260 pA and a sensitivity of (1,57 ± 0,11) nC/Gy, values comparable with those of the reference device. The other three DMTPDS-based samples (DMTPDS SC3 MS, DMTPDS 4 MS, DMTPDS poly 4 MS) have shown a dark current at 10 V comparable with that of the reference device and therefore the characterization was not further carried out. In this case we hypothesized the absence of charge carrier injection through the metal-semiconductor barrier.

Naphthalene and NTHI_01 samples did not show a meaningful response, too. Moreover, the Naphthalene is a very unstable molecule due to its tendency to sublimate at room temperature. Although the NTHI_02 showed a ΔI and a sensitivity greater than those of the reference, its high dark current generates a noisy response and therefore low signal to noise ratios.

In order to have an overview on the principal results obtained in this chapter, we report a summary in Table 6.6.

Molecule	Sample	Electrodes geometry	I_{off} @ 10V (pA)	Sensitivity @ 10 V (nC/Gy)	S/N max @10V	ΔI @ 10 V @ 117 mGy/s (pA)	Resp.
DMTPDS	DMTPDS_01	planar Au	35	1.57 ± 0.11	13.5 @ 98.6 mGy/s	260	!
	DMTPDS SC3MS	Vertical Ag paste	1.5	/	/	/	X
	DMTPDS 4MS	planar Ag	1.3	/	/	/	X
	DMTPDS Poly4MS	planar Ag	1.8	/	/	/	X
Naphthalene	Naphthalene	planar Au	70	1.24 ± 0.06	1.52 @ 98.6 mGy/s	145	!
NTHI	NTHI_01	planar Au	260	1.18 ± 0.07	0.81 @ 117 mGy/s	170	!
	NTHI_02	planar Au	5700	2.78 ± 0.58	0.07 @ 98.6 mGy/s	390	!

Table 6.6: summarized results (other OSSCs-based samples).

7 Final Discussion

In this experimental work, sixteen OSSCs-based samples have been prepared and characterized as direct X-ray detectors. Crystals composed of the following organic molecules identify our samples:

- 6,13-bis(triisopropylsilylethynyl)pentacene (TIPS-Pentacene);
- 5,6,11,12-tetraphenyltetracene (Rubrene);
- 1,2-dimethyl-1,1,2,2-tetraphenyldisilane (DMTPDS);
- 5,6,11,12-tetraphenyltetracene (Naphthalene);
- Methylphenylnaphtaleneimide (NTHI)

Samples' main features and final responses are summarized in Table 7.1.

Molecule	Sample	Electrodes geometry	Response
TIPS-Pentacene	TIPSSC_01 (DCB 1%)	Planar Au	!
	TIPSSC_02 (DCB 1%)	Planar Au	!
	TIPSSC_07 (Tetralin 5.75 mg/mL)	Planar Ag	√
	TIPSSC_09 (Tetralin 4.9 mg/mL)	Planar Au	√
Rubrene	Rux_03	Planar Au	!
	Rux_04		!
	Rux_05		!
	Rux_08		√
	Rux		√
DMTPDS	DMTPDS_01	Planar Au	!
	DMTPDS SC3MS	Vertical Ag paste	X
	DMTPDS 4MS	Planar Ag	X
	DMTPDS Poly4MS	Planar Ag	X
Naphthalene	Naphthalene	Planar Au	!
NTHI	NTHI_01	Planar Au	!
	NTHI_02		!

Table 7.1: Samples' main features and final responses. Legend: !) non-significant response under X-rays; √) significant response under X-rays; x) no response.

As regards the TIPSSC-based samples, four devices with different features have been tested (TIPSSC_01, TIPSSC_02, TIPSSC_07, TIPSSC_09) and the results have been illustrated in chapter 4. The first two samples (TIPSSC_01 and TIPSC_02), which have been grown with DCB solvent (1% concentration) and have gold electrodes in planar geometry, did not show a significant response under X-rays. With respect to the previous samples, the TIPSSC_07 has been grown with Tetralin solvent (5.75 mg/mL concentration) and has silver electrodes. The TIPSSC_07 provided a significant response under X-rays, with sensitivities up to (3.63 ± 0.15) nC/Gy at the bias voltage of 10 V. The last sample, the TIPSSC_09, has been grown with Tetralin solvent (4.9 mg/mL concentration) and has gold electrodes: it showed a significant response too, achieving sensitivities up to (2.99 ± 0.13) nC/Gy at 10 V of applied voltage. Considering these results, we correlated the differences in the X-ray detection performances to the solvent employed. Moreover, this hypothesis is supported by the characterization results (not reported in this thesis) of another sample, the TIPSSC_04. The latter has been grown employing mainly DCB and has gold electrodes: as the other samples grown with DCB, it did not show a meaningful response under X-rays.
The response behavior of the TIPSSC_07 under X-rays showed a slow transient in the current dynamical curves both varying the bias voltage and the dose rate. This behavior has been already observed in organic-based devices exposed to X-rays and, in particularly, in the following cases:

- in detectors based on organic thin film semiconductors (PTAA-based diodes) [**16**];
- in organic insulating materials (polystyrene) [**21**] [**22**].

In the first case, the authors correlated this phenomenon to the height of the metal-barrier: a slow transient response was observed only when the electrodes' work function was higher than the HOMO level of the polymer. In the second case, the author correlated this behavior to the presence of traps, which capture conduction electrons and subsequently release them into conduction levels.
In order to evaluate the presence of a trend in relation to the dose rate and the bias voltage, we performed exponential fits of the rise and decay steps of the dynamical curves of the TIPSSC_07 and we analyzed the variation of the slow and fast time constant (t_1 and t_2, respectively) with both the bias voltage and the dose rate. The results showed that both the time constants related to the rise and decay steps of the curves tend in general to decrease as the bias voltage increases. Furthermore, the time constants related to the rise step of the curves tend to decrease as the dose rate increases, while those related to the decay step do not vary with the dose rate.
With the aim to reach a deeper interpretation of the photoconversion process occurring in X-ray detectors, a measurement with the TIPSSC_07 under LED (λ = 375 nm) illumination has been performed and the dynamical curve showed, as those under X-rays, a slow charge and discharge response. We compared this measurement with that obtained under X-rays at 98.6 mGy/s and we observed that the time constants of both the responses were comparable, possibly indicating that the two mechanisms of photogeneration and charge collection have the same nature (Figure 7.1).

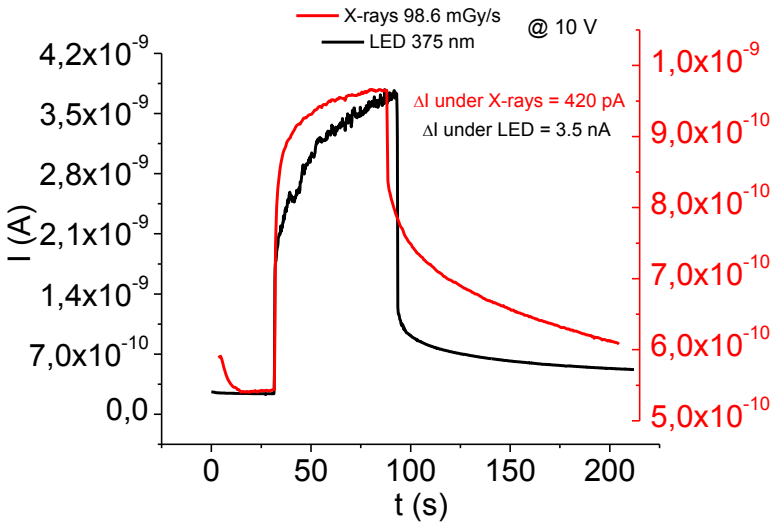

Figure 7.1: Current dynamical response under LED (λ = 375 nm) illumination (black line) and under X-rays at the dose rate of 98.6 mGy/s (red line) (TIPSC_07).

The slow transient response observed in the TIPSSC_07 under visible photons has been already discussed in literature, too. In particular, it has been observed in the following cases:

- in TIPS-Pentacene single crystals under LED (λ = 660 nm) illumination [**18**] [**27**];
- in modulated photocurrent measurement of organic photocells based on Titanyl phthalocyanine (TiOPc), under LASER irradiation (λ = 633 nm) [**23**].

In the first case the authors state that the origin of persistent photoconductivity involves the presence of traps, which may either pre-exist, or which may be created or modified by the optical illumination. In the second case the authors describe the phenomenon in terms of modified space-charge distribution at the Schottky barrier, due to an excess of photocarriers injection. In addition, they state that the origin of the relaxation mechanism should be a key to determine the activation energy of localized states in the organic semiconductors.

Considering the Rubrene-based devices, five samples presenting gold electrodes in planar geometry have been tested (Rux_03, Rux_04, Rux_05, Rux_08, Rux) and the results have been illustrated in chapter 5. All these crystals have been grown by Physical Vapor Transport (PVT, subsection 1.5). The first three samples (Rux_03, Rux_04, Rux_05) had in common an high dark current and they did not provide a significant response under X-rays. The Rux_08 sample, instead, showed a lower dark current and a detectable response in terms of ΔI, sensitivity and signal-to-noise ratio. In particular, even if the Rux sample showed the highest sensitivity (7.59 ± 0.56 nC/Gy at 10 V of applied voltage) among all the OSSCs-based samples characterized through the entire activity, Rubrene-based samples showed in general low detection performances. So far, problems related to low stability, photo-oxidation phenomena [**28**] and low reproducibility do not allow to consider Rubrene as ideal candidate for X-ray detection. In comparison, other OSSCs-based devices characterized as direct X-ray detectors reported in literature (based on 4-hydroxycyanobenzene (4HCB) and 1,5-dinitronaphthalene (DNN)) showed sensitivities comparable with that obtained

with the Rux sample: however, DNN- and 4HCB-based devices also showed good stability, high reproducibility and a fast response under X-rays. [**6**] [**11**]

The response behavior of the of the Rux under X-rays showed, as that of the TIPSSC_07, a slow transient in the current dynamical curves both varying the bias voltage and the dose rate. We performed exponential fits of the rise and decays steps of the dynamical curves and, unlike the TIPSSC_07, we did not observe a trend of the slow and fast time constants (t_1 and t_2, respectively) with both the bias voltage and the dose rate.

As performed for the TIPSSC_07, a measurement with the Rux under LED (λ = 375 nm) illumination has been carried out and the dynamical curve showed, unlike those under X-rays, a faster response with a response time below 200 ms (Figure 7.2). This feature is therefore in contrast with that observed for the TIPSSC_07, possibly indicating that in Rubrene crystals the two mechanisms of photogeneration have different nature and the relaxation process could involve traps of different activation energy [**23**].

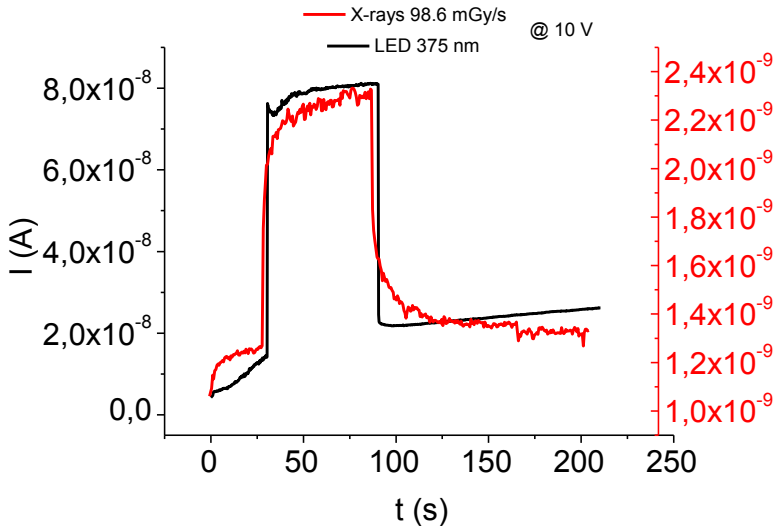

Figure 7.2: Current dynamical response under LED (λ = 375 nm) illumination (black line) and under X-rays at the dose rate of 98.6 mGy/s (red line) (Rux).

Concerning the Rux response under visible photons illumination, a similar study has been carried out on field effect transistors based on Rubrene single crystals, under LASER irradiation (λ = 405 nm). [**17**] The authors observed a small persistent photoconductivity under continuous illumination, effect explained by delayed recombination aided by spatial separation of the photocarriers. Photocurrent transients measured by applying short pulses on the other hand showed a complete recovery in the microsecond regime implying immediate recombination.

As regards the other samples, four DMTPDS-, one Naphthalene- and two NTHI-based devices have been characterized and the results have been illustrated in chapter 6. All these samples reported did not show a significant response under X-rays. The DMTPDS_01 sample showed, at 10 V of applied voltage, a maximum ΔI of 260 pA and a sensitivity of (1.57 ± 0.11) nC/Gy. Due to its low dark current, we obtained high signal-to noise ratio. However, since the ΔI and the sensitivity

were slightly higher than those of the reference, we did not consider as meaningful the device's response.

The other three DMTPDS-based sample (DMTPDS SC3 MS, DMTPDS 4 MS, DMTPDS poly 4 MS) have shown a dark current at 10 V comparable with that of the reference device and therefore the characterization was not further carried out. In this case we can assert the absence of charge carrier injection through the metal-semiconductor barrier.

Also Naphthalene and NTHI_01 samples did not give a significant response. Moreover, Naphthalene is a very unstable molecule due to its tendency to sublimate at room temperature. Although the NTHI_02 showed a ΔI and a sensitivity greater than those of the reference, its high dark current generated a noisy response and therefore low signal to noise ratios.

In general, the characterization results related to the latter samples do not allow to consider, at this stage, these molecules as promising candidates for X-ray detection.

8 Conclusions

Conclusions can be summarized in the following points:

- The reference values of the principal detector's figures of merit (dark current, sensitivity and ΔI) have been verified.

- In samples based on TIPS-Pentacene the solvent employed in the crystals growth played an important role in the devices X-ray detection performances. Independently on the electrodes material, samples based on crystals grown using Tetralin showed a significant response under X-rays, although lower than that of other OSSCs-based X-ray detectors reported in literature. Sensitivities up to (3.63 ± 0.15) nC/Gy have been calculated at 10V of applied voltage. Samples based on crystals grown employing dichlorobenzene did not show a meaningful response under X-rays.

- Rubrene-based samples showed an high variability in terms of both dark current and X-ray detection: only samples with a low dark current (few tens of pA) showed a significant response under X-rays, even if their performances were lower than other OSSCs-based X-ray detectors reported in literature. Sensitivities up to (7.59 ± 0.56) nC/Gy at 10 V of applied voltage have been obtained, although problems due to low stability and reproducibility have been evidenced. Samples with higher dark current (few hundreds of pA) showed a poor response under X-rays.

- Unlike the inorganic counterpart, high mobility organic crystals as TIPS-Pentacene and Rubrene showed a slow transient response under X-rays.

- TIPS-Pentacene showed a slow transient response both under X-rays and LED radiation, possibly indicating that the two mechanisms of photogeneration have the same nature. On the other hand, Rubrene showed a slow transient response under X-rays and a fast response under LED illumination. Therefore we hypothesize that in Rubrene crystals the two photogeneration mechanisms have different nature.

- Characterization results related to the DMTPDS-, Naphthalene- and NTHI-based samples do not allow to consider, at this stage, these molecules as promising candidates for X-ray detection.

In conclusion, we point out the importance of this research field in order to develop novel, smart alternative to traditional inorganic semiconducting solid-state radiation detectors and to reach a deeper understanding of the intrinsic mechanisms at the basis of their operating principle.

Appendix A – List of figures

Appendix B – List of tables

Acknowledgments

I would like to express gratitude to Prof.ssa Beatrice Fraboni for giving me the opportunity to carry out this thesis work at the organic semiconductors laboratory.
I am also pleased to thank very much Dott.ssa Laura Basiricò for her patience in following me during the activity.

A special thanks to all my dears.

Enrico Zanazzi

Bibliography

[1] W. Brütting, *Physics of organic semiconductors*.: Wiley-VHC, 2005.

[2] G. Mattana, *Realisation and Characterisation of Organic Electronic Devices for E-texiles applications*., Università di Cagliari, PhD thesis, 2006.

[3] P. Cosseddu, *Correlation between interface-dependent properties and electrical performances in OFETs*., Università di Cagliari, PhD thesis, 2006.

[4] Petrucci, Harwood, and Herring, *Chimica Generale, Principi e moderne applicazioni*.: Piccin, 2002.

[5] V. Podzorov, *Organic single crystals: addressing the fundamentals of organic electronics*.: MRS BULLETTIN, Volume 38, January 2013.

[6] Beatrice Fraboni, Andrea Ciavatti, Laura Basiricò, Alessandro Fraleoni-Morgera, *Organic semiconducting single crystals as solid-state sensors for ionizing radiation*.: The Royal Society of Chemistry 2014.

[7] R. Noriega, A. Saleo, *Charge transport theories in organic semiconductors*.

[8] Hui Jiang, Christian Kloch, *Single-crystal growth of organic semiconductors*.: MRS BULLETTIN, VOLUME 38, 2013.

[9] Hanying Li, Gaurav Giri, Jeffrey B.-H.Tok, Zhenana Bao, *Toward high-mobility organic field-effect transistors: control of molecular packing and large-area fabrication of single-crystal-based devices*.: MRS BULLETTIN, VOLUME 38, 2013.

[10] Ignacio Gutièrrez Lezama, Alberto F. Morpurgo, *Progress in organic single-crystal field-effect transistor*.: MRS BULLETTIN, VOLUME 38, 2013.

[11] B. Fraboni, A. Ciavatti, F. Merlo, L. Pasquini, A. Cavallini, A. Quaranta, A. Bonfiglio, A. Fraleoni-Morgera, *Organic remiconductors single crystals as next generation of low-cost, room-temeprature electrical x-ray detectors*.: Advanced Materials, 2012.

[12] Glenn F. Knoll, *Radiation detection and measurement* , Third edition ed.: John Wiley & Sons.

[13] William R. Leo, *Techniques for nuclear and particle physics experiments*.

[14] Akarin Intaniwet, Joseph L. Keddie, Maxim Shkunov, Paul J. Sellin, *High charge-carrier mobilities in blends of poly(triarylamine) and TIPS-pentacene leading to better performing X-*

ray sensors.: Organic Electronic 12 1903-1908, 2011.

[15] Akarin Intaniwet, Chistopher A. Mills, Maxim Shkunov, Heiko Thiem, Joseph L. Keddie, Paul J. Sellin, *Characterization of thick film poly(triarylamine) semiconductors diodes for direct x-ray detection*.: Journal of applied Physics 106, 064513, 2009.

[16] Akarin Intaniwet, Christopher A. Mills, Paul J. Sellin, Maxim Shkunov, Joseph L. Keddie, *Achieving a Stable Time Response in Polymeric Radiation Sensors under Charge Injection by X-rays*.: Applied materials & Interfaces Vol. 2 No. 6 1692-1699, 2010.

[17] N. Mathews, D. Fichou, E. Menard, V. Podzorov, S.G. Mhaisalkar, *Steady-state and transient photocurrents in rubrene single crystal free-space dielectic transistors*.: Applied Physics letters 91, 212108 (2007).

[18] T. Tokumoto, J.S. Brooks, D. Graf, E.S. Choi, N. Biskup, D.L. Eaton, J.E. Anthony, S.A. Odom, *Persistent photo-exited conduting states in functionalized pentacene*.: Synthetic Metals 152 (2005) 449-452.

[19] Kang-Jun Baeg, Maddalena Binda, Dario Natali, Mario Caironi, Yong-Young Noh, *Organic light detectors: photodiodes and phototransistors*.: Advanced Materials, 2013, 25, 4267 - 4295.

[20] Kevin Kyungbum Ryu, David Da He, Vladimir Bulovic, Charles G. Sodini, *Bias-Stress Effect in Pentacene Organic Thin-Film Transistors*.: IEEE TRANSACTIONS ON ELECTRON DEVICES, VOL. 57, NO. 5, MAY 2010.

[21] J.F. Fowler, *Radiation-induced conductivity in solide state, and some application*.: IOP Science.

[22] J.F. Fowler, *X-ray induced conductivity in insulating materials*.: IOP Science.

[23] K. Saito, S. Kobayashi, *Bias-Light-Induced Transient Responses of the Modulated Photocurrent in Organic Photovoltaic Cells*.: Jpn. J.Appl. Phys. 2003, 42, L781.

[24] Tatsuo Hasegawa, Jun Takeya, *Organic field-effect transistors using single crystals*.: Sci. Technol. Adv. Mater., 2009.

[25] Hikmet Najafov, Daniel Mastrogiovanni, Eric Garfunkel, Leonard C. Feldman, Vitaly Podzorov, *Photon-Assisted Oxygen Diffusion and Oxygen-Related Traps in Organic Semiconductors*.: Adv. Mater. 2011, 23, 981–985.

[26] A. Intaniwet, C.A. Mills, M. Shkunov, P.J. Sellin, J.L. Keddie, *Heavy metallic oxide nanoparticles for enhanced sensitivity in semiconducting polymer x-ray detectors*.: Nanotechnology 23 (2012).

[27] J. S. Brooks, T. Tukumoto, E.-S. Choi, N. Biskup, L. Eaton, J. E. Anthony, S. A. Odom, *Persistent photoexited conducting states in functionalized pentacene*.: Journal of Applied Physics, Vol. 96, Number 6, 2004.

[28] Hikmet Najafov, Daniel Mastrogiovanni, Eric Garfunkel, Leonard C. Feldman, Vitaly Podzorov, *Photon-Assisted Oxygen Diffusion and Oxygen-related Traps in Organic Semiconductors*.: Adv. Mat. 2011, 23, 981-985.